NACA

RESEARCH MEMORANDUM

AN ANALYSIS OF PRESSURE STUDIES AND EXPERIMENTAL AND

THEORETICAL DOWNWASH AND SIDEWASH BEHIND

FIVE POINTED-TIP WINGS AT

SUPERSONIC SPEEDS

By William B. Boatright

Langley Aeronautical Laboratory
Langley Field, Va.

NATIONAL ADVISORY COMMITTEE
FOR AERONAUTICS
WASHINGTON
April 21, 1954

CONTENTS

NATIONAL ADVISORY COMMITTEE FOR AERONAUTICS

RESEARCH MEMORANDUM

AN ANALYSIS OF PRESSURE STUDIES AND EXPERIMENTAL AND

THEORETICAL DOWNWASH AND SIDEWASH BEHIND

FIVE POINTED-TIP WINGS AT

SUPERSONIC SPEEDS

By William B. Boatright

SUMMARY

Flow-angle and pressure surveys behind five, thin, pointed-tip wings of varying plan form have been made at Mach numbers 1.62 and 2.41. Also, preliminary schlieren studies at a Mach number 1.93 for the same five planform wings were made to illustrate the behavior of the vortex sheet. The surveys were conducted at 1.5, 3, and 4 root chords behind three triangular wings of 50°, 63°, and 72° leading-edge sweep angle, and behind the 50° triangular wing reversed. The flow behind a pointed-tip wing having a sweptback leading edge and a sweptforward trailing edge (both 50°) was also surveyed.

In the analysis of the data, especial attention was focused on the assessments of the validity of the various theoretical methods for predicting the flow at wing angles of attack sufficiently high for the behavior of the vortex sheet to become important.

For the low-aspect-ratio triangular wings (where the Mach number component normal to the leading edge is subsonic), the vortex sheet rolls up rapidly into a single concentrated region of vorticity and the theoretical model of the flow was assumed as a single bent line vortex for comparing the theoretical prediction with experiment at moderately high angles of attack (9° to 17°). An adjustment to the method for determining the vertical location at stations behind the wing is proposed in the report.

For the high-aspect-ratio triangular wings (where the Mach number component normal to the leading edge is supersonic), the more complex nature of the vortex sheet is illustrated, and for the triangular wing with 50° leading-edge sweep angle, various theoretical methods for predicting the flow field are compared with experiment.

Experiment and one of the theoretical methods are compared for the reversed triangular wing and the pointed-tip wing with the 50° sweptback leading edge and sweptforward trailing edge.

INTRODUCTION

A knowledge of the flow fields behind wings at supersonic speeds is important in assessing the stability characteristics of aircraft and missiles. A general picture of the complex nature of the problem and the relative significance of wing lift coefficient, aspect ratio, and distance behind the wing, on the nonlinearities involved in estimating the flow field characteristics, is treated theoretically in reference 1. Point measurements of the flow angle are reported in references 2 to 11 for wings of rectangular, triangular, trapezoidal, and sweptback plan forms at various supersonic Mach numbers, and studies of the flow fields behind wing-body combinations for both aircraft and missile configurations are reported in references 12 to 19. It can be seen that these references include some downwash measurements at transonic and low supersonic speeds; and, as in reference 17, comprehensive studies of wing-body combinations have recently been made at supersonic speeds. Various theoretical estimates are being used to approximate the flow behind different wings, but as yet sufficient systematic tests are not available to assess completely their validity at various locations behind the wing or throughout the variations in plan form and lift coefficient that might exist. Data are being accumulated, however, particularly in the high-aspect-ratio case.

Although the scope of the present investigation includes only wing-alone tests, the flow field for this case becomes very complex at moderate and high angles of attack for different variations in plan form; and theoretical predictions of the flow field have met with little success, particularly for downstream locations inboard of the wing tips.

Most of the theoretical work on predicting the flow fields behind wings has been developed using linear theory and assuming that the wing and vortex sheet behind the wing remain in one horizontal plane throughout the angle-of-attack range. (When using such an assumption, agreement between theory and experiment can only be expected at low angles of attack.) Examples of theoretical methods of this type include the conical-flow technique of references 20 to 22, vortex and lifting-line methods of references 23 and 24, doublet method of reference 25, and a line-source method in reference 26. (This latter method uses a line source to build up solutions that are applied to a particular plan form in the same fashion as are those of the conical-flow technique.) When applying any of these methods to configurations at higher angle of attack, some success has been obtained by correcting for the deflection of the vortex sheet at successive span stations to determine the actual location of a particular field point with respect to this vortex sheet (refs. 2 and 4). However, for those cases where the rolling up of the vortex sheet becomes more important (higher angles of attack, lower aspect ratio, or larger distances behind the wing), other theoretical treatments would appear to be better for predicting the downwash or sidewash. Such theoretical methods

either assume the vortex sheet is completely rolled up and represent it
by a single line vortex, or else they represent the vortex sheet with a
number of two-dimensional line vortices which are allowed to float and
deform as is done in reference 27.

It is the purpose of the present investigation to supplement avail-
able experimental data on flow fields behind wings, as well as to furnish
more quantitative information on the choice of the theoretical method for
a given configuration and the accuracy to be expected when using such a
method.

The experimental phase of the investigation consisted of downwash,
sidewash, and pitot pressure measurements in planes normal to the free-
stream direction at stations 1.5, 3, and 4 root chords behind the wing
trailing edge. Three, thin, triangular-plan-form wings, whose leading
edges were swept back 50°, 63°, and 72°, were surveyed at free-stream
Mach numbers 1.62 and 2.41. In addition surveys were conducted at a Mach
number of 1.62 for the same stations behind the 50° sweptback triangular
wing reversed (i.e., apex downstream), and a straight, 0-taper-ratio
(diamond plan form) wing with 50° swept leading and trailing edges.

<div align="center">SYMBOLS</div>

$a = \tan \Lambda$ (appendix A)

A   aspect ratio

b   variable denoting ratio of tangent of conical ray from apex
          of triangular wing to tangent of Mach angle (appendix A)

b' wing semispan

C_L lift coefficient

c_{l_m} wing section lift coefficient at plane of symmetry

c_r wing root chord

$E(t')$ complete elliptic integral of second kind of modulus t',
       where $t' = \sqrt{1 - \beta^2 \cot^2 \Lambda}$

H_3 measured pitot pressure

H_{o_3} tunnel stagnation pressure

k   distance from origin to apex of two intersecting line
            vortices (appendix C)

m   slope of line vortex (appendix C)

M   free-stream Mach number

P_w pressure on wedge surface

r   radius of conical ray in polar coordinate system (appendix A),
            $$\frac{\beta \sqrt{y^2 + z^2}}{x}$$

R   Reynolds number (based on c_r)

V   free-stream velocity

u   perturbation velocity in x-direction

u'   perturbation velocity in x-direction on triangular wing at
            plane of symmetry (appendix A)

u_o perturbation velocity in x-direction on supersonic leading-
            edge triangular wing for region between leading edge and
            Mach line from apex (appendix A)

v   perturbation velocity in y-direction

w   perturbation velocity in z-direction

x   horizontal coordinate parallel to free-stream direction

x_o chord at plane of symmetry of triangular wing (appendix C)

y   horizontal coordinate, normal to free-stream direction

y_o one-half of distance apart of streamwise legs of bent-line
            vortex model of flow (appendix C)

z   vertical coordinate, normal to free-stream direction

α angle of attack, deg

β $\sqrt{M^2 - 1}$

Γ_m wing circulation at plane of symmetry

ϵ downwash angle, deg

$\theta = \tan^{-1}\frac{z}{y}$ (appendix A)

ϕ angle in vertical plane between line vortex and free-stream
          direction, deg

Λ sweepback angle of wing leading edge, deg

σ sidewash angle, deg

Subscripts:

B   body

W   wing

T   tail

TE   trailing edge

APPARATUS

Wind Tunnel

All tests were made in the Langley 9-inch supersonic tunnel, which
is a continuously operating, closed-circuit type of wind tunnel in which
the temperature, pressure, and humidity can be controlled. The test Mach
number is varied by interchangeable nozzles which form a test section
about 9 inches square.

Models and Model-Support Apparatus

The five semispan wings tested are shown in figure 1(a). The wings
were solid steel flat plates with beveled leading and trailing edges.
All wings had the same root chord, and the maximum thickness of the root
chord was $2\frac{1}{2}$ percent.

The wings were mounted from a boundary-layer bypass plate such that
the wing angle of attack could be changed with the bypass plate remaining
stationary. With the model-support design illustrated in figure 1(b),
there was no appreciable leakage of air through the bypass plate at the
wing-plate juncture or from the bottom wing surface to the top. The plan
form of the plate was conservatively designed such that a disturbance

from behind the plate could not bleed around the leading edge and influence the flow field in the region of the surveys. The photograph of figure 2(a), viewed obliquely downstream, illustrates the bypass plate and wing model, as well as the survey apparatus, mounted in a mockup using dummy sidewalls to represent the tunnel.

Survey Apparatus

Measurements of pitot pressure and downwash and sidewash angle were made in the flow fields behind the wing. The photograph of figure 2(b) illustrates the pitot rake, which consisted of eleven 0.040-inch-outside-diameter tubes mounted 3/16 inch apart in a vertical row. A 2-inch-outside-diameter tube (0.050-in. wall thickness) with its leading edge cut oblique to its longitudinal axis and beveled on the outside was the supporting strut. The complete rake could be traversed both spanwise and vertically with the tunnel in operation. The spanwise motion was accomplished by a lead screw directly coupled to a counter which indicated the spanwise position of the rake in the tunnel (1 count = 0.0025 in.), and the vertical motion was accomplished by a gear and rack at the rear end of the supporting strut. The vertical location was determined by sighting directly on a reference wedge with a cathetometer. It was necessary to stop the tunnel to change the longitudinal location.

The downwash and sidewash angles were obtained using a rake of small wedges such as is illustrated in the photograph of figure 2(c). Details of the construction of the individual wedges are illustrated in the sketches of figures 2(d) and 2(e). Because the smaller size wedges used during the tests at $M = 2.41$ responded too slowly to pressure changes, a larger version of the wedges was used for the tests at $M = 1.62$. With the larger wedges, it was necessary to increase the spacing of the wedges on the rake from 1/4 to 3/8 inch in order to prevent any interference effects between the wedges. The wedges were mounted on the rake alternately horizontally and vertically, such that they would measure downwash and sidewash, respectively. Also mounted on the rake was a small 1/16-inch-diameter mirror, which was used in conjunction with an external light source and a calibrated scale, for referencing the horizontal angle of the rake in the tunnel. The small 1-inch-long bar at the top of the rake was used for referencing the vertical angle of the rake in the tunnel, as it afforded a convenient surface on which to sight a cathetometer.

TESTS AND METHODS

Test Conditions

The surveys were conducted at free-stream Mach numbers of 1.62 and 2.41. At each Mach number the tunnel stagnation pressure was

adjusted to obtain data at two Reynolds numbers of 0.71×10^6
and 1.42×10^6 (based on the wing root chord which was the same for
all models).

The tunnel stagnation temperatures were around 95° F for the low-
pressure tests and 105° F for the high-pressure tests.

The moisture content of the tunnel air was sufficiently low for all
the tests such that any effects of condensation in the test section were
negligible.

Test Procedure

Schlieren studies.- Prior to making the detailed surveys, schlieren
studies were undertaken of wings of the same plan form as used in the
detailed surveys in order to obtain a general picture of the flow fields
(fig. 3). These tests were made at $M = 1.93$.

For all the schlieren tests, the knife edge was horizontal in order
to illustrate the density gradients in the vertical direction and thus
show the trails of the vortices.

The angles of attack of the tests were approximately the same as
the maximum angles of attack of the wings used for the surveys.

Side views and plan views of the flow patterns were photographed.
In the side views, the body was painted in a checkerboard fashion to
show up the location of the wing trailing edge. Two tiny wires were
stretched across the tunnel window to define the free-stream direction.
These can be seen in the plan view of figure 3(a) at about $1\frac{1}{2}$ semispans
from the body center line. The silhouettes in the lower left-hand corner
of all the side views of figure 3 merely serve to identify the plan form
of the wing being tested. (In fig. 3(b), this silhouette is rotated 90°
from its position in the other figures.)

Figure 4 shows the locations of the paths of high vorticity such as
were sketched from enlargements of figure 3, and are presented to aid in
the interpretation of the schlieren photographs.

Pitot pressure measurements.- The pitot tubes such as used in the
investigation are not sensitive to small differences in alinement between
the tube axis and the direction of the flow. For example, at $M = 1.62$,
calibrations have shown a misalinement of 5° is not discernible on the
pressure reading. For 10° misalinement, the error in H_3/H_{0_3} amounts to
about 1.3 percent. For this reason no provision or correction for the mis-
alinement of the pitot tubes with the local flow angle was made in the
present investigation.

The flow field was surveyed with the boundary-layer bypass plate installed, both with and without the wing. The longitudinal location of the crossflow planes that were surveyed were 1.5, 3, and 4 chords behind the wing trailing edge.

With the wing installed, the wing angle of attack was held constant while the pressure survey was conducted throughout each plane perpendicular to the free-stream direction. It was necessary to stop the tunnel in order to change the longitudinal location. While conducting a survey at a longitudinal station, the wing angle of attack was changed without stopping the tunnel, and the survey in the same crossflow plane was repeated. The wing angles of attack tested were -3°, 0°, and 3° for all the wings, plus two higher angles of attack. The highest angles tested were about 17° for the 72° sweptback triangular wing, about 14° for the 63° sweptback triangular wing, and about 12° for the others.

In making a survey of a crossflow plane at an assigned value of wing angle of attack and longitudinal location, the following procedure was used: The rake was set at a desired spanwise location, then moved vertically until one of its tubes registered the peak of minimum pressure in the viscous wake or vortex. The pressure and location data were then recorded.

With the rake at the same spanwise station, the vertical location was then changed by about one-half the distance between the tubes (3/32 in.), and the new data were taken. This was the usual procedure; however, in some cases where double peaks were observed in the wake profile, more than two vertical locations of the rake were used in order to define the wake profile more accurately. The spanwise stations selected for obtaining wake profiles were the same as those for which flow-angle measurements were made.

Flow-angle measurements.- The flow angle was determined by using the pressures, as measured on opposite sides of the previously described wedges, and the value of the pitot pressure at the same point. The sidewash and downwash were measured at the same point by taking measurements at two vertical locations of the rake. (The equal spacing of the six wedges on the rake in a vertical row alternately horizontally and vertically permitted this.) The tests were conducted in the same manner as for the pitot pressure measurements except that selected values of vertical location were used instead of searching for any peak value, as was the case with the pitot pressure measurements. Prior to observing and recording the vertical and horizontal location of the rake, the alinement of the rake in the tunnel both in the horizontal and vertical plane was checked by the referencing system described under Apparatus.

All flow-angle measurements were made at the desired locations, first with just the boundary bypass plate in the tunnel and no wing,

then with both the bypass plate and the wing in the tunnel. When the flow-angle values determined from the no-wing tests were subtracted from those with the wing present, the flow angle caused by the wing was obtained independent of any small variations in stream angle. Also, since the wedges were in the same position with respect to the rake for both the wing-on and the wing-off tests, the use of differences avoided the question of how accurately the angle of the small wedges with respect to the rake could be determined.

Data Reduction

The data were mechanically reduced and printed in the form of the ratio of the measured pressure to the tunnel stagnation pressure. All pitot pressure measurements are presented in this form; however, further reduction was necessary in order to obtain the downwash and sidewash. Figure 5 illustrates the type of chart that was used to obtain the downwash and sidewash. The dashed lines of this chart indicate the Mach number and flow angle with respect to the wedge axis for given pressure ratios such as two-dimensional wedge theory predicts. The ordinate P_w/H_3 (upper or outboard, depending on whether one is using a downwash or sidewash wedge) is the ratio of the pressure on the wedge to the measured pitot pressure (uncorrected for the normal shock at the nose of the tube). Similarly, the abscissa is this same pressure ratio for the opposite surface of the wedge. Knowing these pressure ratios and the wedge angle, the angle of the flow with respect to the wedge and the local Mach number can be determined. When the chart of figure 5 is used for the determination of flow angle, the parameters are very insensitive to changes in wedge angle. The maximum discrepancy between the chart of figure 5, which was constructed for an 8° half-wedge angle, and a chart which was constructed for a 7° half-wedge angle was less than 0.2° with regard to predicting the flow angle. However, with regard to predicting the Mach number, the parameters of the chart are very sensitive to wedge angle and since the wedges used for the tests of this report were so small that the wedge angle could not be accurately determined, no Mach number data are presented for the flow surveys.

Superimposed on the theoretical curves of figure 5 are the experimental points obtained when a typical wedge is varied through an angle-of-attack range at three different Mach numbers. The good agreement of the calibration with the theoretical lines of the chart at M = 2.41, with regard to predicting the flow angle, is shown. Consequently, the chart was used directly for reducing the flow-angle data at M = 2.41. At M = 1.62, the discrepancy between experiment and theory is larger than at M = 2.41. These discrepancies are probably due to a side-edge effect, although theoretically these effects should not start appearing until about 4° or 5° angle of attack of the wedge. Because of these

discrepancies, it was necessary to calibrate the wedge rake for the tests at M = 1.62. This was done at both tunnel stagnation pressures for which the tests were conducted, and the correction was applied to each individual wedge reading throughout the tests.

As previously stated, no Mach number data are presented. Comparing the experimental points with theory in figure 5, it is interesting to observe that even if the wedge angle were known exactly, the Mach number as indicated by the wedge theory would still be unreliable, since, in general, the experimental points indicate that the lines of constant Mach number on the chart are a different shape than predicted by theory.

Precision

The estimated accuracies of the controlled conditions during a test are as follows:

M . . . . ±0.01
α, deg . . . . ±0.1
x, in. 1/64
y, in. . . . . ±0.005
z, in. . . . . ±0.005

Checks between the values of the pressures as read directly, and the pressure ratios which were reduced mechanically, established a precision of ±0.003 for the H_3/H_{03} values. The precision of ϵ and σ, when estimated from the worst possible combination of inaccuracies in the pressures, with and without the wing present, reduce to ±0.4°. In the case of the flow-angle measurements, it should be further pointed out that for the tests at Mach number 1.62, an unknown source of error existed because of the fact that the calibration tests were conducted at Mach number 1.62, instead of at the particular local Mach number at which each wedge was operating. Throughout most of the flow field this error is probably negligible. A further source of an unknown effect on the precision of the flow-angle measurements results from how well the finite wedge sizes approximate a point measurement. Although the wedges were made as small as was practical, the results in a large pressure gradient might be subject to considerable inaccuracy due to this source. This would be especially true of the Mach number 1.62 tests of the 72° sweptback delta wing, where the wedge span is approximately 1/2 the wing span.

RESULTS AND DISCUSSION

Basic Data

Preliminary schlieren studies at M = 1.93.- Before commencing the detailed surveys behind the wings, schlieren observations, such as shown

in figure 3, were made at M = 1.93 in order to aid in planning the test program. In this figure, the primary object of interest is the regions of large changes in density in the vertical direction, such as accompany regions of concentrated vorticity. Although the free-stream Mach number is between the two Mach numbers for which the detailed surveys were made, the schlieren pictures serve to illustrate qualitatively what to expect with regard to the locations of the concentrated regions of vorticity behind the wings.

Although the wings are of the same plan form as the semispan wings for which the detailed surveys were made, they are smaller and are mounted on a slender body.

The angles of attack of the various wings were near the same theoretical lift coefficient in order to illustrate the variations in the flow patterns due primarily to aspect ratio. Observing the triangular wing plan forms of figures 3(a), 3(b), and 3(c), it is apparent that, for the lower-aspect-ratio wings, there is a more distinct and concentrated region of vorticity.

The paths of the main vortices behind the various triangular wings are shown in figure 4. This figure was sketched from enlarged versions of the schlieren pictures. For figures 4(a) and 4(b), where a wing shock was discernible, the location of this shock is shown as a solid line.

Since theoretical estimates of the flow angularity behind triangular wing configurations often approximate the flow fields using a line vortex which is located along the theoretical centroid of vorticity[1], the path of this streamline has been superposed in figure 4 for each wing. The discrepancy inherent in this assumption is apparent.

Pressure contours.- The data presentation is made in figures 6 to 32. The dashed lines of figures 6 to 32, which were constructed from the pitot pressure measurements, represent lines of constant pressure in the cross-flow planes for the various configurations tested. The numbers assigned to these contours are the ratio of the pressure as measured by the pitot tube to the tunnel stagnation pressure. Since the values were not corrected for the shock at the nose of the tube, the numbers given in the plots are not the true total pressure loss. The contours do give a good pictorial representation as to what is the nature of the flow field behind each wing. The z/b' location (y/b' axis) for all the figures is referenced to the wing trailing edge.

---

[1]The term "centroid of vorticity" will be used throughout the report to indicate the resultant weighted center of all the vorticity in a given region. It is analogous to the center of gravity of a similar system of point masses.

It can be seen that at approximately 0° angle of attack for all the
wings tested, there is a relatively flat sheet of low dynamic pressure
approximately straight behind the wing trailing edge. For the range
covered by the tests (1.5 to 4 chords behind the wing trailing edge),
the variation, both in shape and intensity, of the viscous wake with dis-
tance downstream is slight if any, (e.g., figs. 6(b) and 8(b)).

As the angle of attack of a wing is increased, the line of maximum
pressure deficiency deflects downward for inboard spanwise locations and
upward for the outboard locations (e.g., figs. 6(c), 6(d), 6(e), 7(a),
7(b), 8(c), and 8(d)). Also, at various spanwise locations along this
line, concentrations of lower dynamic pressure form. These are probably
concentrated regions of high vorticity which occur as the vorticity in
the vortex sheet redistributes itself. The formation of these regions
makes it difficult to trace the actual sheet of vorticity, or of minimum
total pressure, throughout its breadth as was possible at low angles of
attack. Actually, the interpretation of the vorticity existing as a
sheet becomes doubtful, since practically all the vorticity will be con-
tained in these concentrated regions. At the same angle of attack, it is
much easier to identify the existence of the vortex sheet as a sheet for
the higher-aspect-ratio wings than it is for lower. (For example, the
sheet is much more readily discernible in figure 6(d), or even 6(e), than
it is in the subsonic leading-edge configuration of figure 12(d), where
the vorticity is more concentrated. Similarly, at $M = 1.62$, the exist-
ence of the vortex sheet as a sheet is more apparent in figure 15(d) than
in figure 21(d)).

Downwash and sidewash.- In addition to the pressure contours, fig-
ures 6 to 32 present a vector presentation of the flow angles existing
in crossflow planes behind the various wings. The projection of a vector
on a vertical line is the downwash or upwash, and its projection on a
horizontal line is the sidewash. The length of each vector is referenced
from the center of each small circle, which is plotted at the location
for which the measurement was made. The magnitude of a 1° reference vec-
tor indicates a perturbation velocity sufficient to deflect the local
stream angles by 1° in the indicated direction. In some of the figures,
flow-angle data at the lower Reynolds number are shown as dashed vectors.
For those figures which show flow-angle data at both $R = 1.42 \times 10^6$
and 0.71×10^6, the pressure contours are for the higher Reynolds number.
Otherwise, the pressure contours are for the same Reynolds number as the
flow-angle data.

Although a more detailed and quantitative analysis will appear in
succeeding figures, the vector diagrams afford a good pictorial represen-
tation of the flow angles behind the wings, and illustrate some of the
following features of the flow.

At wing angles of attack of approximately zero degrees, the values of the flow angle which were measured are small. This indicates that the thickness effect is small for the thin wings of these tests.

At the same angle of attack, the largest vectors (largest flow angles) occur behind the lower-aspect-ratio wings. Also, there is a tendency for the intersection of the normals of the vectors for the lower-aspect-ratio wings to define a smaller region such as a theoretical model of the flow using a single-line vortex behind each wing panel would predict. For example, at $M = 2.41$, the flow behind the 50° sweptback triangular wing tends to circulate about the whole sheet of low pressure as defined by the pressure contours, figure 8(e), whereas the flow behind the 72° sweptback triangular wing tends to circulate about the small circular region of lowest pressure, which is defined by the pressure contours, figure 14(d) or 14(e). For all cases where this small low-pressure region exists, it is the vectors nearest this region that are largest and whose normals come closest to intersecting in this region. Those vectors which are farther away indicate that the path of the fluid is more distorted from a true circle.

No systematic variations due to Reynolds number were observed for the range tested. Minor differences in the high and low Reynolds number data (as for example, fig. 15(d), or comparing figs. 23(a) and 23(b) with figs. 24(a) and 24(b)) can be observed, but the vectors are very similar in size and direction so that the effects of the Reynolds number are apparently of a secondary nature.

Analysis

All wings at low angles of attack.- A summary of the low-angle-of-attack data is presented in the $-\partial\epsilon/\partial\alpha$ plots of figures 33 to 35. In these plots, values of $-\partial\epsilon/\partial\alpha$ below the zero axis are downwash, and values above are upwash. Each experimental point represents the slope of an ϵ agains α curve, which was drawn through the measured values of ϵ at wing angles of attack of approximately -3°, 0°, and 3°. Thus, the values are not necessarily the true value of $-\partial\epsilon/\partial\alpha$ near $\alpha = 0^\circ$, such as should be compared with the theoretical curves, but represent the average slope over a finite angle-of-attack range ($\pm 3^\circ$). The z/b' values quoted in these figures refer to the distance above and below the wing trailing edge at the root chord.

Because the point at which the downwash was being measured remained fixed, while the wing angle of attack was varied, the experimental values correspond to the physical case of the downwash at the tail behind a variable incidence wing, rather than the usual case where the measuring point is fixed referenced to the wing extended chord plane.

In figures 33 to 35, various theoretical calculations are presented. In these calculations the vortex sheet was assumed flat, undistorted, and located in the $\frac{z}{b'} = 0$ plane. Details of the various theoretical methods are presented in appendixes A to E.

Three theoretical estimates are presented in the plot on the left of figure 33(a) to compare with the experimental spanwise $-\partial\epsilon/\partial\alpha$ variation for a z/b' location of -0.049. This comparison is for the triangular wing whose leading edge is most supersonic[1] and for the longitudinal location which is closest behind the trailing edge ($x = 1.5c_r$). Because the experimental z/b' value was so near 0, the theoretical conical flow calculations were made at $\frac{z}{b'} = 0$ to facilitate computations. The agreement was poor and the conical flow method does not appear to give any better agreement than the less rigorous vortex methods. Further downstream, as in the plot on the right of figure 33(a), the infinite line vortices give closer agreement with experiment. This might be expected since any effect of chordwise loading becomes less important with distance downstream, and the assumption of infinite line vortices becomes more realistic. The theoretical estimate using horseshoe vortices shows this same trend of better agreement between theory and experiment with distance downstream.

As the wing aspect ratio is progressively decreased at a constant Mach number, the values of $-\partial\epsilon/\partial\alpha$, which are encountered, become more negative. (Compare figs. 33(a), 33(b), and 33(c).)

At a Mach number of 1.62, the same types of comparisons between experiment and theory are made in figure 34. The experimental curves at $x = 1.5c_r$ (left side of fig. 34(a)) show that the Reynolds number effect is small. The wing of this figure has a supersonic leading edge, although the leading-edge shock is detached. The agreement between infinite line vortex theory and experiment is not too good, nor does it improve much with distance downstream, as can be seen from the curves at the right of figure 34(a). Figures 34(b) and 34(c) are for wings whose leading edges are subsonic.

For the subsonic leading-edge wing of figure 34(c), theory and experiment are in good agreement close behind the wing ($x = 1.5c_r$). However, for the midspan portion of the wing, more negative experimental $-\partial\epsilon/\partial\alpha$ values are encountered than theory predicts, at the farther downstream station ($x = 4c_r$).

Figure 35(a) presents the spanwise $-\partial\epsilon/\partial\alpha$ variation for the reversed triangular wing. The theoretical loading for the wing is triangular and

---

[1]The terminology supersonic leading edge will be used throughout this report whenever the component of free-stream Mach number normal to the leading edge is supersonic (i.e., $M \cos \Lambda > 1$).

the equally spaced infinite line vortices give good agreement between
theory and experiment at both longitudinal stations.

Figure 35(b) presents the spanwise $-\partial\epsilon/\partial\alpha$ variation for the
straight 0-taper-ratio wing. For this wing, the spanwise $-\partial\epsilon/\partial\alpha$ varia-
tion resembles the variation as obtained for the triangular wings.

Subsonic leading-edge triangular wings at higher angles of attack.-
Because of the tendency for the vortex sheet behind the subsonic leading-
edge triangular wings to rapidly roll up into a single strong region of
vorticity (see vector plots), the use of a single bent-line vortex seemed
justifiable to represent the flow field behind the wing.

The proper location of this bent-line vortex, however, should be
examined. In order to study the vertical locations of the vortex sheet,
the plots in figures 36 to 38 show the vertical variation of the sidewash
for the three subsonic leading-edge triangular-wing configurations. The
experimental points were cross-plotted from curves of σ against span
for the various z/b' locations. Curves are shown in each of the plots
of these figures for two y/b' locations inboard of the theoretical
centroid of vorticity (which is located at about $0.8b'$). The missing
points near the peaks in figure 38(b), behind the lower side of the wing,
are not shown because the values were beyond the calibration curves of
the wedges, and although not presented, they are known to be greater than
10°.

The experimental curves of figures 36 to 38 are compared with theory,
which in this case was computed using a single bent-line vortex to repre-
sent the flow field. The bound portion of this line vortex was placed
along the wing center-of-pressure location, and the spanwise distance
between the semi-infinite legs of the vortex and the strength of the vor-
tex were determined from the theoretical span load curve. The expression
for the potential in the field of this bent-line vortex was taken from
reference 24 and differentiated with respect to y to obtain the side-
wash. (See appendix C.) The theoretical curves shown in figures 36
to 38 were all constructed assuming the vortex remained in the free-stream
direction with distance downstream. The horizontal arrow on each plot
denotes the z/b' location of the 0-sidewash point to which the theoreti-
cal curves may be shifted according to an over-all empirical correlation
based on the present set of data. This point will be discussed subse-
quently. Comparison of the theoretical and experimental curves of these
figures without performing this shift corresponds to the assumption that
the vortex follows the free stream from the wing trailing edge. The
improved agreement when the shift is performed can be visualized in these
figures. Furthermore, it can be seen that if the shift is performed, the
single bent-line vortex predicts the sidewash reasonable well.

The z/b' locations where the sidewash changes direction are plotted against the distance behind the wing trailing edge in figure 39. The square and diamond symbols on these curves came from figures 36 to 38. The circular symbols are the z/b' location of the vortex as obtained from the pressure contours.

The dashed curves in the plots of figure 39 are a side view of the paths of the vortices behind the wing, assuming they left the wing trailing edge and moved at an angle with the free-stream direction caused by the induced velocity from the vortex of the opposite panel. The angles ϕ and α referred to in figure 39 (also fig. 40) are illustrated in the following sketch:
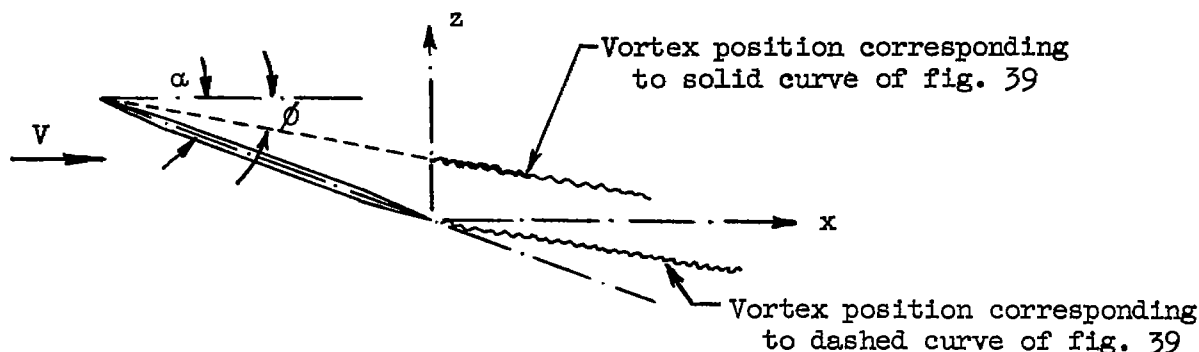
The solid curve of figure 39 is a line faired through an approximate average of the experimental points parallel to the dashed curve and having the same ϕ/α values at both angles of attack. The fact that this solid curve is above the wing trailing edge at $\frac{x}{b'} = 0$ might be expected, since previous experiments (for example, refs. 28 and 29) have established that for a subsonic leading-edge triangular wing, there is a leading-edge vortex formed above the upper wing surface. It would necessarily follow that the centroid of vorticity at a longitudinal station corresponding to the wing trailing edge is above the trailing edge. Such a conclusion is definitely indicated in figure 39 in spite of the scatter of test points. It is from the solid-line curve of figure 39 that the locations of the previously mentioned horizontal arrows of figures 36 to 38 were taken.

Since the slope of the solid-line curve of figure 39 can be predicted by theory, it would be possible to obtain a more accurate prediction of the flow field if the height of the starting point of this curve above the trailing edge could be predicted by theory. At the present time, a theoretical method for the prediction of the location of the leading-edge vortex above the wing surface is not available. Various attempts were

made to correlate the ϕ/α values as given by figure 39 with $\beta \cot \Lambda$, and the parameter selected as the ordinate in figure 40 plotted against $\beta \cot \Lambda$ appeared to give a reasonable variation. The complete elliptic integral of the second kind $(E(t'))$, occurring in this parameter comes from the expression for the lift coefficient of a subsonic leading-edge triangular wing. Although each experimental point of figure 40 represents two angle-of-attack conditions, there is in reality still too few points to generalize on this empirical relation. The chart of figure 40 is presented, however, as a preliminary approach to the problem since the data cover a fairly wide range of $\beta \cot \Lambda$ from a practical viewpoint as used in current missiles and since even an inaccurate correction for the height of the centroid of vorticity above the trailing edge will probably greatly improve estimates of the location of the line vortex at distances behind the wing.

The lack of any correction for the height of the centroid vorticity above the wing trailing edge was very noticeable in the plots of sidewash against span such as figures 41 and 42. Without the correction, theory and experiment were often of opposite sign. The theoretical curves that are shown in figures 41 and 42 were calculated using the correction for the height of the centroid of vorticity above the trailing edge as obtained from the solid line of figure 39.

In order to check the accuracy and the importance of making the correction for the vertical location of the line vortex as it leaves the wing trailing edge in the theoretical model of the flow, calculations of the tail efficiency for model BW_5OT_4 of reference 16 were made using the height of the vortex above the wing trailing edge as taken from figure 40. The calculations were made for a fixed wing-tail missile of this type but are not presented since the correction was negligible. This might be expected since, at higher angles of attack where the correction becomes sizeable, the location of the tail is too far from the line vortex to experience much difference in the downwash estimate acting on it. With a shorter tail arm the correction could become significant. Also, for the case of a missile with a variable incidence wing, the correction might prove important.

The lift data for a variable incidence wing configuration are illustrated in figure 43. The data, which are for the Sparrow 14-B configuration at Mach number 1.50, were taken from reference 30. The data shown in figure 43 are for a wing incidence of $8°$ relative to the body.

Figure 43 illustrates the relative importance of the components that enter into an accurate prediction of the stability characteristics of such a missile. The dashed theoretical curve represents the lift curve that would be predicted by the theory of reference 31 which considers all the interference lifts between the wing, body, and tail exclusive of the wing downwash effects. (The theory of ref. 31 was used since it permits

treating the case of a missile with a variable incidence wing.) This
theoretical curve should be compared with the experimental
$C_{L_{(BT-B)+BW}}$ curve, which is the experimental lift of the missile exclu-
sive of downwash effects.

The two dot-dashed curves are the resulting lift curves when the
downwash, as determined with and without the vertical displacement cor-
rection of the vortex, is applied. For a given downwash estimate, the
reverse-flow theorem was used to obtain the incremental tail lift, which
was in turn applied to the theoretical lift curve predicted by reference 31.
These two theoretical dot-dashed curves should be compared to the
$C_{L_{BWT}}$ curve.

In the estimate of the downwash, the line vortex from each wing panel
was allowed to deflect with distance downstream as in reference 32 (i.e.,
with an induced velocity as determined by the vortex from the opposite
panel, and the image vortices in the body, as well as the induced velocity
from the body crossflow). The only difference in the two curves is that
one included the vertical displacement correction at the wing trailing
edge and the other did not.

It is interesting to note that if the theory of reference 31 pre-
dicted the lift correctly, then near a body of angle of attack of zero
degrees, which is where the wing-alone data of this report are most appli-
cable, the theory using the displacement correction for the vertical
location of the vortex and the experimental $C_{L_{BWT}}$ curve would almost
coincide. At higher angles of attack, the use of the vertical displace-
ment correction to the theoretical downwash estimate gives poorer agree-
ment. If the theory underpredicted the downwash at large distances from
the vortex (i.e., the vorticity is more diffused and not concentrated in
a single line as assumed by the theory), then this poorer agreement might
be expected since the vertical displacement correction is predicting that
the vortex is farther from the tail than without the correction. There
are indications in figures 41 and 42 that, at large distances from the
vortex, theory tends to underpredict the downwash.

Supersonic leading-edge triangular wings at higher angles of attack.-
Although there doesn't appear to be an abrupt transition in the character
of the flow fields when the leading edge of a triangular wing goes from a
subsonic to a supersonic configuration, there is a difference in the types
of flow, in that, for comparable angles of attack, or even comparable lift
coefficients, the vorticity behind a supersonic leading-edge wing appears
as more than one region of strong vorticity or possibly still retains its
identity as a sheet. The 50° sweptback triangular wing at a Mach number
of 2.41 (the wing whose leading edge is most supersonic) was selected to
compare with the various theoretical techniques of predicting the flow
angles behind the wing, as the other supersonic leading-edge configurations

will be bracketed by this wing and the subsonic leading-edge wings. The comparison of figure 44 should best illustrate the advantages or disadvantages of the various theoretical methods. In this figure, the location of the experimental wake center line as determined from the pressure profiles is plotted as the circular symbols. Comparing the location of the vortex sheet, as determined by the various theories with the experimental location of the wake center line should give a good over-all picture in deciding on the merits of the various theoretical methods.

The location of the vortex sheet for the conical-flow theory was computed by calculating the downwash in the z = 0 plane at stations 0, 0.25, 0.50, 0.75, 1.0, 1.25, and 1.5 chords behind the wing trailing edge. Since $z = \int_0^x \frac{w}{V} dx \approx \int_0^x \epsilon \, dx$, plots of ϵ against x for given span stations, when mechanically integrated, determined the vertical locations of the vortex sheet that are shown in figure 44.

The location of the vortex sheet for the horseshoe-vortex theory was computed in the same manner as the conical-flow theory, except in the evaluation of the downwash at the various longitudinal locations, the horseshoe-vortex theory was used.

The square symbols of figure 44 show the locations of ten equal-strength infinite line vortices, whose resulting location was determined assuming they left the wing trailing edge with a lateral spacing in accordance with the theoretical wing span load distribution, and followed a path calculated in a step-by-step process (such as ref. 27), where each vortex moved vertically and laterally in accordance with the velocities induced by the other nineteen line vortices (considering both wing panels).

It can be seen in figure 44(a) that, at $x = 1.5c_r$, the two vortex-line methods bracket the experimental wake center-line location just as they did in the $-\partial\epsilon/\partial\alpha$ plots of figure 33. Behind the tip region, the infinite line vortices approximate very closely the experimental wake center-line location. On the other hand, conical-flow theory is in excellent agreement with experiment behind the inboard portion of the wing.

The agreement of the infinite-line-vortex theory with experiment behind the tip region and the agreement of the conical-flow theory behind the inboard portion of the wing (fig. 44(a)) suggests that a theoretical method employing a combination of the two methods might predict the actual flow field closely. For this combination theory, the vertical location of the vortex sheet was determined at points along Mach lines from the tip using conical-flow theory. With these locations as the starting points of the infinite line vortices, the method using infinite line vortices

was employed for distances farther downstream. Details of this method of calculation are given in appendix E.

In can be seen in figure 44 that this combination theory produces excellent agreement with experiment at the longitudinal station $(x = 1.5c_r)$ close to the intersection of the two Mach lines from the tip. Since the rolling-up process of the vortex sheet starts behind the tip (ref. 1), where the chordwise loading effects are small, the good agreement of the combination theory with experiment is not surprising. It uses the best features of both conical-flow and infinite-line-vortex theory. Actually any of the rigorous theories, which are exact within the linearizing approximations, such as the doublet theory of reference 25, could have been used instead of conical-flow theory with the same results.

Because of the tediousness of the method using the combination theory, the theoretical method using just the infinite line vortices has received the most emphasis in the comparisons between theory and experiment in this report. The advantage of using this seemingly more approximate method as compared to the planar methods is that the simple relation for the induced velocity in the field, from an infinite line vortex, permits the angle-of-attack effects (that is, the distortion of a vortex sheet) to be better approximated. However, wing chord loading effects are overlooked completely by the theory, as well as variations of Mach number in the wake itself with distance downstream. Also, in supersonic flow, the pressures or velocities experienced by a point in the field are influenced only by those disturbances in the Mach forecone from the point. The method used, which considered the induced velocities in successive crossflow planes has some justification, however, in that those line vortices closest to the point most strongly effect the velocities at the point.

It is realized that although the wing-alone tests of this report permitted theoretical calculations based on ten infinite line vortices from each wing panel, such calculations for the practical case of a wing and body would be too lengthy. However, the calculations were carried out, since the large number of line vortices permitted a study of the way they grouped themselves, and possibly would permit assigning strengths and locations to a fewer number of line vortices to obtain a better theoretical model of the flow, if agreement using the ten infinite line vortices could be obtained.

The theoretical paths of these infinite line vortices are shown in figure 45 by the dashed lines. The shapes of the vortex sheet at the various longitudinal stations are the solid curves. Theoretical (unpublished) and vapor-screen studies (ref. 17) of the vortex sheet made at the NACA Ames Laboratory have established the fact that for supersonic leading-edge delta wings the vortex sheet rolls up in a conventional manner behind the inboard section of the wing, and forms an "S" shaped pattern behind the triangular loaded tip region. In figure 45, vortices a, b,

and c illustrate the conventional rolling up, and the rest of the vortices
illustrate the formation of the "S" shaped pattern. In this figure, the
"S" shaped pattern becomes distorted farther downstream than about
$x/c_r = 2$. This is probably due to inaccuracies in graphically selecting
the initial locations of the line vortices and to the use of an insuffi-
cient number of streamwise increments in the computations. However, when
the paths for this particular wing were recomputed using more accurately
selected initial locations and smaller streamwise increments for the
entire range of calculations, the deformation of the "S" shaped structure
of the vortex sheet was still observed. This suggests that there is a
limit to how practical the method is, since at higher angles of attack,
and at larger distances behind the wing, smaller streamwise increments
would be required. In this connection, the patterns such as are shown
in figure 45 should be considered as rough approximations at large down-
stream distances. However, because of the practical limit to the method
for determining the shape of the vortex sheet, the accuracy with which
the flow angle can be predicted by the approximate patterns such as shown
in figure 45 may be of interest.

In figures 46(a) and 46(b), the experimental and theoretical downwash
and sidewash for this same wing at the same Mach number are compared using
the locations of the infinite line vortices as shown in figure 44, both
for the infinite-line-vortex theory and the combination theory. Near the
vortex sheet $\left(\frac{z}{b^{t}} = -0.075\right)$, the combination theory gives the best agree-
ment with the experimental spanwise downwash distribution as compared to
the theory using infinite line vortices; however, there is still consider-
able discrepancy. This discrepancy between theory and experiment is also
present at a z/b^{t} location farther from the vortex sheet $\left(\frac{z}{b^{t}} = 0.223\right)$.
The same statements apply to the sidewash in figure 46(b), except that,
for the spanwise range covered, the agreement between the combination
theory and experiment at $\frac{z}{b^{t}} = 0.223$ is excellent. Farther downstream
(figs. 46(e) and 46(f)) the line vortices have grouped themselves so close
together in many instances that, although the spanwise locations were
selected midway between line vortices, when evaluating the downwash and
sidewash, there are unreal variations in the theoretical curves, due to
the proximity of a vortex to the field point being calculated. All the
theoretical curves shown in figures 46(e) and 46(f) were based on the
infinite-line-vortex theory, and there is considerable discrepancy between
theory and experiment.

Reversed triangular wing at higher angles of attack.- One purpose of
using the ten infinite line vortices for the theoretical calculations of
all the supersonic leading-edge wings, analysed in this report, was to
study their behavior as they moved downstream. This possibly would per-
mit a better assignment of strength and locations to a fewer number of
line vortices to be applied to the wing-body problem. For the reversed

triangular wing the span loading is triangular and the ten equal-strength vortices are also equally spaced. The tendency for the vortices to divide into two separate groups was particularly evident. (See fig. 47.) Whether such a result would take place if many more streamwise increments had been used in the computations is not certain. Since the experimental pressure contours (figs. 28(d) and 29(d)) exhibit a tendency for the sheet to form concentrated regions of vorticity, the arrangement of the vorticity shown in figure 47 probably represents a good approximation of the arrangement of the vortex sheet. The separation of the sheet into these two regions suggests that a model of the flow with two vortices from each wing panel would be a simpler representation of the flow. The outboard vortex should have a strength $0.6\Gamma_m$ (six line vortices are in the outer group) and the inner vortex would have a strength of $0.4\Gamma_m$. This model of the flow (though probably considerably better than a single vortex) was not further investigated since it would be a cruder model of the flow than the theoretical method using ten line vortices.

The theoretical prediction of the downwash and sidewash using ten line vortices are compared in figure 48. For this case, although the same shapes of the curves are evident in both experiment and theory, the agreement is not too good. It is obvious in figure 48, however, that the method used, predicts the downwash better than would a single line vortex from each wing panel since with a single line vortex the downwash would change sign at $\frac{y}{b'} = 0.5$. Both experiment and the theoretical method using ten line vortices show that the spanwise location where the downwash changes sign is outboard of $\frac{y}{b'} = 0.5$.

O-taper-ratio wing $\left(\Lambda = -\Lambda_{TE} = 50^\circ\right)$ at higher angles of attack.- The theoretical paths of the ten infinite line vortices behind a straight O-taper-ratio wing are shown in figure 49. The vortex sheet appears to roll up in the conventional manner. The leading edge of the wing is slightly supersonic at this Mach number but the shock is detached even at $\alpha = 0^\circ$. The pressure contours (fig. 32(d)) show three regions of apparently higher vorticity along the vortex sheet, but the two inboard regions are so much weaker than the one which remains straight behind the point on the wing at $0.8b'$, that the flow picture can be assumed to be the conventional rolling-up pattern indicated by the theoretical calculations of figure 49.

The spanwise downwash and sidewash distributions for the straight O-taper-ratio wing are shown in figure 50. Also shown are the theoretical curves to be compared with the appropriate experimental curve. The theoretical curves were computed using the locations of the infinite line vortices such as shown in figure 49 for the appropriate streamwise location. The agreement between experiment and theory is poor.

CONCLUSIONS

Schlieren studies, pitot-pressure profiles, and flow-angle surveys were made behind five, thin, pointed-tip wings. The flow behind three triangular wings of 50°, 63°, and 72° leading-edge sweep angle was surveyed at Mach numbers 1.62 and 2.41. The flow behind a reversed triangular wing (-50° trailing-edge sweep angle) and a 0-taper-ratio wing $\left(\Lambda = -\Lambda_{TE} = 50°\right)$ was surveyed at Mach number 1.62. The analysis of the data and comparison of the results with theoretical predictions indicated the following conclusions:

1. The vortex sheet behind triangular wings with subsonic leading edges tends to rapidly form itself into one distinct region of high vorticity behind the wing as it moves downstream, as in the case for triangular wings in subsonic flow. For subsonic leading-edge triangular wings at moderate and high angles of attack, the use of a single bent-line vortex to represent the flow field agrees with the physical picture and predicts the downwash and sidewash reasonably well if its location can be estimated with sufficient accuracy. A proposed empirical adjustment of the method for determining vertical location of this line vortex at stations behind the wing gives a good representation of the flow field (particularly the sidewash).

2. For triangular wings with supersonic leading edges, the flow tends to rotate more about a sheet of vorticity, which still retains its identity as a sheet at·lift coefficients and downstream distances comparable to subsonic leading-edge wings. The vortex sheet itself appeared to have more than one region of high vorticity along any semispan of its width. At moderate angles of attack (12°), a lifting-surface theory such as conical-flow theory best predicts the location of the vortex sheet near the plane of symmetry, whereas using infinite line vortices and a step-by-step process best predicts the location of the vortex sheet behind the tip region. Using a combination of the two methods gave an accurate representation of the vortex sheet at a longitudinal station 1.5 chords behind the trailing edge (near the location where the Mach lines from the tip intersect), and improved the agreement of the theoretical and experimental downwash and sidewash. The method was not evaluated at stations farther behind the wing, since the number of line vortices and the smallness of the streamwise increments would probably cause the method to become too cumbersome for a practical wing-body problem.

3. For the reversed triangular wing both experiment and the theory using ten infinite line vortices exhibited a tendency for the vortex sheet to concentrate into two regions with the outboard region containing the most vorticity. The actual prediction of the flow angles was poor at moderately high angles of attack, although the curves of the experimental and theoretical spanwise downwash and sidewash distributions appeared to have the same shape.

4. For the 0-taper-ratio plan-form wing with a leading edge that
was only slightly supersonic, the vortex sheet rolled up in a conventional
subsonic manner in the theoretical calculations and, neglecting a couple
of weak inboard concentrations of vorticity, the same pattern was evident
in the experimental flow. However, the actual prediction of the flow
angle was poor.

Langley Aeronautical Laboratory,
      National Advisory Committee for Aeronautics,
          Langley Field, Va., January 22, 1954.

APPENDIX A

DETAILS OF CONICAL-FLOW METHOD

The calculation of downwash and sidewash behind a wing at supersonic speeds using conical flows has been presented in references 20 to 22. The principle of the method depends on the fact that when the downwash or sidewash is known for certain specified plan forms, other plan forms can be formed by the superposition of these known plan forms. The resulting downwash or sidewash is then the combined effect of the known solutions. An example follows for the supersonic leading-edge triangular wing.

The upwash at any point in the field (x,y,z) due to an infinite triangular wing can be found from the charts of reference 34. $\left(\text{For } z = 0, \dfrac{-\partial\epsilon}{\partial\alpha} = \dfrac{w}{\alpha V} = -1\right)$. The sketches shown in this appendix illustrate the steps that are required in order to cancel the lifting pressures of an infinite triangular wing, at a desired x location, which is to be the trailing edge of the wing. For each plan form, the corresponding resulting pressure distribution, as a result of the particular step involved, is also shown by the solid lines. The dashed lines indicate the canceling pressure which is being applied. All pressures refer to the upper-surface pressure only. The expressions for u and u_0 shown in sketch I

Pressure distribution
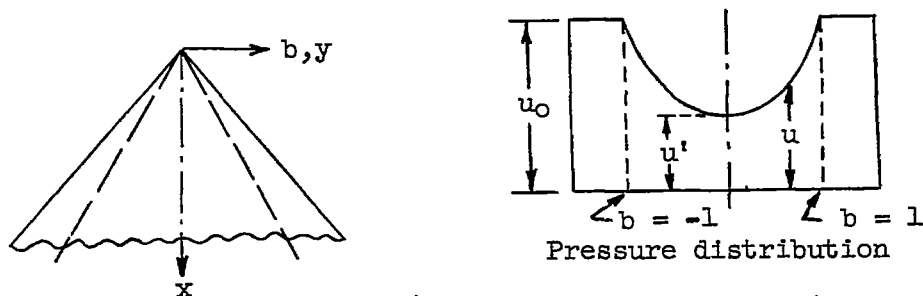
SKETCH I. (Infinite Triangular Wing)

can be obtained from reference 35, and are

$$u_0 = \frac{\alpha V}{\beta\sqrt{1 - \dfrac{a^2}{\beta^2}}} \tag{A1}$$

$$\frac{u}{u_0} = \frac{1}{\pi} \cos^{-1}\left[1 + \frac{2\left(\frac{a^2}{\beta^2} - 1\right)}{1 - a^2\left(\frac{b}{x}\right)^2}\right] \qquad (A2)$$

Sketch II illustrates the addition of wing A which is at constant pressure u' and cancels the pressures as shown in the following sketch:

Pressure distribution at x_1
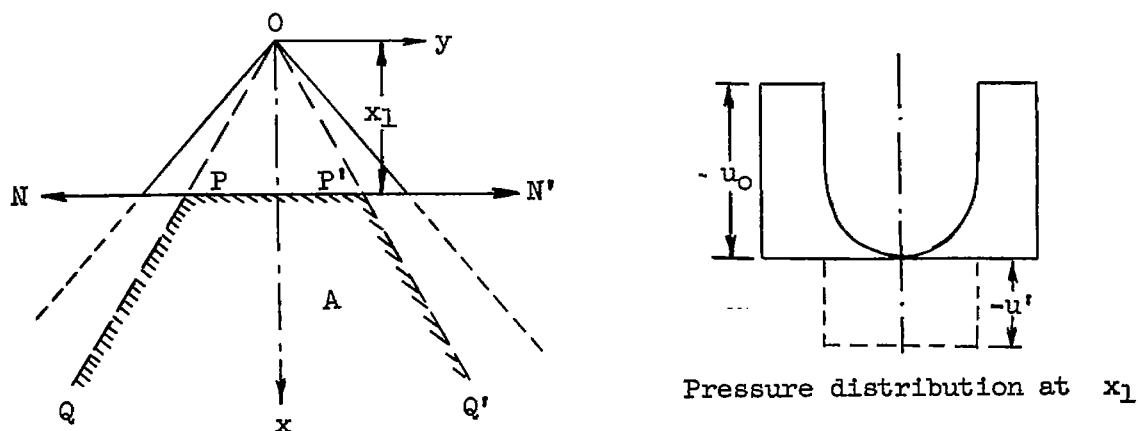
Sketch II.

Wing A is formed by subtracting two conical wings, N,P,Q and N',P',Q', from a two-dimensional wing. In the sketch, N,Q,Q', and N' are at infinity in the designated direction. Using the expressions for the $G(-1,r,\theta)$ and $G(1,r,\theta)$ functions that are given in reference 20, the resulting upwash in the $z = 0$ plane due to wing A is

$$\frac{w}{V_\alpha} = -1 - \left[G(-1,r,\theta)\frac{u'}{m} + G(1,r,\theta)\frac{u'}{m}\right] \qquad (A3)$$

Sketch III illustrates the process whereby conical wings each of a different constant pressure are used to cancel the pressure between the two Mach lines from the apex:

Pressure distribution at x_1
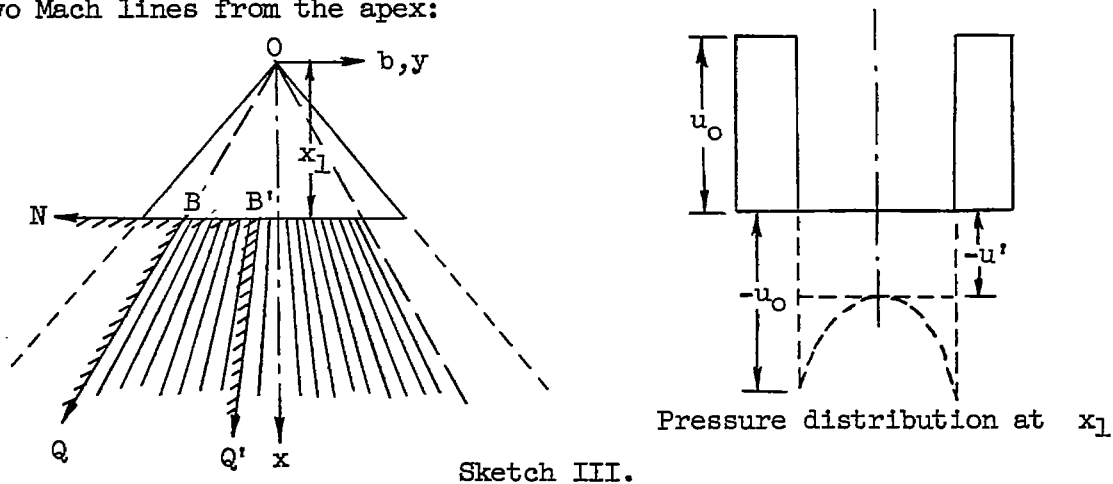
Sketch III.

The upwash due to a typical conical wing Q,B,B',Q' is formed by subtracting the upwash due to two conical wings at the same pressure u, that is, wing N,B',Q' minus wing N,B,Q. The resulting expression for the upwash due to the canceling wings in sketch III is

$$\frac{w}{\alpha V} = -\beta \left\{ \int_0^{-1} \left[G(-b,r,\theta) - G(-1,r,\theta) \right] \frac{du}{db} \right\} db +$$

$$\beta \left\{ \int_0^1 \left[G(b,r,\theta) - G(1,r,\theta) \right] \frac{du}{db} \right\} db \qquad (A4)$$

The expressions for the $G(b,r,\theta)$ functions are given in reference 20 and

$$\frac{du}{db} = \frac{2\alpha Vab}{\pi \beta^2 \left(1 - \frac{a^2}{\beta^2} b^2 \right) \sqrt{1 - b^2}} \qquad (A5)$$

The integration was performed mechanically using ten wings for each half of the conical field between the Mach lines.

Sketch IV illustrates the final step in canceling the pressures (u values) everywhere downstream of the wing trailing edge:

Pressure distribution at x_1
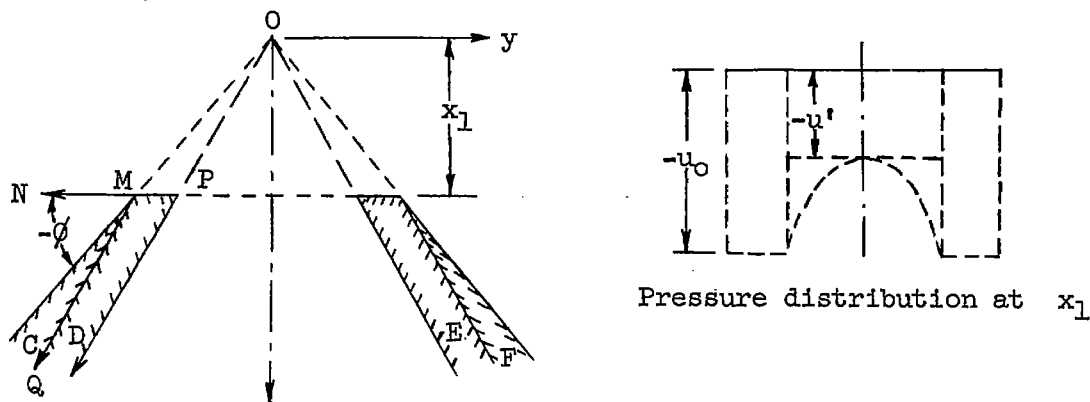
Sketch IV.

Wings C + D and E + F are at constant pressure u_0. The expression for the downwash due to wings C and F may be obtained from reference 21. The expression, as is given in reference 21, is for $M = \sqrt{2}$. When the Mach number terms are reinstalled, the expression as applied to wing C is

$$G''(-1,r,\theta) = \frac{w}{\alpha V}$$

$$= \frac{1}{\pi}\left[\cot \beta + \frac{\tan(-\phi)}{\beta}\right] \log R -$$

$$\sqrt{1 - \frac{\tan^2(-\phi)}{\beta^2}}\left\{\tan^{-1} \frac{2\sqrt{1 - \frac{\tan^2(-\phi)}{\beta^2}}\left[R \cos \theta + \frac{\tan(-\phi)}{\beta}\right]}{R^2 - 1 + \frac{2\tan^2(-\phi)}{\beta^2} + \frac{2R}{\beta} \cos \theta \tan(-\phi)} - \right.$$

$$\left. \tan^{-1} \frac{\sqrt{1 - \frac{\tan^2(-\phi)}{\beta^2}}}{\frac{\tan(-\phi)}{\beta}}\right\} \tag{A6}$$

The symbols are defined in reference 21 or reference 20, where, for $z = 0$,

$$R = \frac{1 - \sqrt{\frac{x^2}{\beta^2} - y^2}}{y}$$

and $\theta = 0^\circ$ or 180°.

In applying formula (A6) to the calculation of upwash due to wings C and F of sketch IV, the axis must be shifted to M and N (that is, define the field points x, y, and z with respect to M and N instead of with respect to O). The upwash due to wings D and E of sketch IV was also determined by a ruse which employed a shift in the y coordinates of the field points, for which the upwash was being calculated, by the distance MP. For wing D, the upwash was that of the conical wing N,P,Q' minus the conical wing N,M,Q, where the wing N,M,Q was determined from the $G'(-1,r,\theta)$ function based on the shifted y coordinates of the field points; that is (due to wings D and E),

$$\frac{w}{V_\alpha} = \beta u_o \Big[G(-1,r,\theta) - G'(-1,r,\theta) \Big] + \beta u_o \Big[G(1,r,\theta) - G'(1,r,\theta) \Big] \tag{A7}$$

After the evaluation of all of the above component contributions to the upwash, the final value for the upwash as obtained at any field point was merely the algebraic sum. Previously constructed charts for all the G functions greatly expedited the calculations. The case of the supersonic leading-edge wing, which is illustrated, is the most tedious. For subsonic leading-edge wings, it is necessary to carry the calculations only through the steps illustrated in sketchs I, II, and III.

APPENDIX B

Details of Horseshoe-Vortex Method

The estimation of the downwash and sidewash behind triangular wings using horseshoe-vortex theory is one of the methods described in reference 24. The theoretical model of the flow suggested in reference 24, which places the corners of the horseshoe vortices along a line representing the center of pressure of the triangular wing, was tried. Also, a different theoretical representation which placed the corners of the horseshoe vortices in equal x increments (although they might fall off the wing plan form) was tried. The difference in the downwash, as calculated by the two methods, was very slight. All the theoretical curves presented in this report, which used horseshoe vortices, were calculated by the latter method.

APPENDIX C

DETAILS OF SINGLE-BENT-LINE-VORTEX METHOD

For the low-aspect-ratio triangular wings, a single bent-line vortex physically approximates the flow field. The expression for the upwash, which is given explicitly in reference 1, was used in this paper for those theoretical calculations where the theoretical model of the flow was a single bent-line vortex. In order to obtain the expression for the sidewash due to a single bent-line vortex, the expression for the potential as given in reference 24 was differentiated with respect to y. The resulting equation is

$$\frac{2\pi v}{\Gamma} = z \left\{ \frac{\left[(y - y_o)\left(x - \frac{y + k}{m}\right) - \frac{z^2}{m}\right]\left[\dfrac{-\beta^2\left(y^2 - y_o{}^2\right)}{\sqrt{\left(x - \frac{y_o + k}{m}\right)^2 - \beta^2(y - y_o)^2 - \beta^2 z^2}}\right]}{\left[(y - y_o)\left(x - \frac{y + k}{m}\right) - \frac{z^2}{m}\right]^2 + z^2\left[\left(x - \frac{y_o + k}{m}\right)^2 - \beta^2(y - y_o)^2 - \beta^2 z^2\right]} \right.$$

$$\left. \frac{\sqrt{\left(x - \frac{y_o + k}{m}\right)^2 - \beta^2(y - y_o)^2 - \beta^2 z^2}\left[x - \left(\frac{2y + k - y_o}{m}\right)\right]}{\left[(y - y_o)\left(x - \frac{y + k}{m}\right) - \frac{z^2}{m}\right]^2 + z^2\left[\left(x - \frac{y_o + k}{m}\right)^2 - \beta^2(y - y_o)^2 - \beta^2 z^2\right]} \right\}.$$

$$z \left\{ \frac{\left[(y - y_o)\left(x + \frac{y - k}{m}\right) + \frac{z^2}{m} \right]\left[\dfrac{-\beta^2(y + y_o)}{\sqrt{\left(x - \frac{y_o + k}{m}\right)^2 - \beta^2(y + y_o)^2 - \beta^2 z^2}} \right]}{\left[(y + y_o)\left(x + \frac{y - k}{m}\right) + \frac{z^2}{m} \right]^2 + z^2\left[\left(x - \frac{y_o + k}{m}\right)^2 - \beta^2(y + y_o)^2 - \beta^2 z^2 \right]} - \right.$$

$$\left. \frac{\sqrt{\left(x - \frac{y_o + k}{m}\right)^2 - \beta^2(y + y_o)^2 - \beta^2 z^2}\,(mx + 2y - k + y_o)}{\left[(y + y_o)\left(x + \frac{y - k}{m}\right) + \frac{z^2}{m} \right]^2 + z^2\left[\left(x - \frac{y_o + k}{m}\right)^2 - \beta^2(y + y_o)^2 - \beta^2 z^2 \right]} \right\} +$$

$$\frac{mz\left[\dfrac{y(mx + y - k) + z^2\left(-\beta^2 y\right)}{\sqrt{\left(x - \frac{k}{m}\right)^2 - \beta^2\left(y^2 + z^2\right)}} - (mx + 2y - k)\sqrt{\left(x - \frac{k}{m}\right)^2 - \beta^2\left(y^2 + z^2\right)} \right]}{\left[y(mx + y - k) + z^2 \right]^2 + m^2 z^2\left[\left(x - \frac{k}{m}\right)^2 - \beta^2\left(y^2 + z^2\right) \right]} -$$

$$\frac{mz\left[\dfrac{\left[y(mx - y - k) - z^2 \right]\left(-\beta^2 y\right)}{\sqrt{\left(x - \frac{k}{m}\right)^2 - \beta^2\left(y^2 + z^2\right)}} - (mx - 2y - k)\sqrt{\left(x - \frac{k}{m}\right)^2 - \beta^2\left(y^2 + z^2\right)} \right]}{\left[y(mx - y - k) - z^2 \right]^2 + m^2 z^2\left[\left(x - \frac{k}{m}\right)^2 - \beta^2\left(y^2 + z^2\right) \right]}$$

where x, y, z, k, x_0, and y_0 are defined in the following sketch:
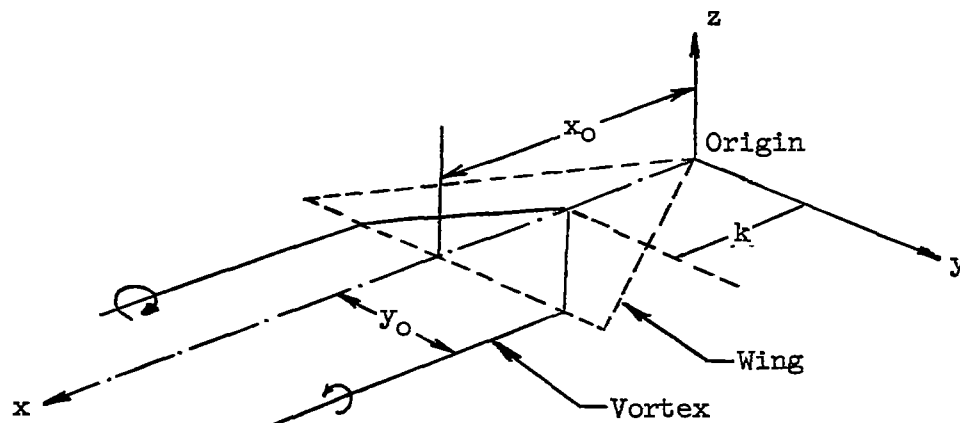
APPENDIX D

DETAILS OF INFINITE-LINE-VORTEX METHOD

At angles of attack where the deflection and the distortion of the vortex sheet behind a wing becomes important, yet where the wing aspect ratio is too high, or the distance behind the wing too short to represent the vorticity behind the wing with a single bent-line vortex, a method such as was used in reference 27 was employed to estimate the shape of the vortex sheet and to approximate the resulting downwash and sidewash. The equivalence of the supersonic and the incompressible line vortex, when both have zero slope, was pointed out in reference 23. The simple relation for the induced tangential velocity at points in the field of an infinite line vortex is

$$v_T = \frac{\Gamma}{2\pi r} \tag{D1}$$

or, as used in this paper,

$$\left. \begin{array}{l} \dfrac{wb'}{\Gamma} = \dfrac{\dfrac{y}{b'}}{\sqrt{\left(\dfrac{y}{b'}\right)^2 + \left(\dfrac{z}{b'}\right)^2}} \\[40pt] \dfrac{vb'}{\Gamma} = \dfrac{\dfrac{z}{b'}}{\sqrt{\left(\dfrac{y}{b'}\right)^2 + \left(\dfrac{z}{b'}\right)^2}} \end{array} \right\} \tag{D2}$$

The simplicity of these expressions permitted the use of an iteration procedure, such as used in reference 27, to approximate the location and shape of the vortex sheet.

APPENDIX E

DETAILS OF THE METHOD FOR THE COMBINATION OF THE CONICAL-FLOW

AND THE INFINITE-LINE-VORTEX THEORIES

The region between the two Mach lines from the tips was taken as an
arbitrary range of applicability of conical-flow theory. The deflection
of the vortex sheet above or below the reference streamwise plane was
computed at various span stations using conical-flow theory. These
locations correspond to points a through j in the following sketch:
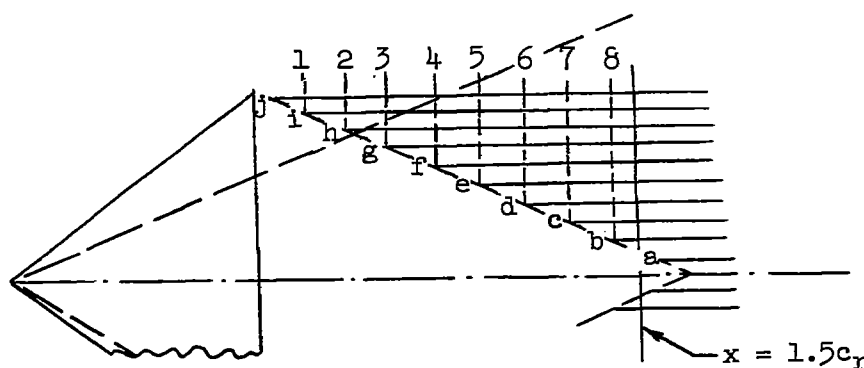
The spanwise locations of points a through j were determined from the
wing span load distribution in the same manner as was used for setting up
the infinite-line-vortex calculations.

With the location of points a through j as the starting points
of the infinite line vortices, the induced velocities and corresponding
paths of each vortex were computed in the same step-by-step manner (from
station 1, to 2, to 3, etc.) as was used for the calculations using
infinite line vortices alone. However, only those vortices which were
actually present at any longitudinal station were considered to have any
effect on the adjacent line vortices. (For example, at station 5, the
total induced velocity on g was the sum of the induced velocities from
e, f, h, i, and j.)

REFERENCES

1. Sprieter, John R., and Sacks, Alvin H.: The Rolling Up of the Trailing Vortex Sheet and Its Effect on the Downwash Behind Wings. Jour. Aero. Sci., vol. 18, no. 1, Jan. 1951, pp. 21-32, 72.

2. Perkins, Edward W., and Canning, Thomas N.: Investigation of Downwash and Wake Characteristics at a Mach Number of 1.53. I — Rectangular Wing. NACA RM A8L16, 1949.

3. Perkins, Edward W., and Canning, Thomas N.: Investigation of Downwash and Wake Characteristics at a Mach Number of 1.53. II — Triangular Wing. NACA RM A9D20, 1949.

4. Adamson, D., and Boatright, William B.: Investigation of Downwash, Sidewash, and Mach Number Distribution Behind a Rectangular Wing at a Mach Number of 2.41. NACA RM L50G12, 1950.

5. Cummings, John L., and Haefeli, Rudolph C.: Downwash in Vortex Region Behind Rectangular Half-Wing at Mach Number 1.91. NACA RM E50H10, 1950.

6. Davis, Theodore: Experimental Investigation of Downwash and Sidewash Behind a Rectangular Wing at a Mach Number of 1.60. Meteor Rep. UAC-45, United Aircraft Corp., Jan. 1950.

7. Walker, Harold J., Stivers, Louis S., Jr., and Beard, Luther, Jr.: Experimental Downwash and Wake Characteristics at Subsonic and Supersonic Mach Numbers Behind an Unswept Tapered Wing of Aspect Ratio 2.67 with Leading- and Trailing-Edge Flaps. NACA RM A51B16, 1951.

8. Cummings, J. L., Mirels, H., Baugham, L. E.: Downwash in Vortex Region Behind Trapezoidal-Wing Tip at Mach Number 1.91. NACA RM E9H15, 1949.

9. Perkins, Edward W., and Canning, Thomas N.: Investigation of Downwash and Wake Characteristics at a Mach Number of 1.53. III — Swept Wings. NACA RM A9K02, 1950.

10. Walker, Harold J., and Stivers, Louis S., Jr.: Investigation of the Downwash and Wake Behind a Triangular Wing of Aspect Ratio 4 at Subsonic and Supersonic Mach Numbers. NACA RM A50I14a, 1950.

11. Schindel, Leon H., and Durgin, Frank H.: Survey of the Downwash Field Behind Rectangular, Trapezoidal, and Delta Wings at Mach Numbers 1.71, 1.99, and 2.50. Wind Tunnel Rep. No. 29 (Bur. Aero. Contract NOas 52-551-c), M.I.T., Naval Supersonic Lab.) Mar. 1953.

12. Grant, Frederick C., and Gapcynski, John P.: An Investigation of a
    Supersonic Aircraft Configuration Having a Tapered Wing With
    Circular-Arc Sections and 40° Sweepback. Estimated Downwash Angles
    Derived From Pressure Measurements on the Tail at Mach Numbers of
    1.40 and 1.59. NACA RM L51L17, 1952.

13. Wetzel, Benton E., and Pfyl, Frank A.: Measurements of Downwash and
    Sidewash Behind Cruciform Triangular Wings at Mach Number 1.4.
    NACA RM A51B20, 1951.

14. Wise, George A., and Dryer, Murray: Influence of a Canard-Type Con-
    trol Surface on Flow Field in Vicinity of Symmetrical Fuselage at
    Mach Numbers 1.8 and 2.0. NACA RM E52E13, 1952.

15. Boatright, William B.: Total-Pressure and Schlieren Studies of the
    Wakes of Various Canard Control Surfaces Mounted on a Missile Body
    at Mach Number of 1.93. NACA RM L52I29, 1952.

16. Grigsby, Carl E.: The Use of the Rolled-Up Vortex Concept for Pre-
    dicting Wing-Tail Interference and Comparison With Experiment at
    Mach Number of 1.62 for a Series of Missile Configurations Having
    Tandem Cruciform Lifting Surfaces. NACA RM L52H05, 1952.

17. Spahr, J. Richard, and Dickey, Robert R.: Wind-Tunnel Investigation
    of the Vortex Wake and Downwash Field Behind Triangular Wings and
    Wing-Body Combinations at Supersonic Velocities. NACA RM A53D10,
    1953.

18. Fradenburgh, Evan A., Obery, Leonard J., and Mello, John F.: Influ-
    ence of Fuselage and Canard-Type Control Surface on the Flow Field
    Adjacent to a Rearward Fuselage Station at a Mach Number of 2.0.
    Data Presentation. NACA RM E51K05, 1952.

19. Weil, Joseph, Campbell, George S., and Diederich, Margaret S.: An
    Analysis of Estimated and Experimental Transonic Downwash Character-
    istics as Affected by Plan Form and Thickness for Wing and Wing-
    Fuselage Configurations. NACA RM L52I22, 1952.

20. Lagerstrom, P. A., Graham, Martha E., and Grosslight, G.: Downwash
    and Sidewash Induced by Three-Dimensional Lifting Wings in Super-
    sonic Flow. Rep. No. SM-13007, Douglas Aircraft Co., Inc.,
    Apr. 14, 1947.

21. Lagerstrom, P. A.: Linearized Supersonic Theory of Conical Wings.
    NACA TN 1685, (Corrected copy) 1950.

22. Buseman, A.: Infinitesimal Conical Supersonic Flow. NACA TM 1100,
    1947.

23. Mirels, Harold, and Haefeli, Rudolph C.: Line-Vortex Theory for Calculation of Supersonic Downwash. NACA Rep. 983, 1950.

24. Martin, John C.: The Calculation of Downwash Behind Wings of Arbitrary Plan Form at Supersonic Speeds. NACA TN 2135, 1950.

25. Heaslet, Max A., and Lomax, Harvard: The Calculation of Downwash Behind Supersonic Wings With Application to Triangular Plan Forms. NACA TN 1620, 1948.

26. Harmon, Sidney M.: Method for Calculating Downwash Field Due to Lifting Surfaces at Subsonic and Supersonic Speeds. NACA TN 2344, 1951.

27. Westwater, F. L.: Rolling Up of the Surface of Discontinuity Behind an Aerofoil of Finite Span. R. & M. No. 1692, British A.R.C., 1935.

28. Boyd, John W., and Phelps, E. Ray: A Comparison of the Experimental and Theoretical Loading Over Triangular Wings at Supersonic Speeds. NACA RM A50J17, 1951.

29. Hatch, John E., Jr., and Hargrave, L. Keith: Effects of Reynolds Number on Aerodynamic Characteristics of a Delta Wing at a Mach Number of 2.41. NACA RM L51H06, 1951.

30. Beal, R. R.: Analysis of Force and Moment Characteristics From Supersonic Wind-Tunnel Tests of a 13.5-Percent-Scale Model of the Sparrow 14-B at Mach Number = 1.50 Including the Effects of Systematic Variations of Wing Planform. Rep. No. SM-20175, Douglas Aircraft Co., Inc., Aug. 31, 1951.

31. Tucker, Warren A.: A Method for Estimating the Components of Lift of Wing-Body Combinations at Supersonic Speeds. NACA RM L52D22, 1952.

32. Lagerstrom, P. A., and Graham, M. E.: Aerodynamic Interference in Supersonic Missiles. Rep. No. SM-13743, Douglas Aircraft Co., Inc., July 1950.

33. Nielson, Jack N., and Perkins, Edward W.: Charts for the Conical Part of the Downwash Field of Swept Wings at Supersonic Speeds. NACA TN 1780, 1948.

34. Lagerstrom, P. A., Wall, D., and Graham, M. E.: Formulas in Three-Dimensional Wing Theory. Rep. No. SM-11901, Douglas Aircraft Co., Inc., July 8, 1946.
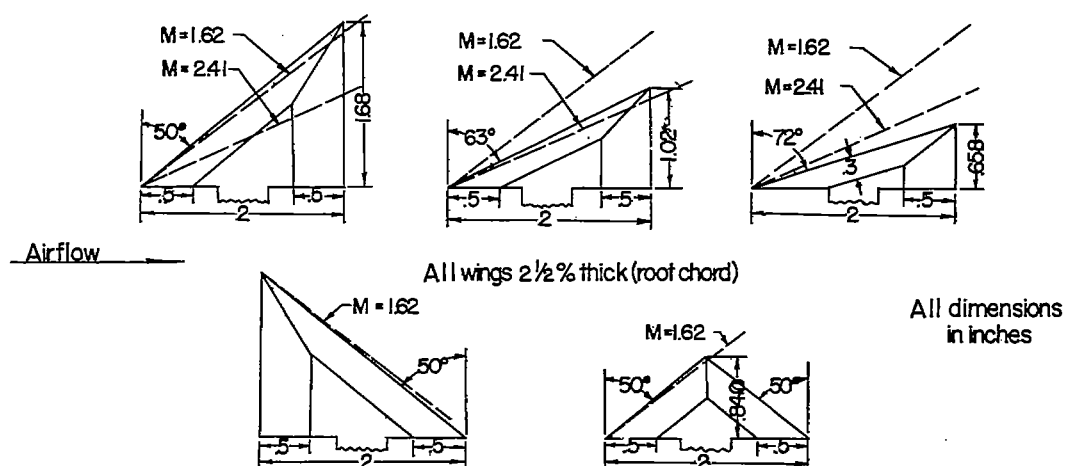
(a) Wing models illustrating Mach cone leading-edge configuration.
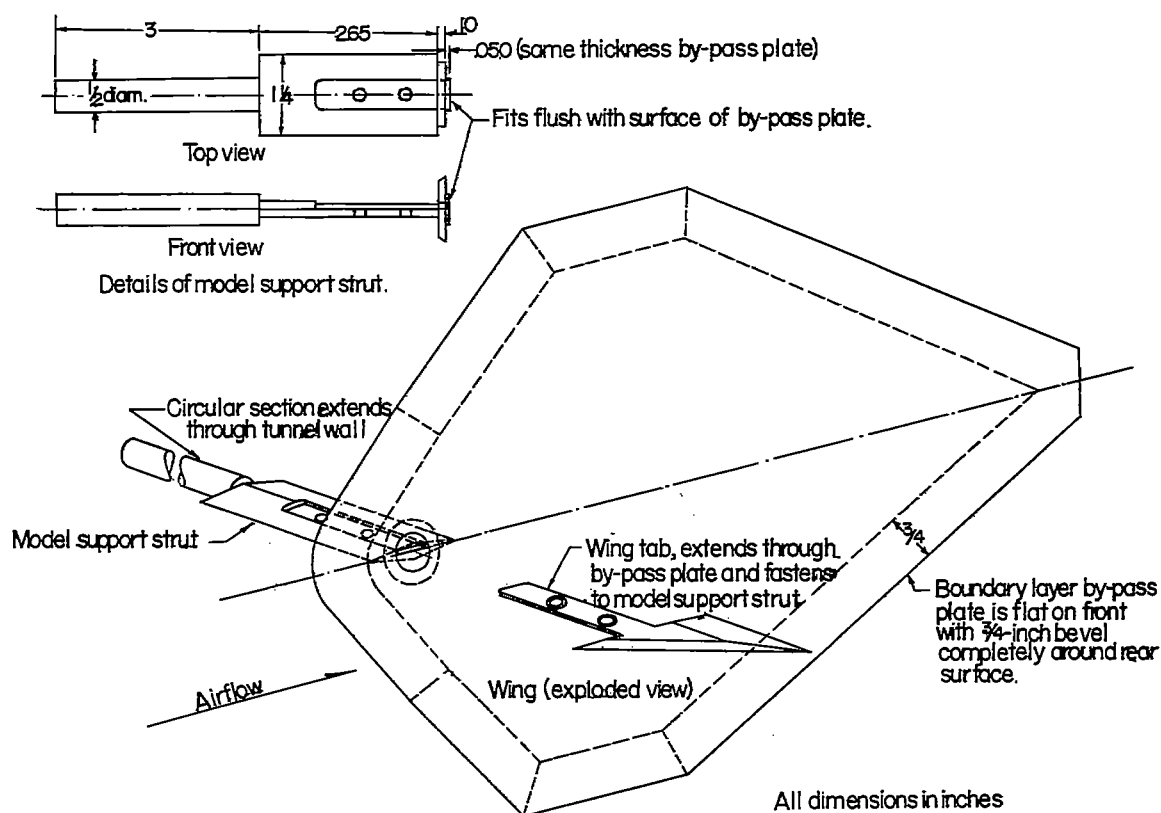
(b) Method of model support.

Figure 1.- Models and model-support apparatus.
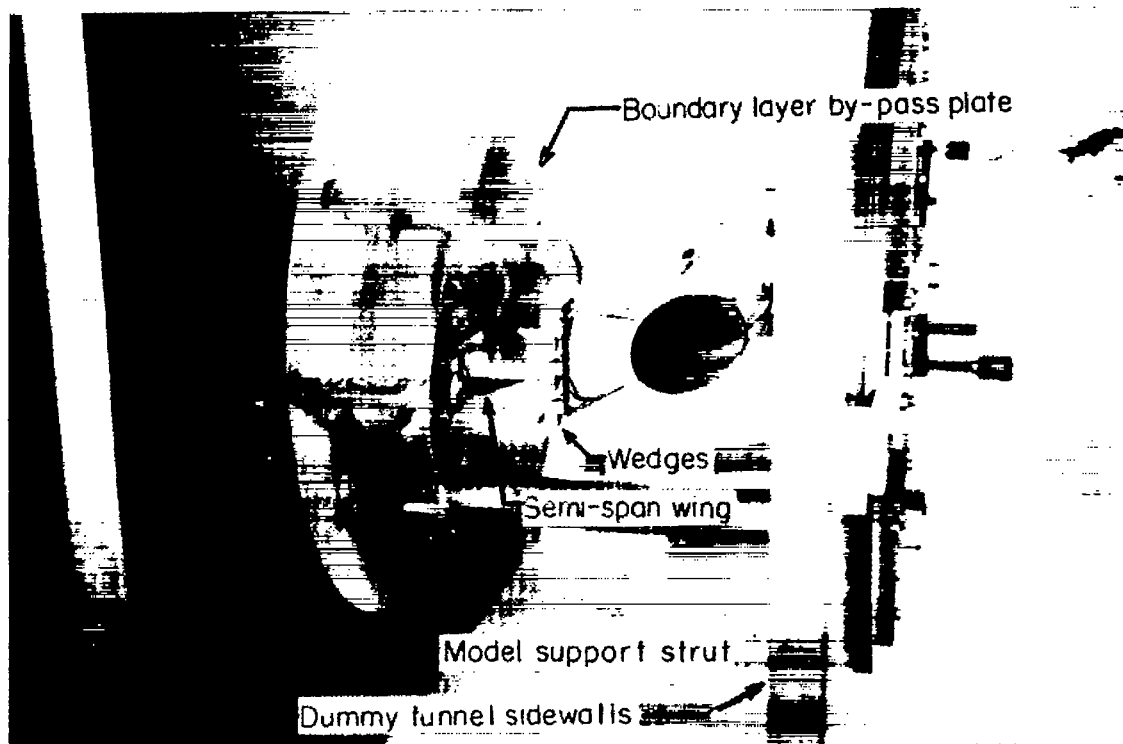
(a) Arrangement of model, bypass plate, and survey apparatus.
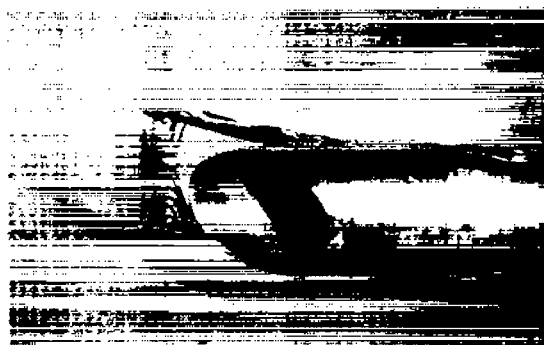
L-82097

(b) Pitot rake.　　　　　(c) Wedge rake.

Figure 2.- Test apparatus.

Build up planform with
Silver Solder

.35

.21

.07

.25

.15
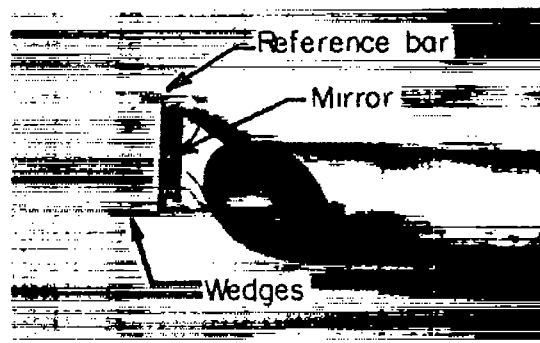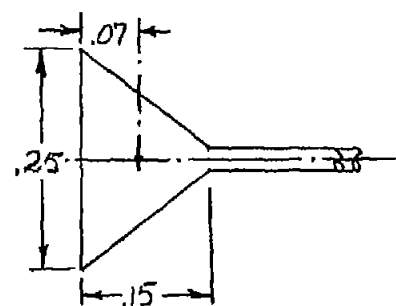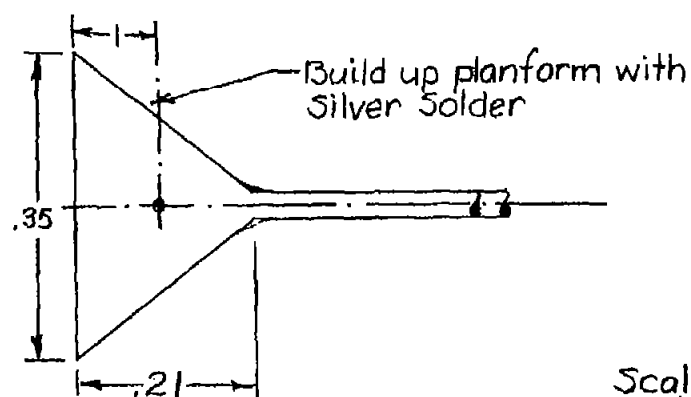
Scale: 5 × Size
(All dimensions in inches)

Two .0135 diam. orifices
(directly opposite)

Two .030 O.D. thin-
wall tubes, soldered
back to back.

Two .010 diam. orifices
(directly opposite)

Two .025 O.D. thin-
wall tubes, soldered
back to back.
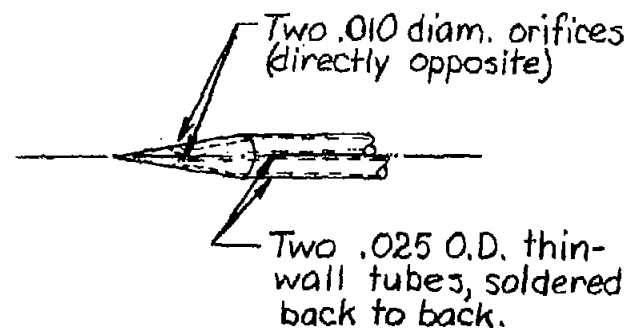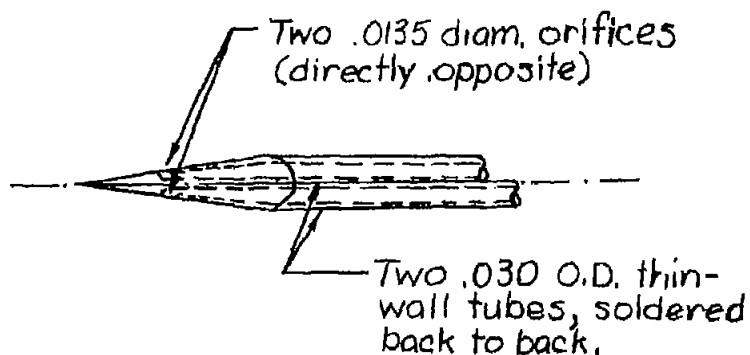
(d) Typical wedge used in tests
at M = 1.62.

(e) Typical wedge used in tests
at M = 2.41.

Figure 2.- Concluded.

Wires indicate free
stream direction.

Planview Sideview

(a) 50° Λ Triangular wing, M = 1.93, α = 12°

Planview Sideview

(b) 63° Λ Triangular wing, M=1.93, α = 12°

Planview Sideview

(c) 72° Λ Triangular wing, M= 1.93, α = 18°

L-82098

Figure 3.- Schlieren photographs illustrating the flow behind various wings.

Planview   Sideview

(d) 50° Λ Triangular wing reversed, M=1.93, $\alpha=12°$

Planview   Sideview

(e) Diamond planform, M = 1.93, $\alpha = 12°$

L-82099

Figure 3.- Concluded.

(a)50°ΛΔwing, α=12°,M=1.93, R=.323×10⁶

(b)63°ΛΔwing, α=12°,M=1.93,R=.485×10⁶

(c)72°ΛΔwing, α=18°, M=1.93, R=.485×10⁶
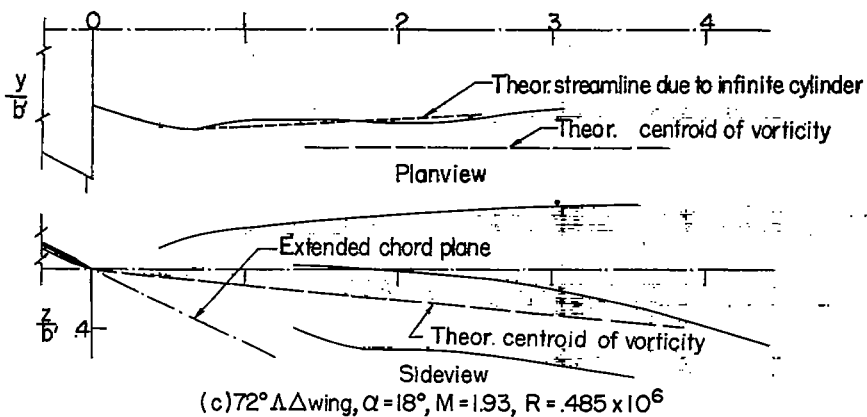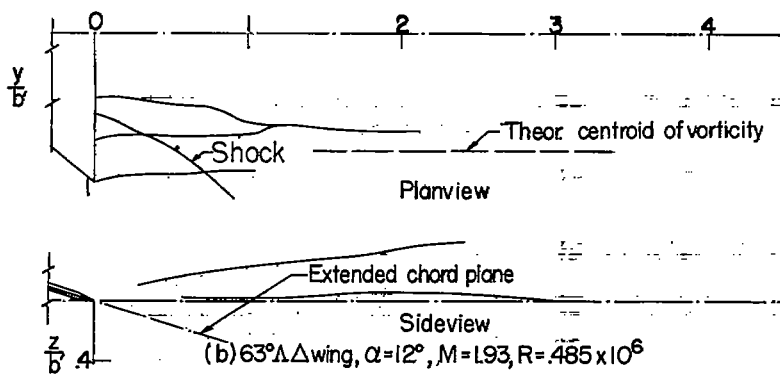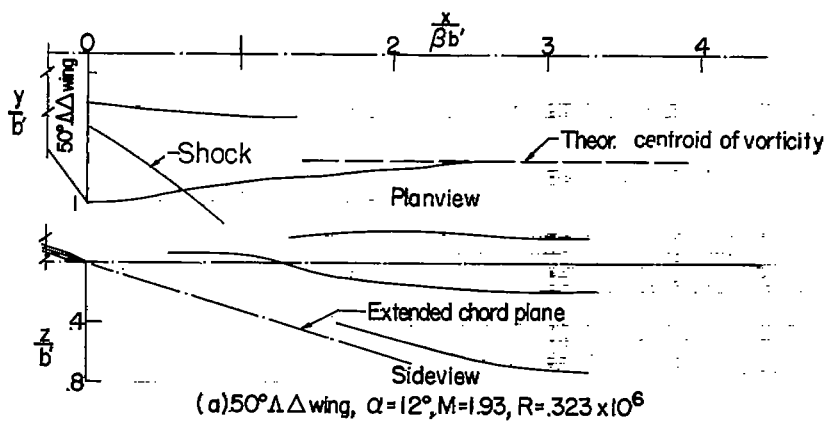
Figure 4.- Sketches illustrating the locations of the paths of high
vorticity behind triangular wings.
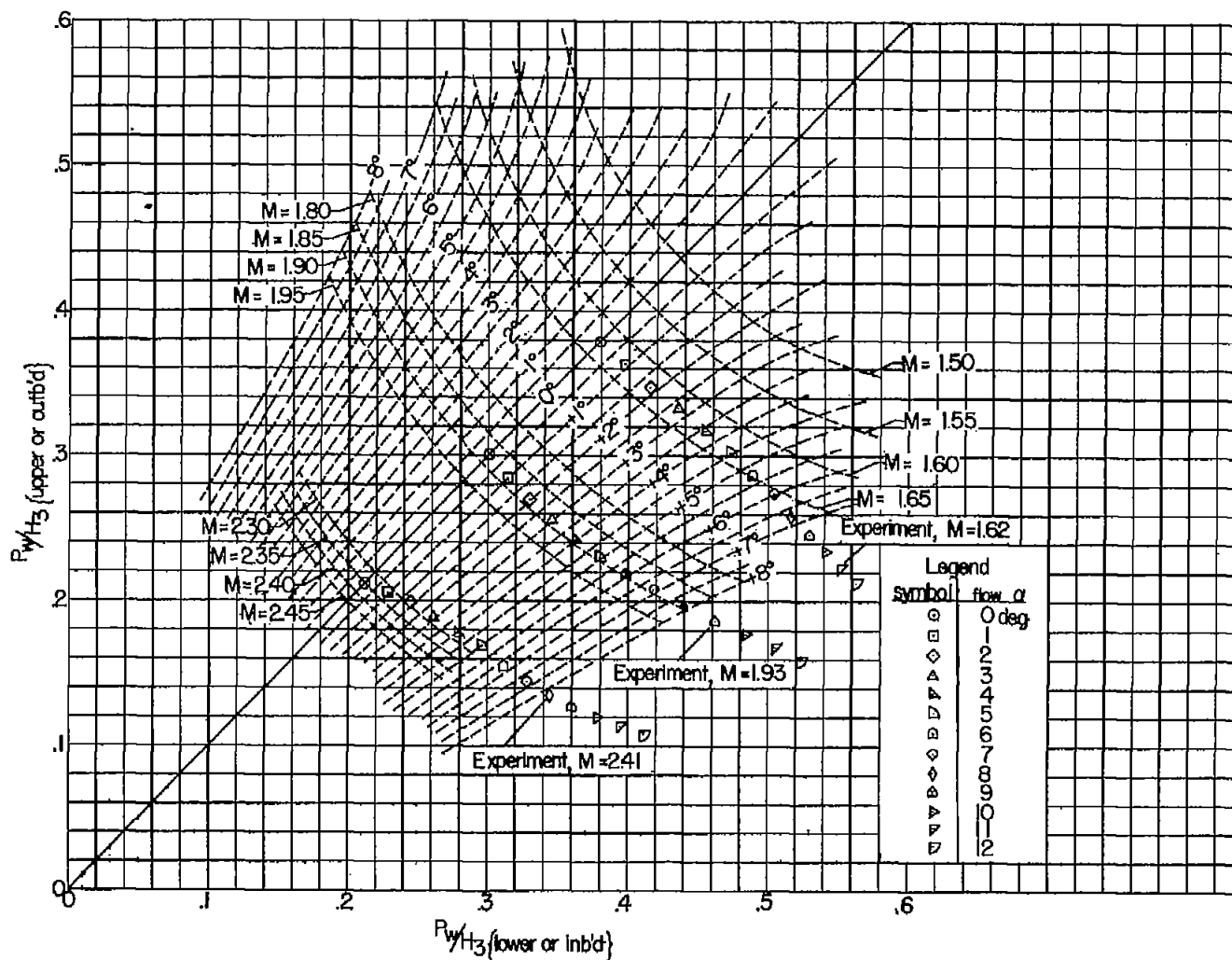
Figure 5.- Chart illustrating wedge pressure readings as a function of angle
of flow with respect to wedge and the local Mach number (8° half-angle
wedge).

Dashed lines correspond to constant values of $\frac{H_3}{H_{o_3}}$, as quoted.

$\frac{H_3}{H_{o_3}}$ (Free stream) = .536
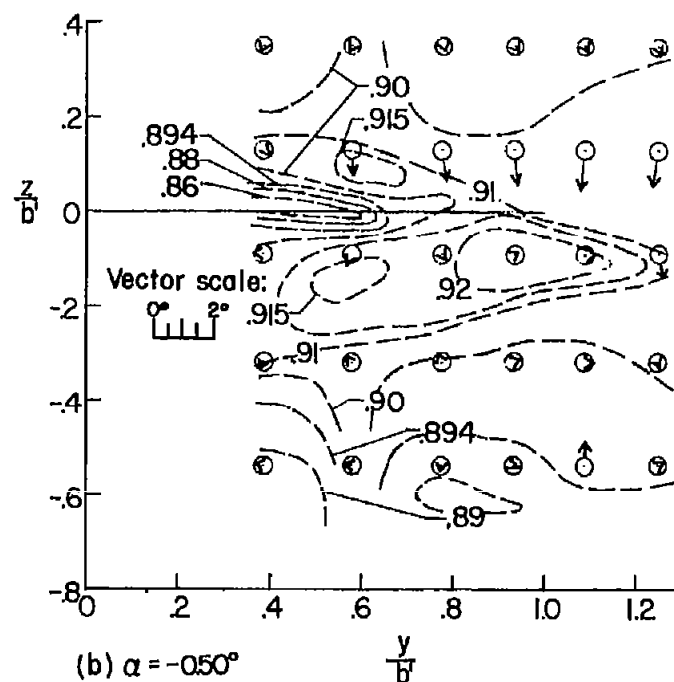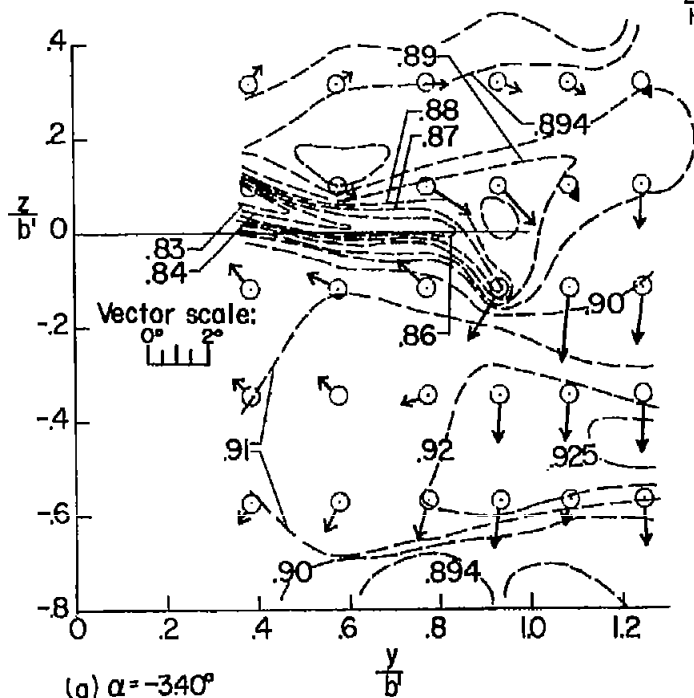

(a) $\alpha = -3.50°$

(b) $\alpha = -0.50°$
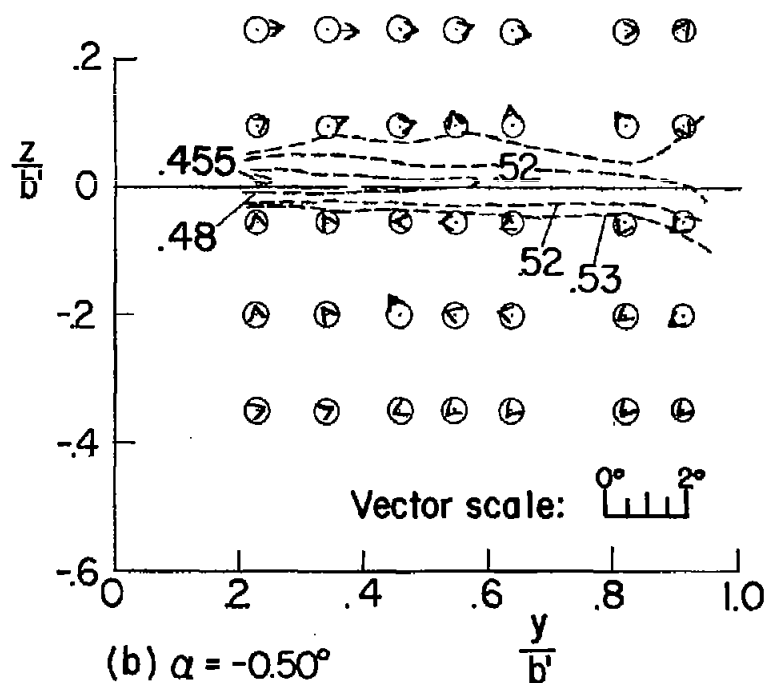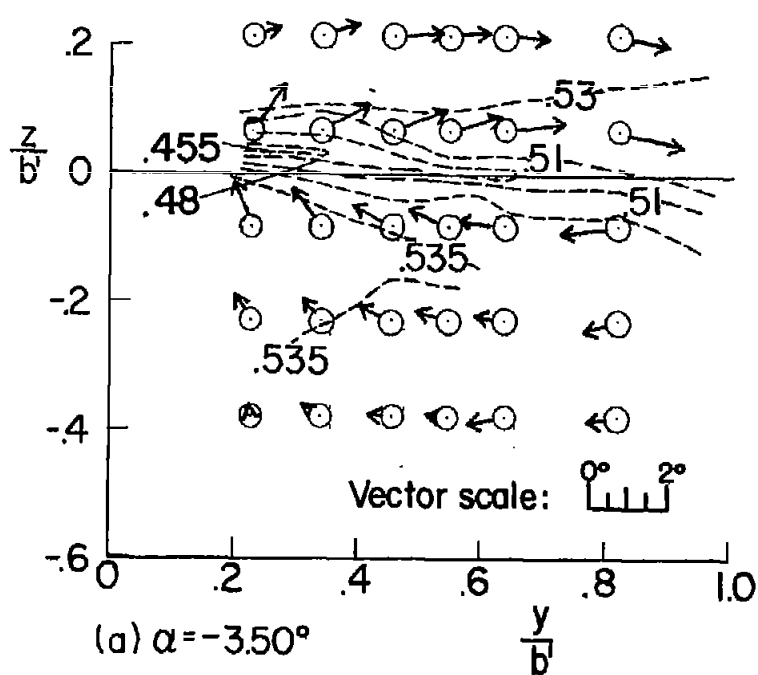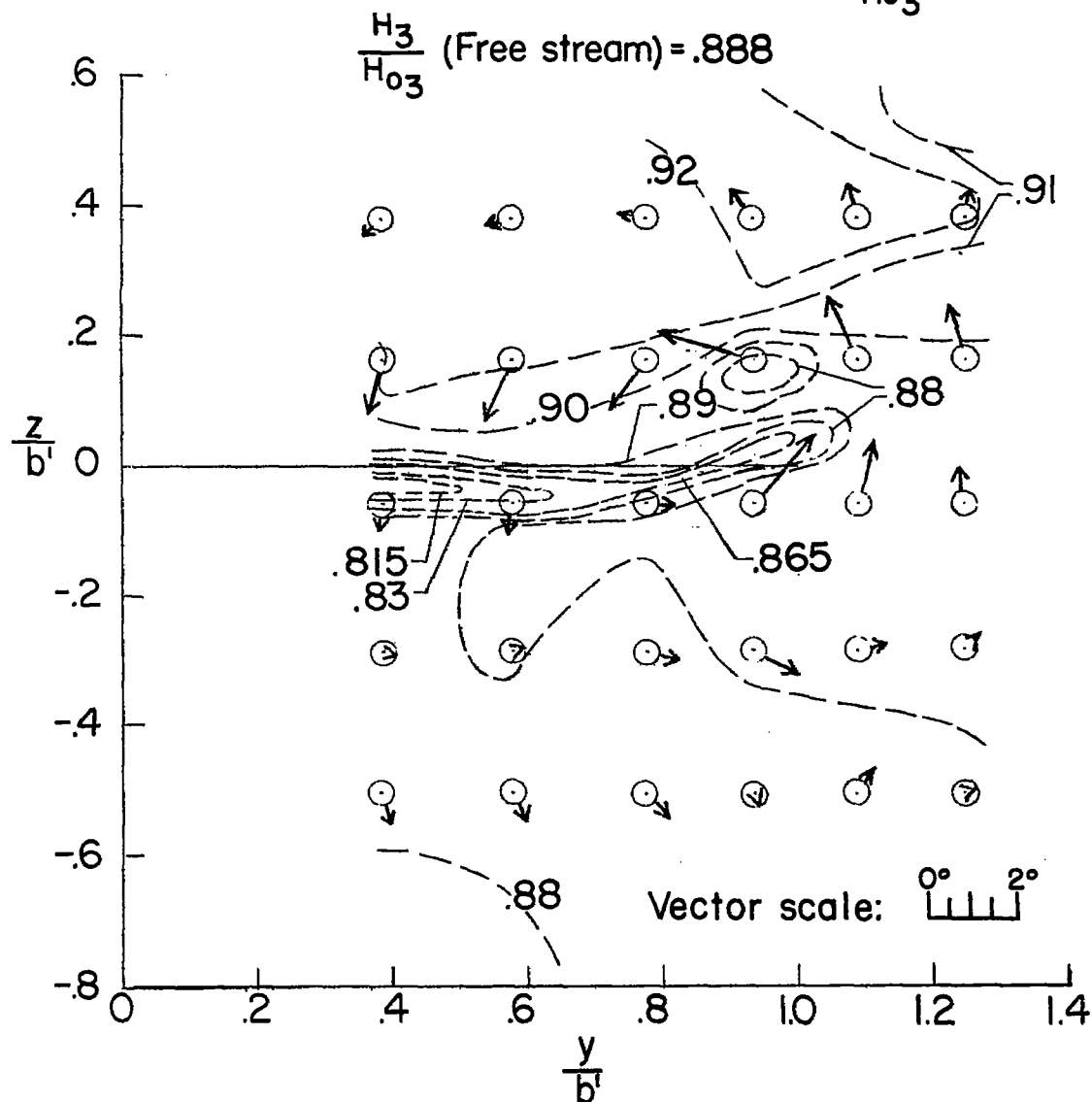
Figure 6.- Pressure contours and vector representation of the flow behind a triangular wing. $\Lambda = 50°$; $M = 2.41$; $x = 1.5c_r$; $R = 1.42 \times 10^6$.

Dashed lines correspond to constant values of $\frac{H_3}{H_{o_3}}$, as quoted.

$\frac{H_3}{H_{o_3}}$ (Free stream) = .536

(c) $\alpha = 2.50°$

(d) $\alpha = 8.50°$
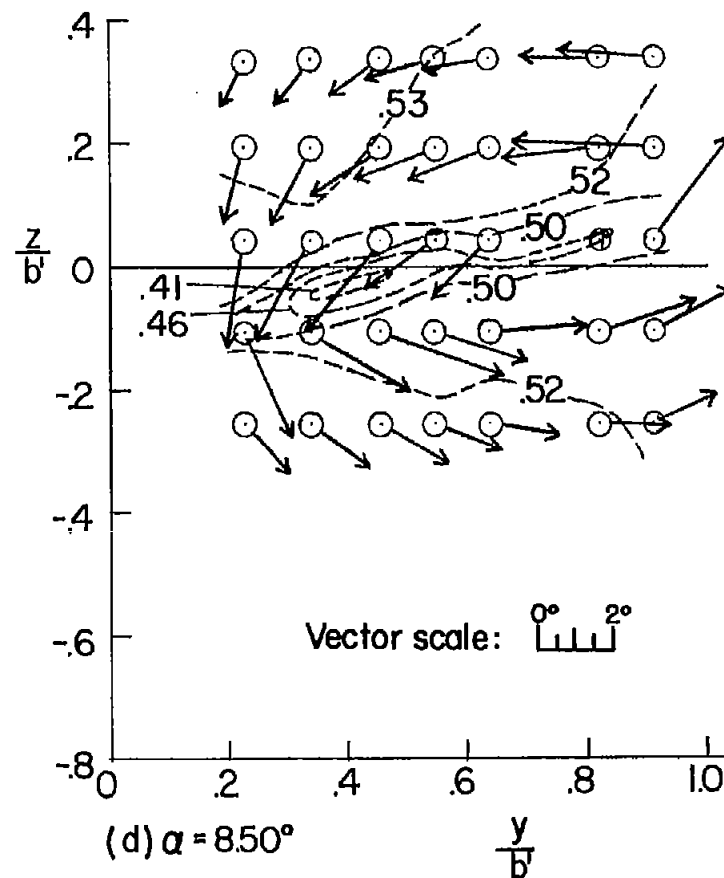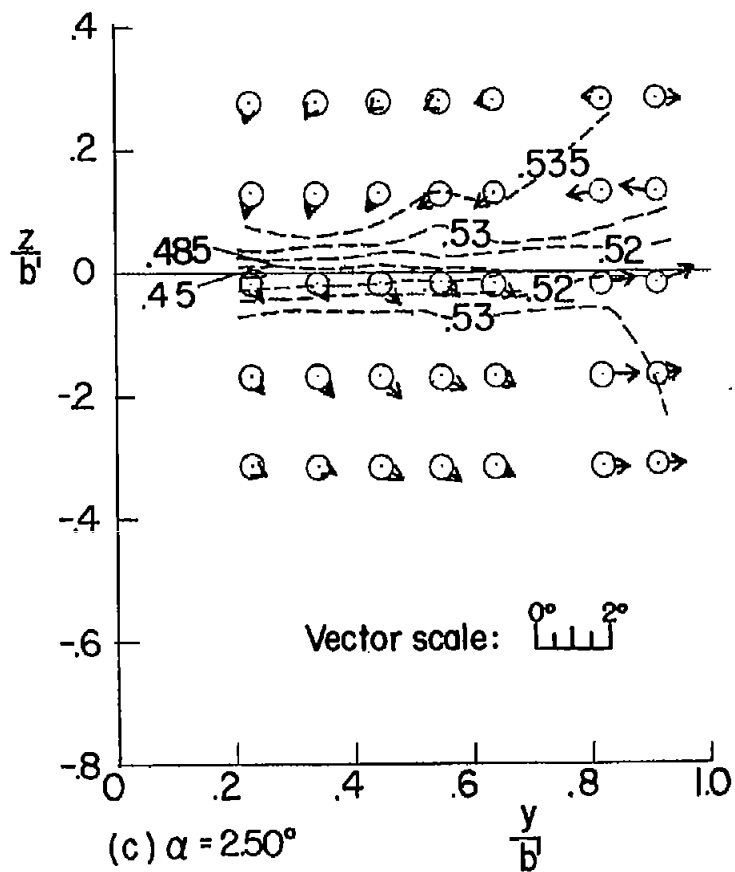
Figure 6.- Continued.

Dashed lines correspond to constant values of $\frac{H_3}{H_{o_3}}$, as quoted.

(e) $\alpha = 11.50°$
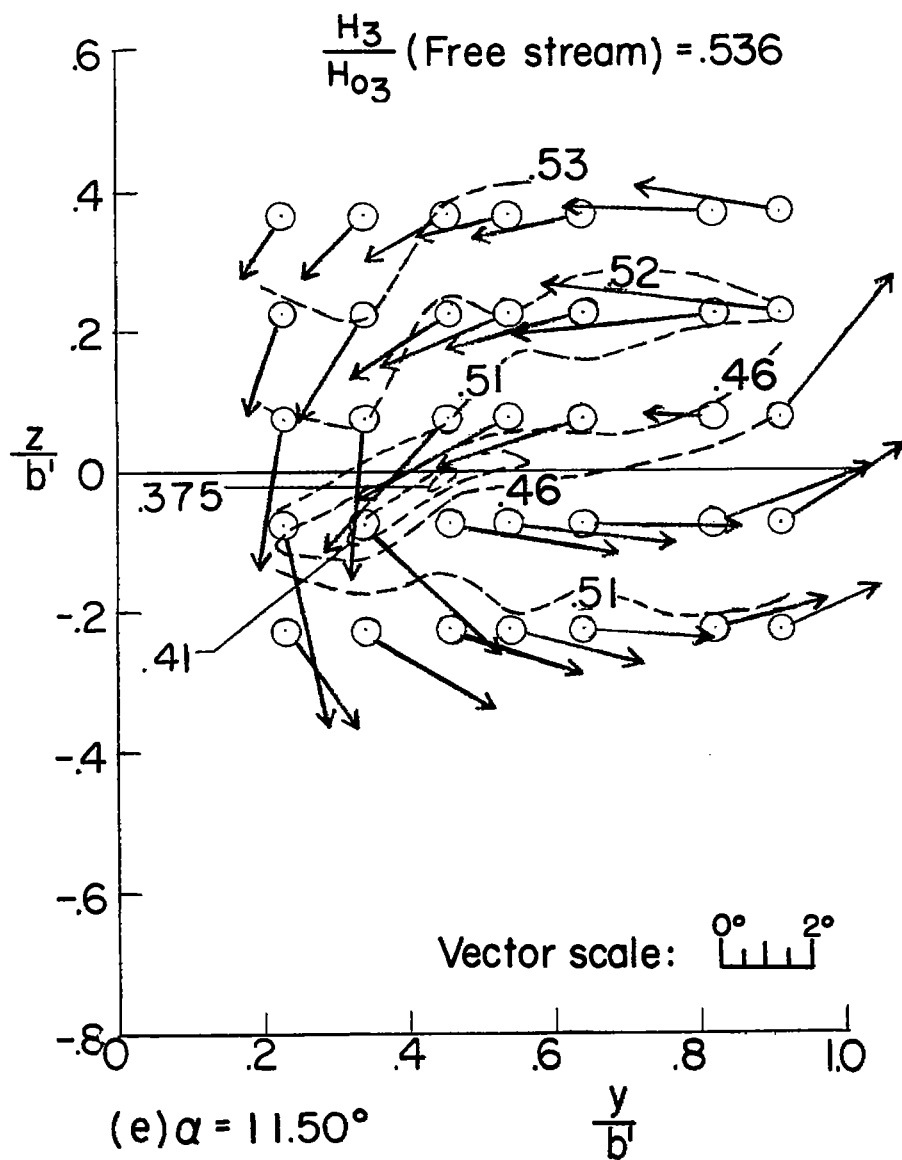
Figure 6.- Concluded.
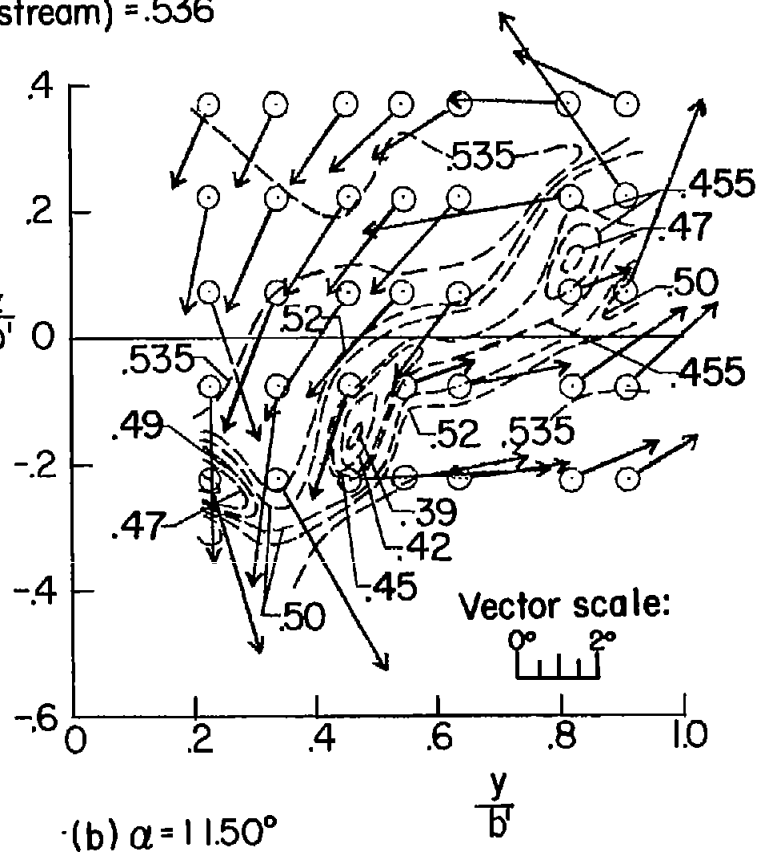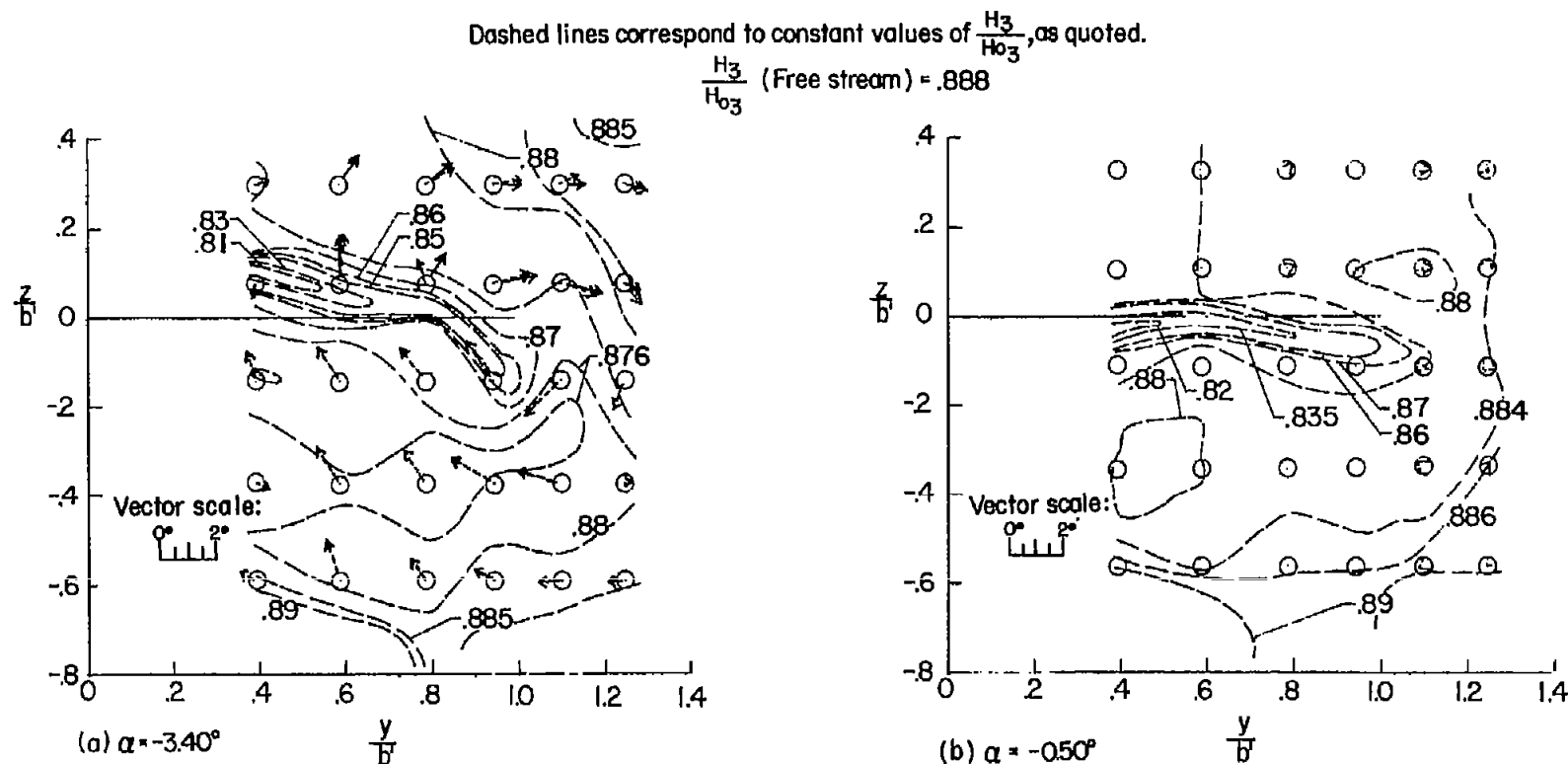
Figure 7.- Pressure contours and vector representation of the flow behind a triangular wing. $\Lambda = 50°$; $M = 2.41$; $x = 3c_r$; $R = 1.42 \times 10^6$.

Dashed lines correspond to constant values of $\dfrac{H_3}{H_{o_3}}$, as quoted.

$$\dfrac{H_3}{H_{o_3}}\text{(Free stream)} = .536$$

(a) $\alpha = -3.50°$

(b) $\alpha = -0.50°$
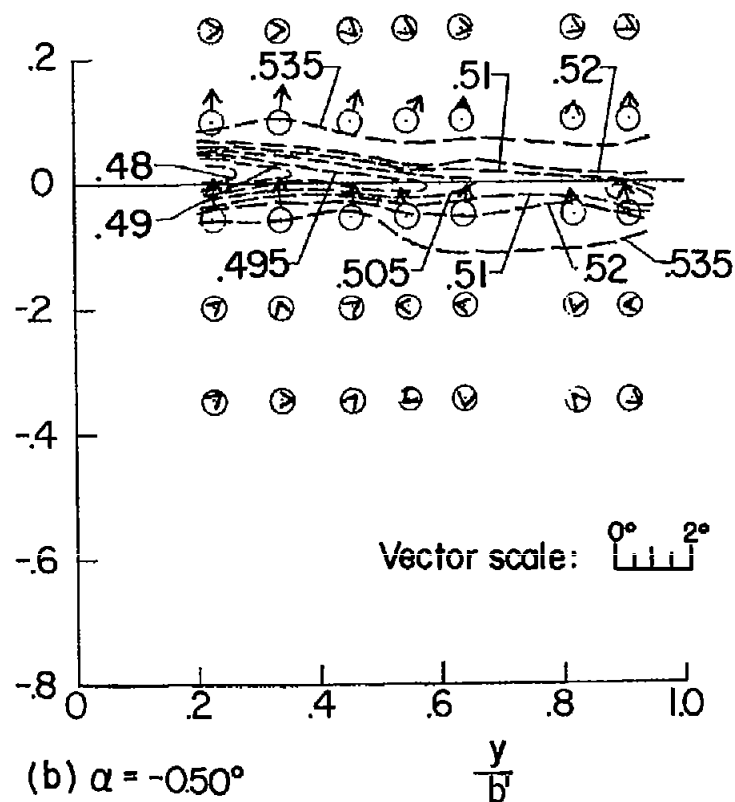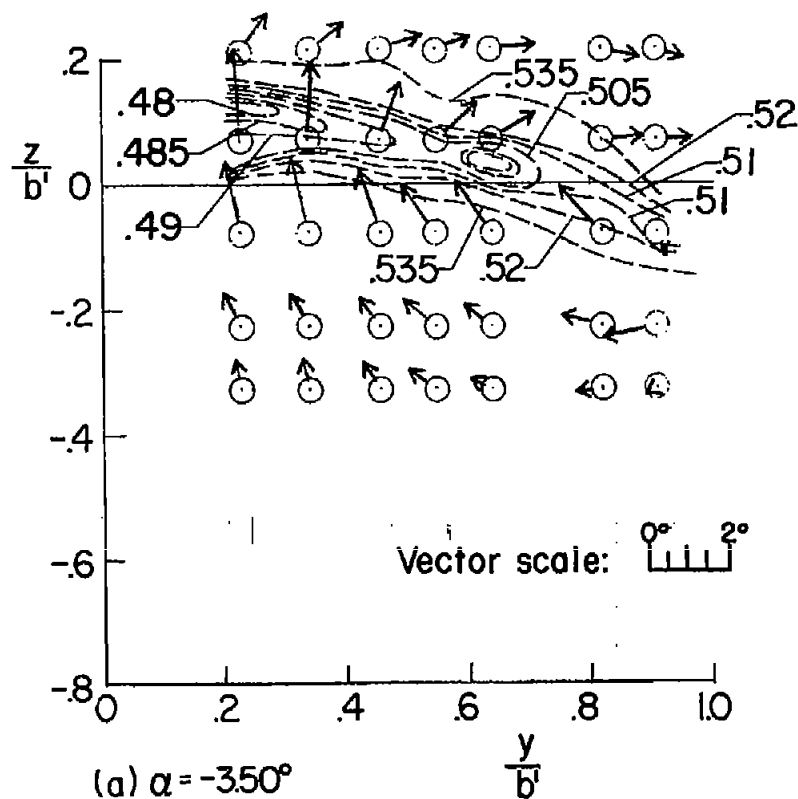
Figure 8.- Pressure contours and vector representation of the flow behind a triangular wing. $\Lambda = 50°$; $M = 2.41$; $x = 4c_r$; $R = 1.42 \times 10^6$.

Dashed lines correspond to constant values of $\frac{H_3}{H_{o_3}}$, as quoted.

$\frac{H_3}{H_{o_3}}$ (Free stream) = .536

(c) $\alpha = 2.50°$

(d) $\alpha = 8.50°$
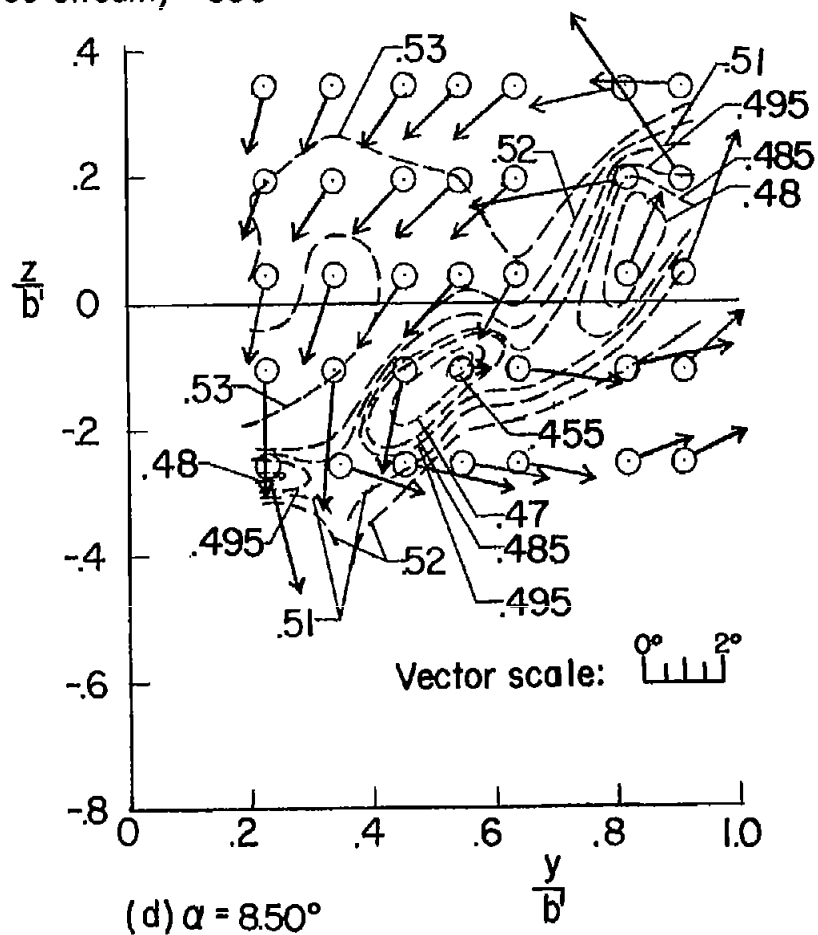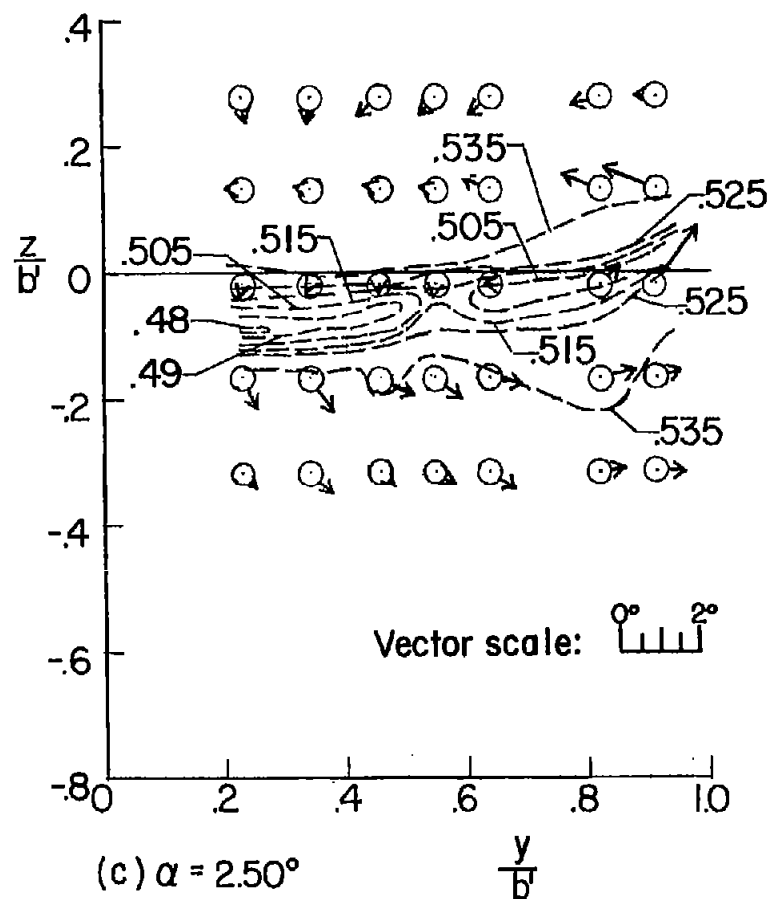
Figure 8.- Continued.

Dashed lines correspond to constant values of $\dfrac{H_3}{H_{o_3}}$, as quoted.
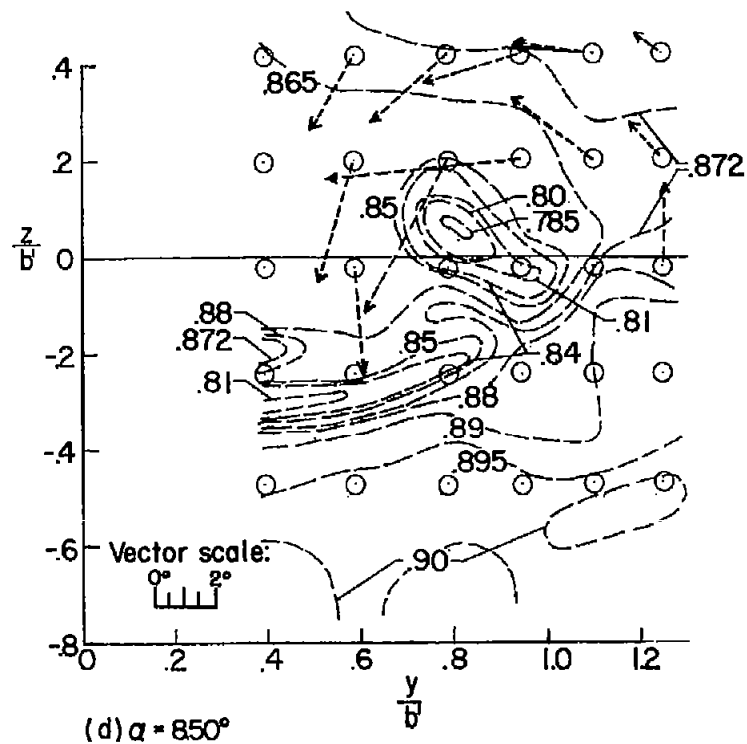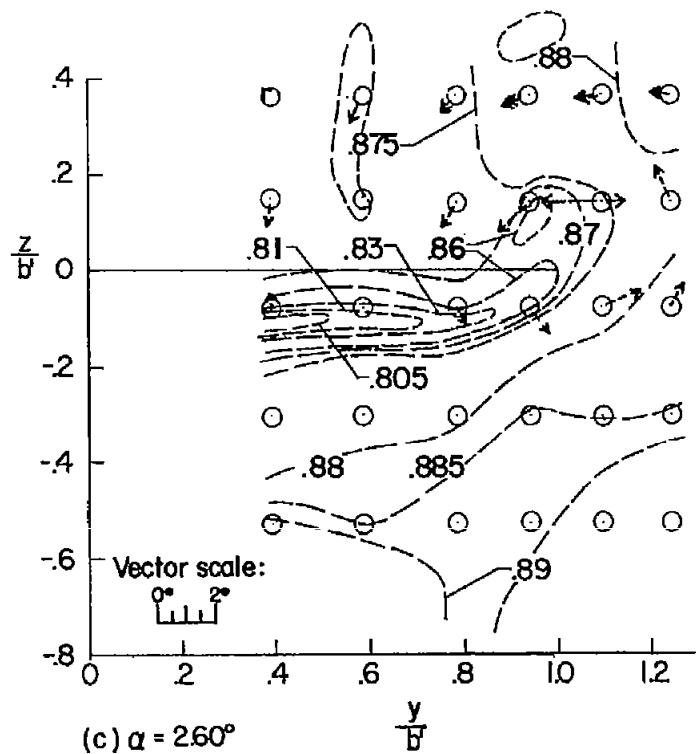

(e) $\alpha = 11.50°$
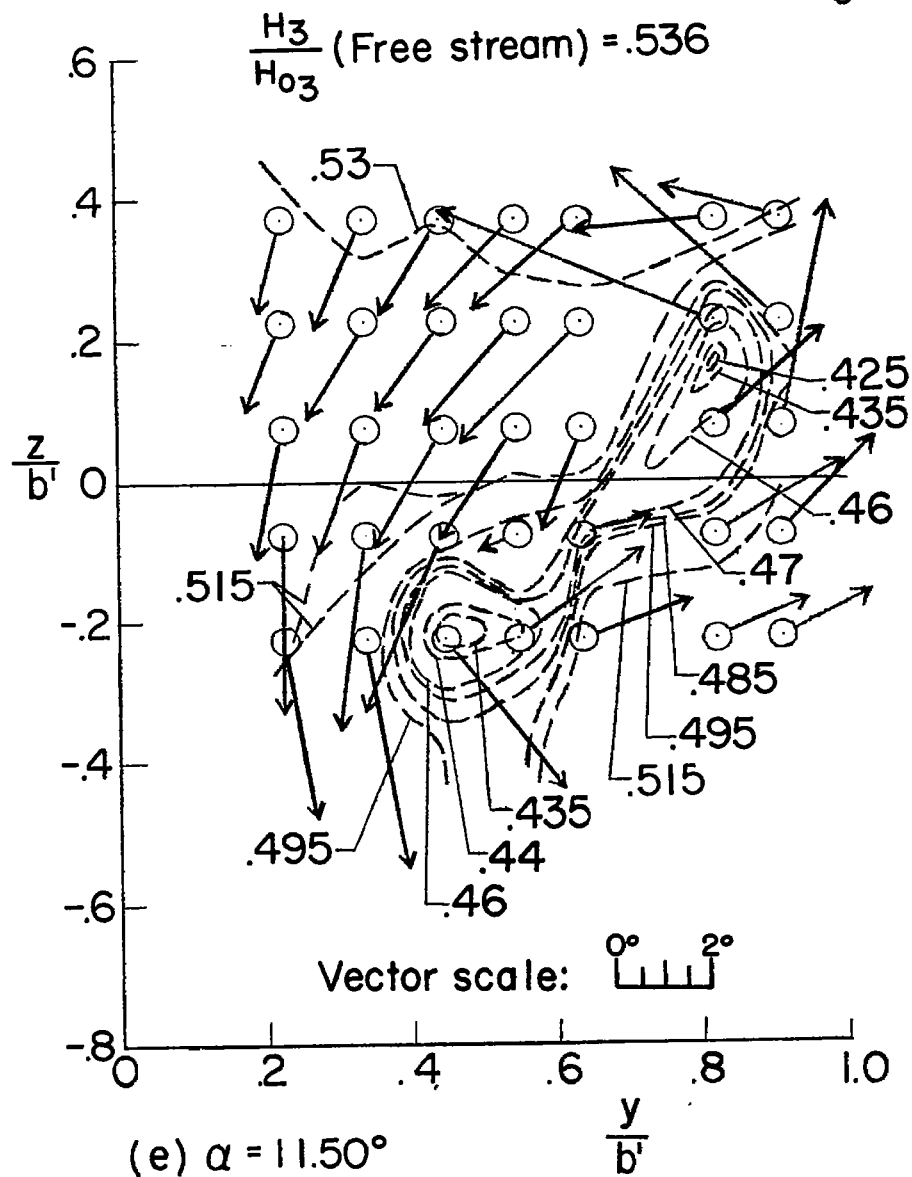
Figure 8.- Concluded.

Dashed lines correspond to constant values of $\frac{H_3}{H_{o3}}$, as quoted.
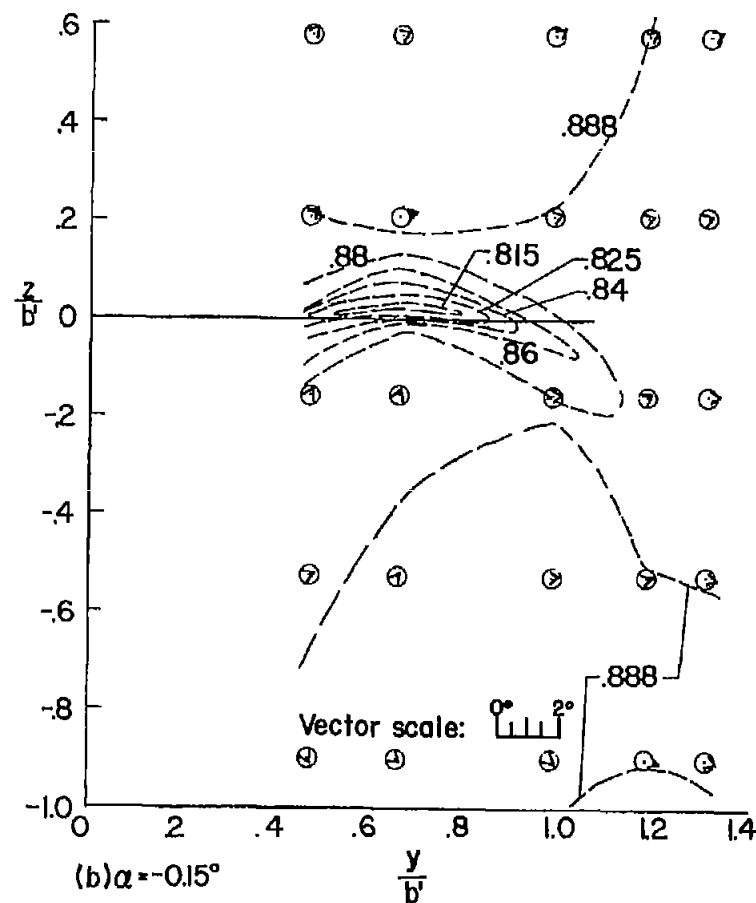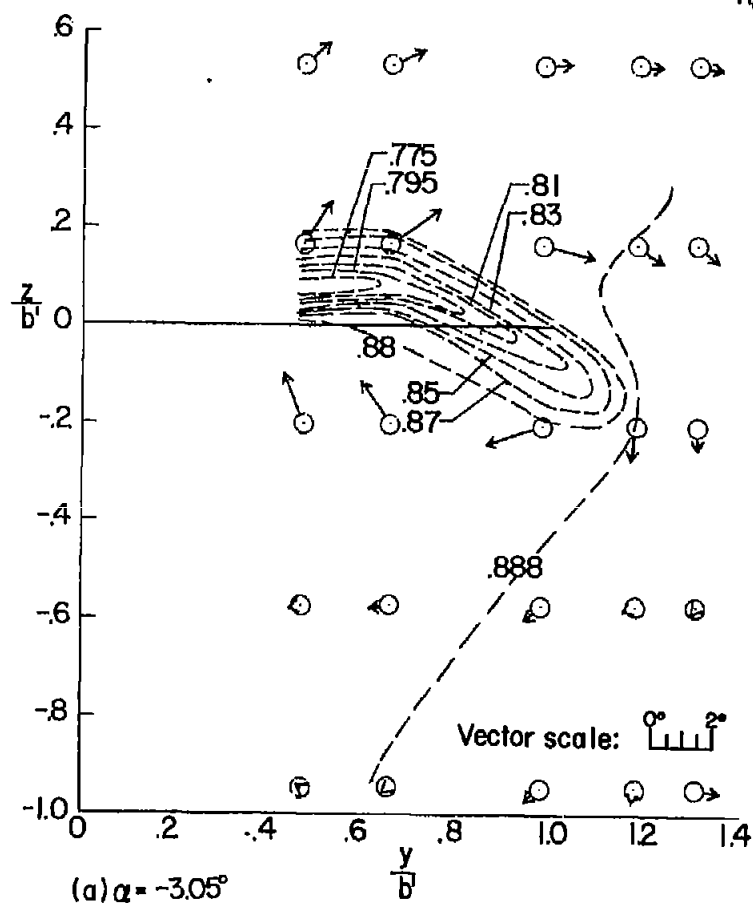
$$\frac{H_3}{H_{o3}}\text{ (Free stream)} = .536$$

(a) $\alpha = -3.00°$

(b) $\alpha = -0.10°$
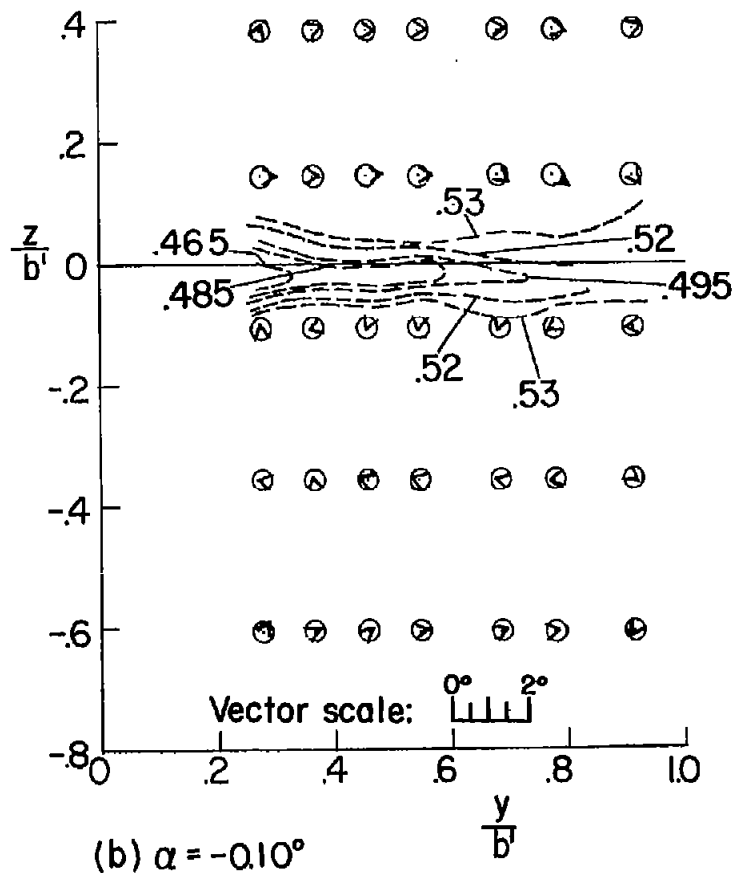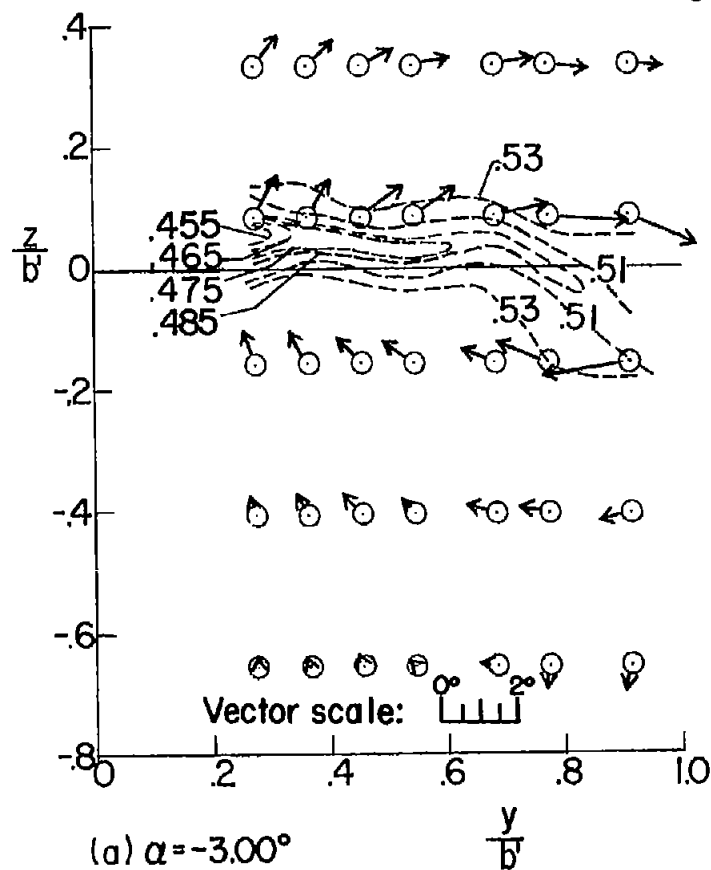
Figure 9.- Pressure contours and vector representation of the flow behind a triangular wing. $\Lambda = 63°$; $M = 2.41$; $x = 1.5c_r$; $R = 1.42 \times 10^6$.

Dashed lines correspond to constant values of $\dfrac{H_3}{H_{o_3}}$, as quoted.
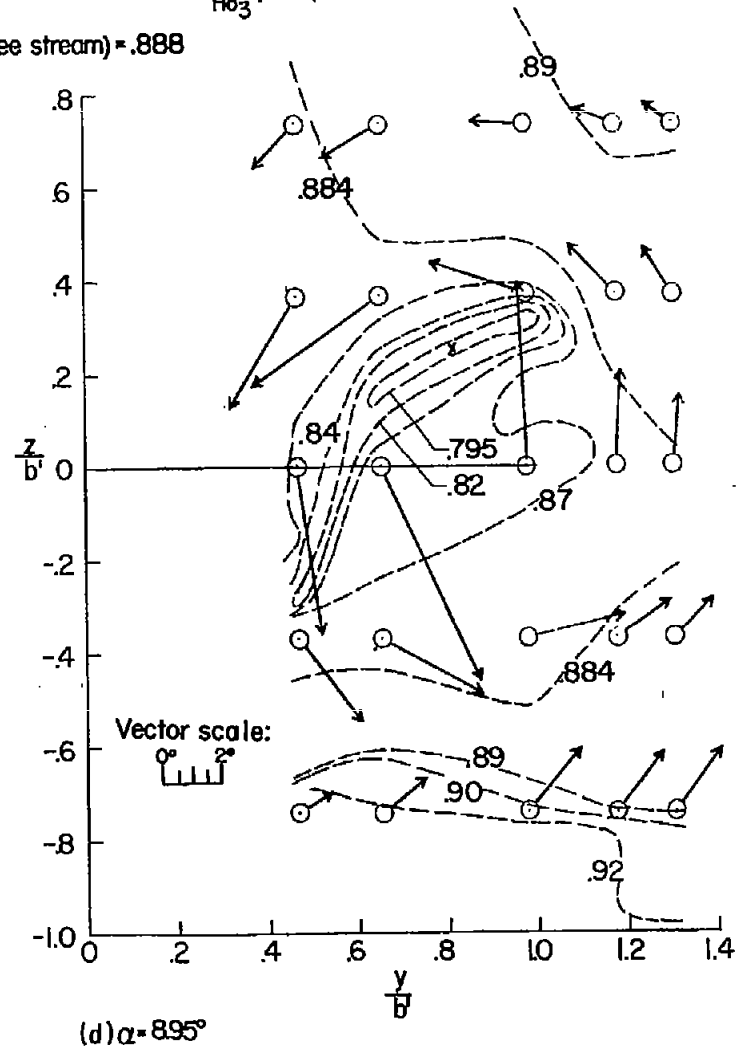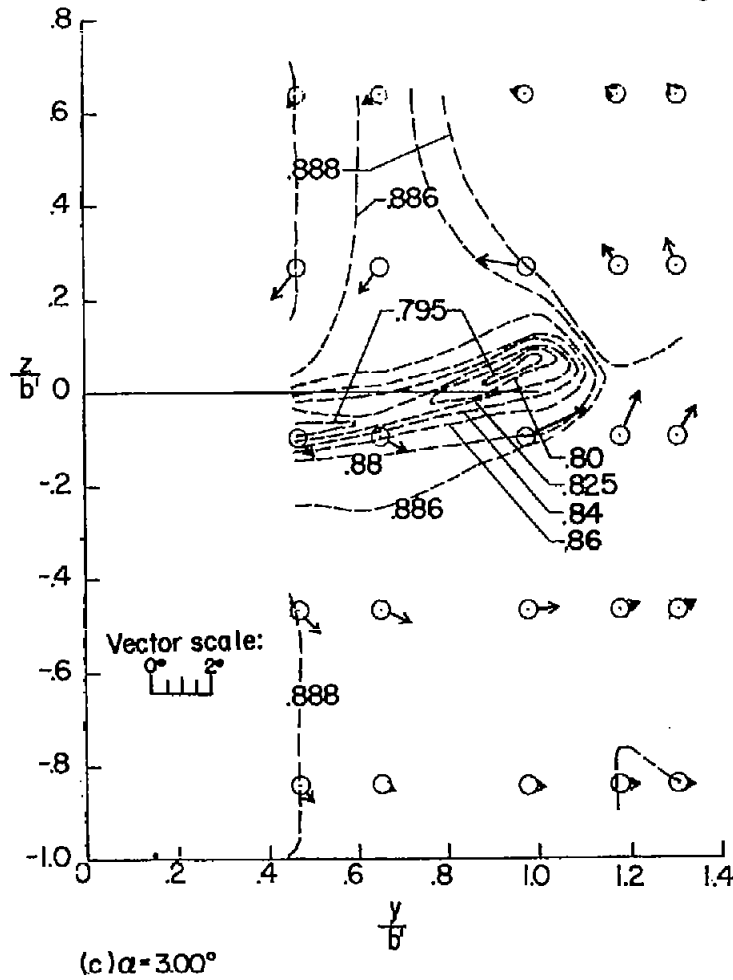
$\dfrac{H_3}{H_{o_3}}$ (Free stream) = .536
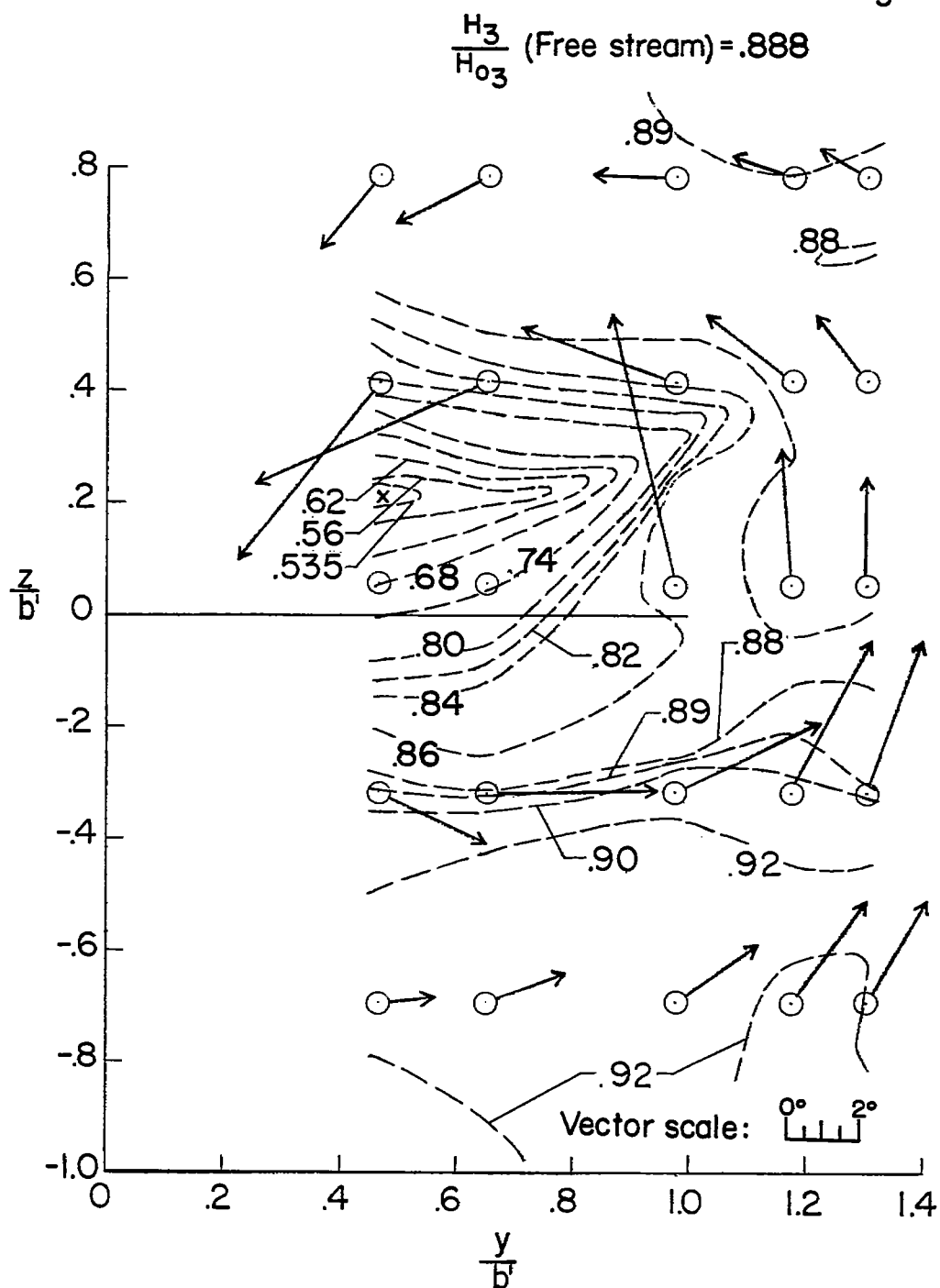

(c) $\alpha = 3.00°$

(d) $\alpha = 11.95°$
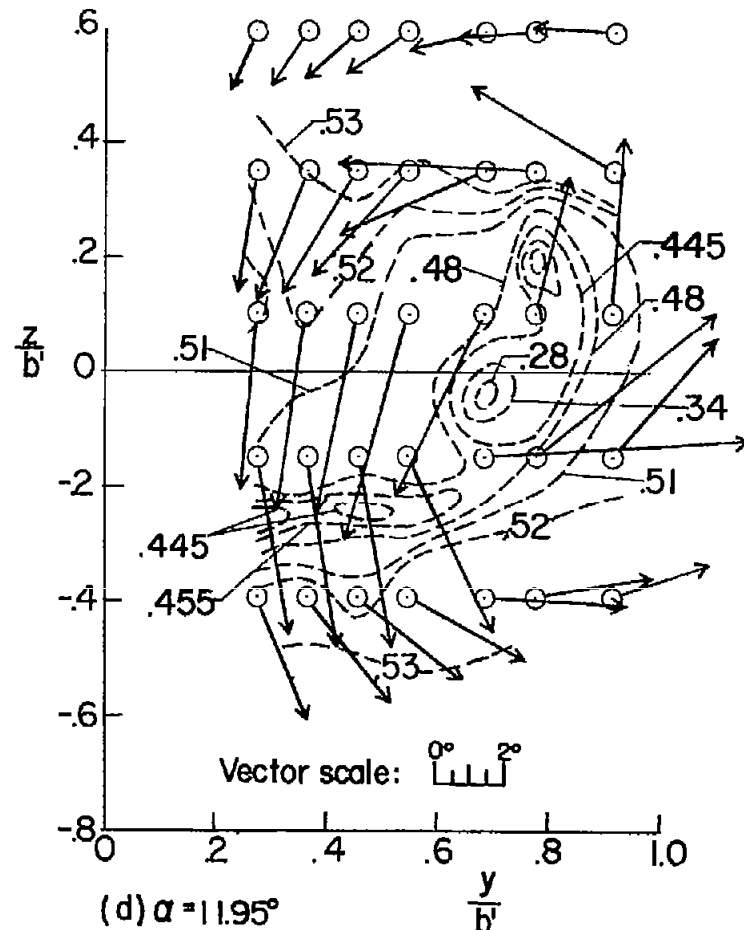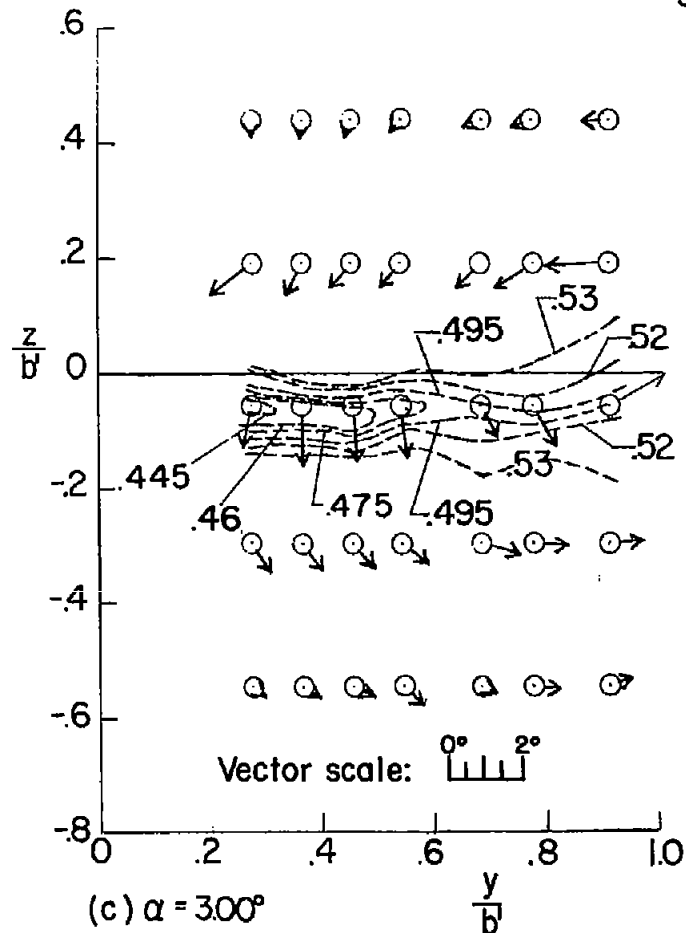
Figure 9.- Continued.

Dashed lines correspond to constant values of $\frac{H_3}{H_{o_3}}$, as quoted.

(e) $\alpha = 13.95°$

Figure 9.- Concluded.

Dashed lines correspond to constant values of $\frac{H_3}{H_{o_3}}$, as quoted.

$\frac{H_3}{H_{o_3}}$ (Free stream) = .536

(a) $\alpha = 11.95°$

(b) $\alpha = 13.95°$

Vector scale:
0° 2°
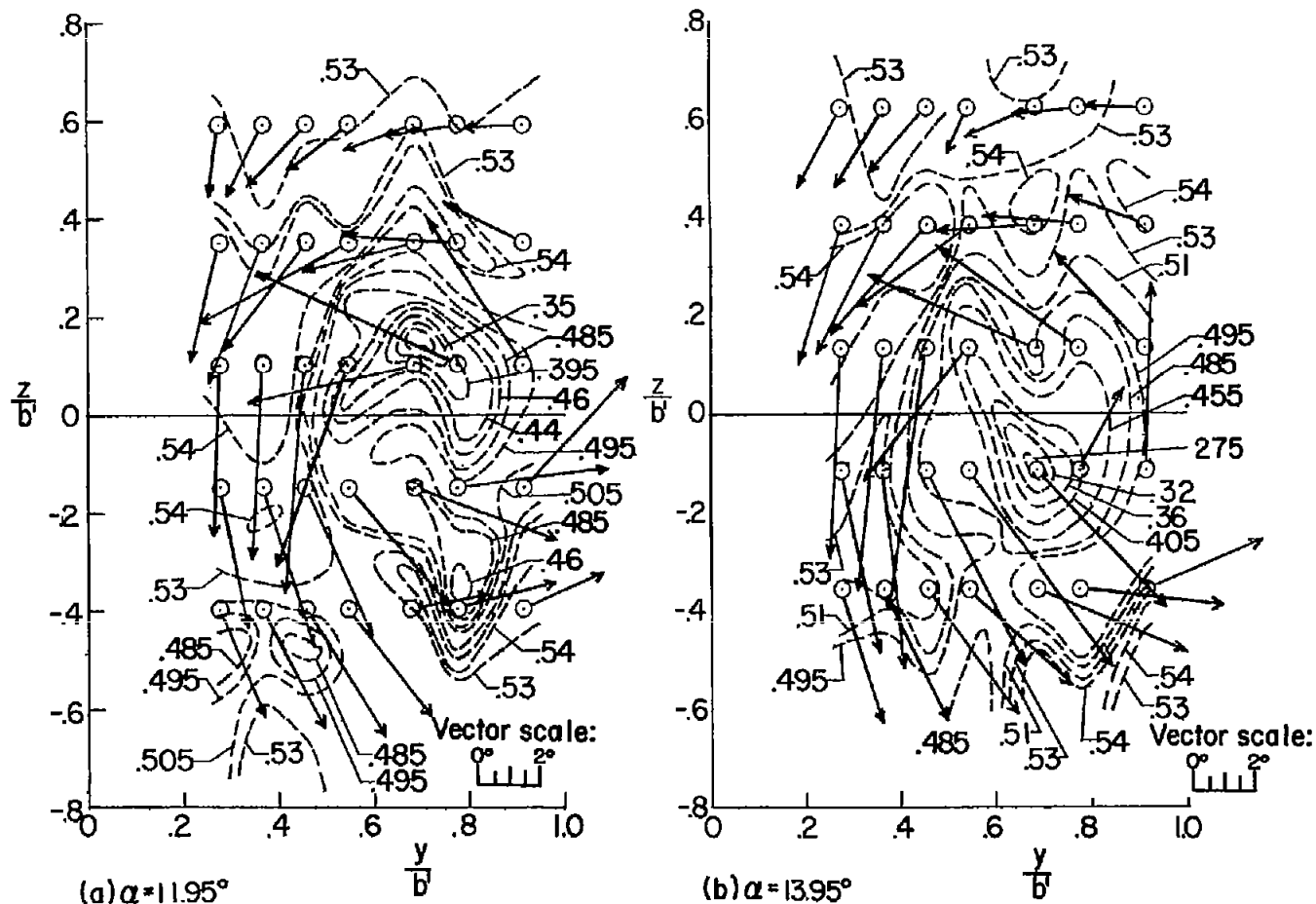
Figure 10.- Pressure contours and vector representation of the flow behind a triangular wing. $\Lambda = 63°$; $M = 2.41$; $x = 3c_r$; $R = 1.42 \times 10^6$.

Dashed lines correspond to constant values of $\frac{H_3}{H_{o_3}}$, as quoted.

$$\frac{H_3}{H_{o_3}} \text{ (Free stream)} = .536$$
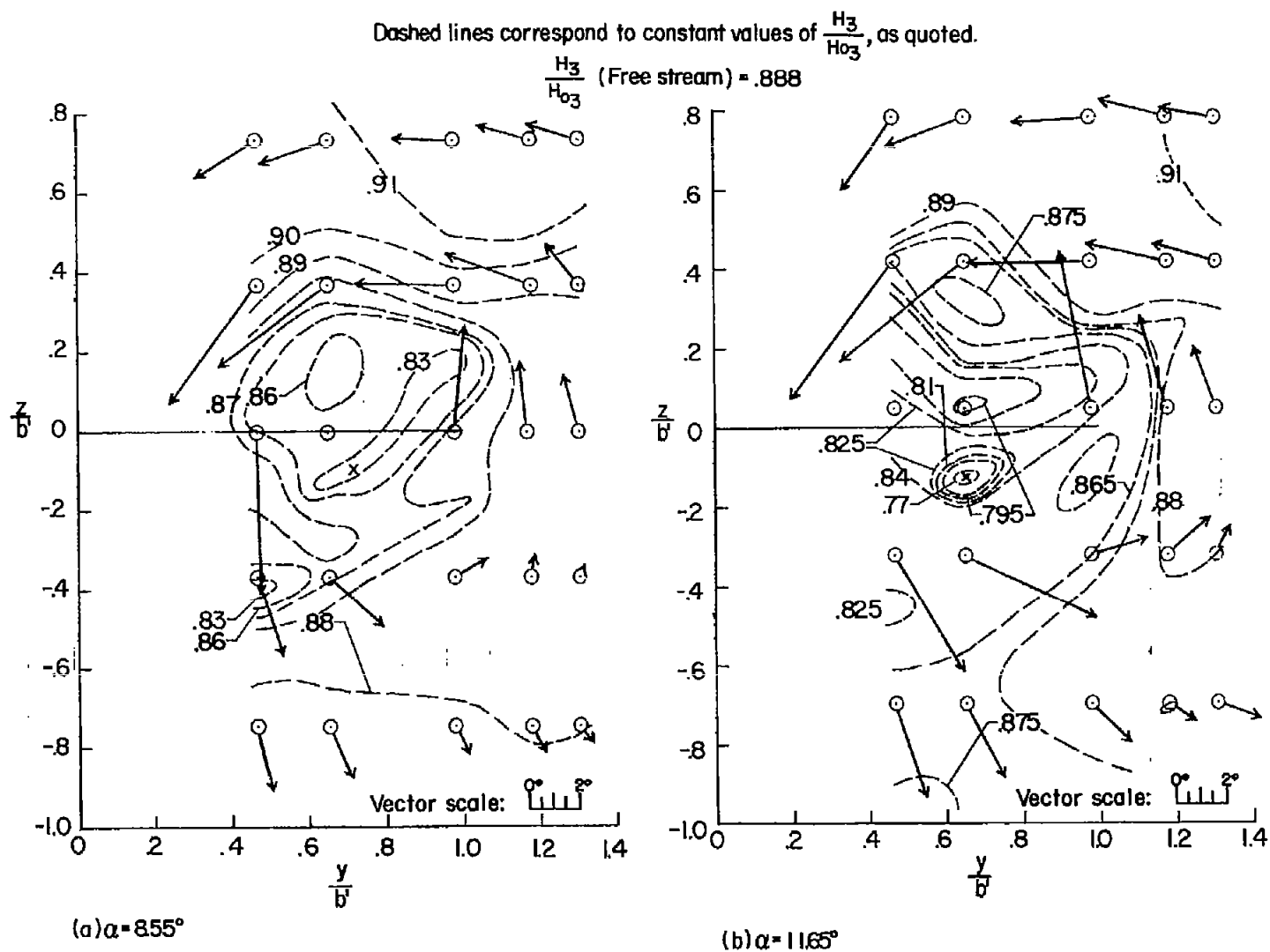

(a) $\alpha = -3.00°$

(b) $\alpha = -0.10°$
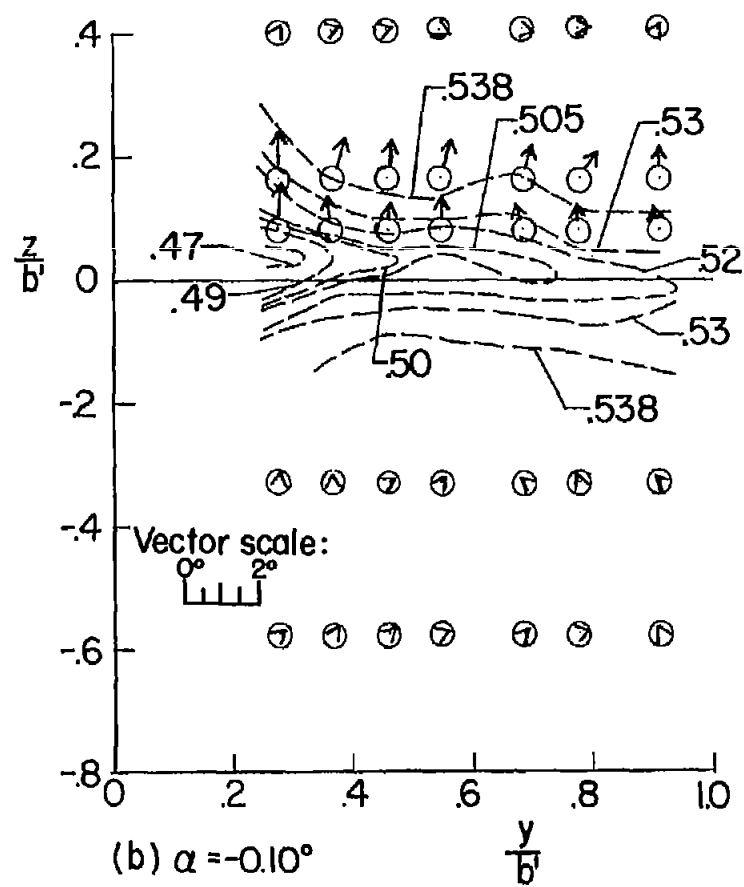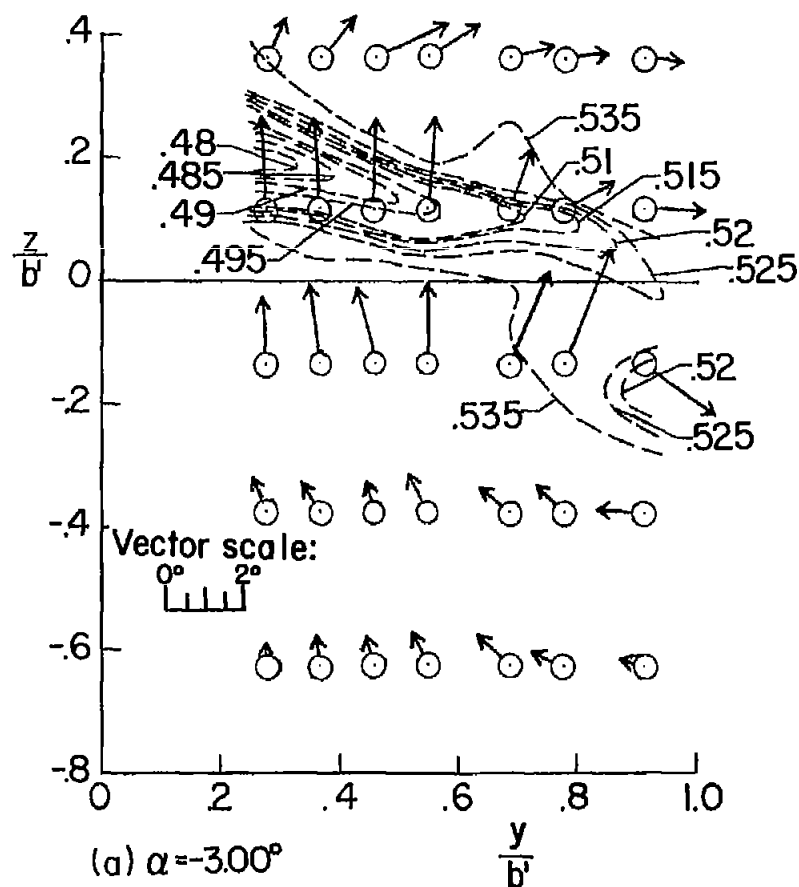
Figure 11.- Pressure contours and vector representation of the flow behind a triangular wing. $\Lambda = 63°$; $M = 2.41$; $x = 4c_r$; $R = 1.42 \times 10^6$.

Dashed lines correspond to constant values of $\frac{H_3}{H_{o_3}}$, as quoted.

$\frac{H_3}{H_{o_3}}$ (Free stream) = .536

.6

.4

$\frac{z}{b'}$

.2

0

-.2

-.4

-.6

-.8

.52

.48

.535

.50

.47

.52

.48

.47

.50

.51

.485

.49

.535

Vector scale: 0° 2°

0 .2 .4 .6 .8 1.0

(c) $\alpha = 3.00°$

$\frac{y}{b'}$

.535

.53

.45

.42

.345

.52

.355

.38

.48

.495

.50

.51

.52

.495

.50

.51

.51

.48

.50

.495

.52

.50

Vector scale: 0° 2°

$\frac{z}{b'}$

.6

.4

.2

0

-.2

-.4

-.6

-.8
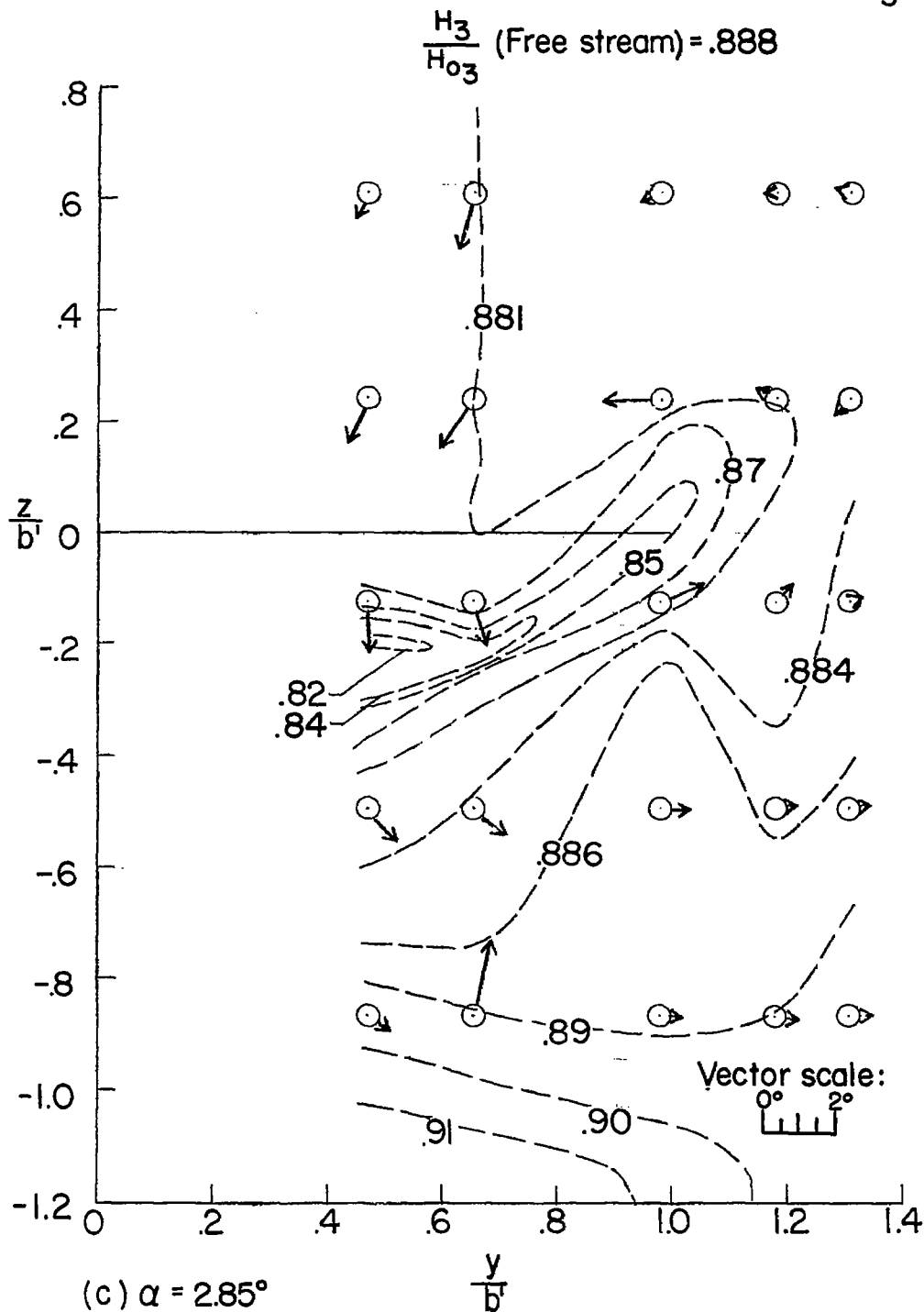
0 .2 .4 .6 .8 1.0

(d) $\alpha = 11.95°$

$\frac{y}{b'}$
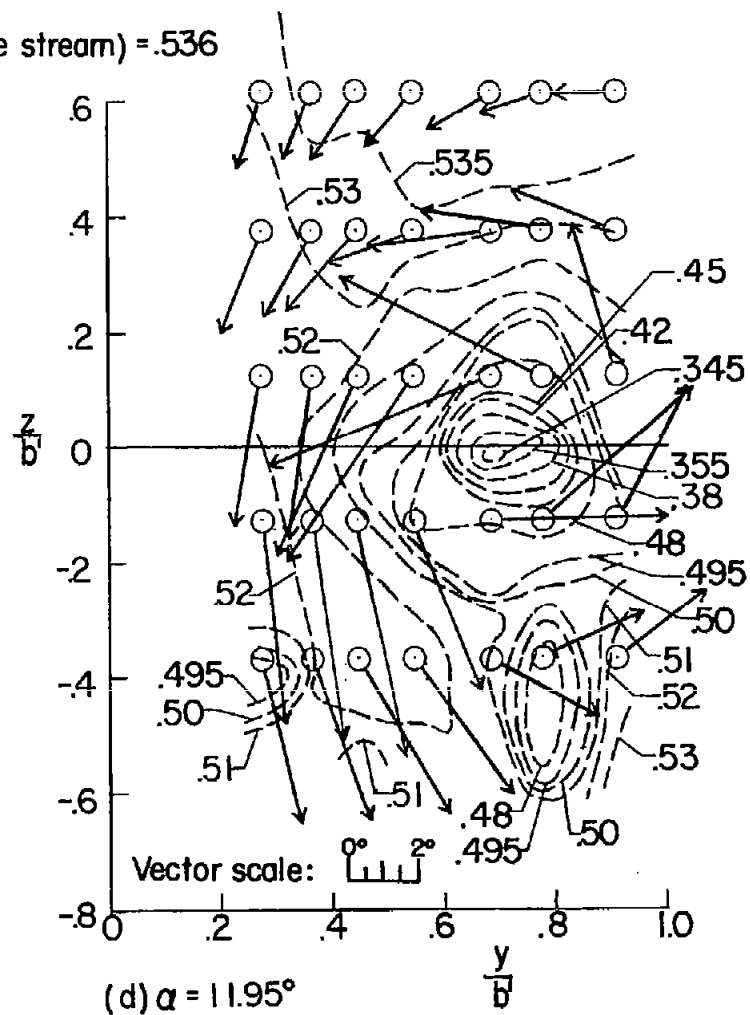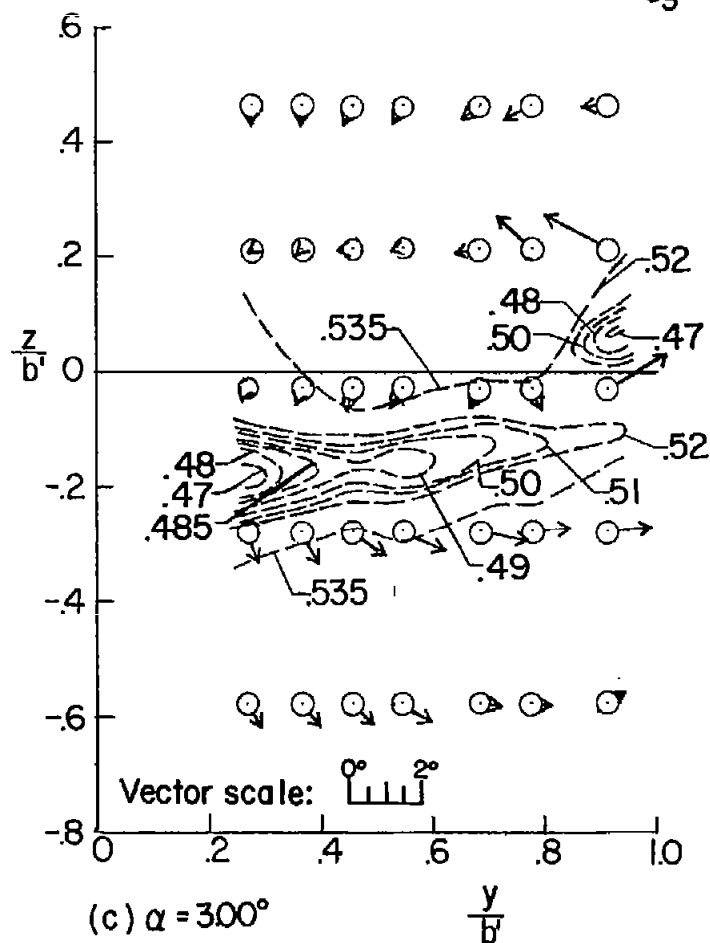
Figure 11.- Continued.

Dashed lines correspond to constant values of $\frac{H_3}{H_{o3}}$, as quoted.

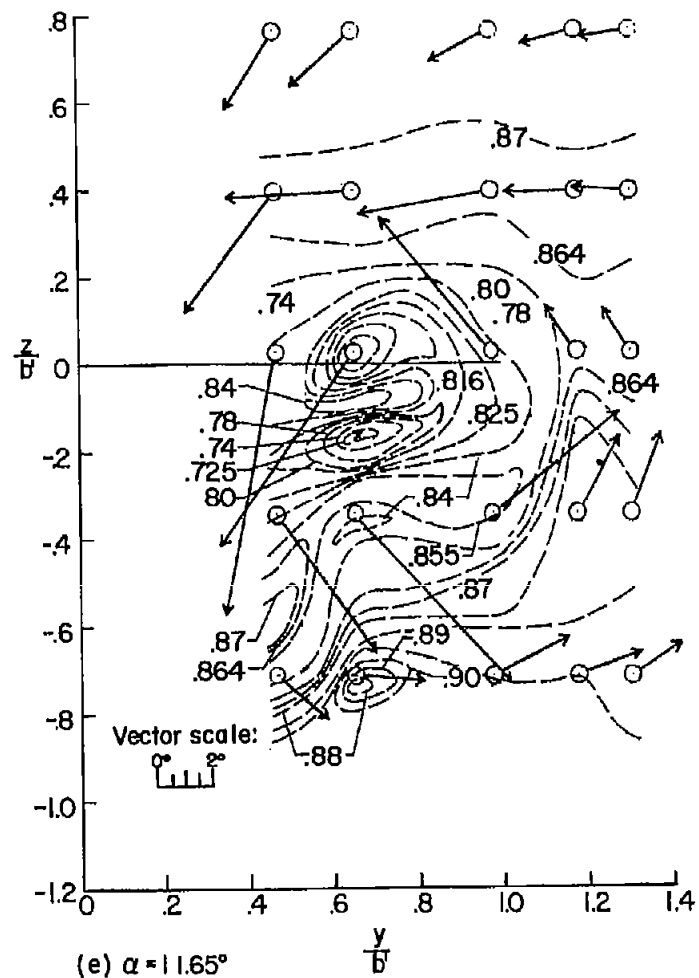$\frac{H_3}{H_{o3}}$ (Free stream) $= .536$

(e) $\alpha = 13.95°$
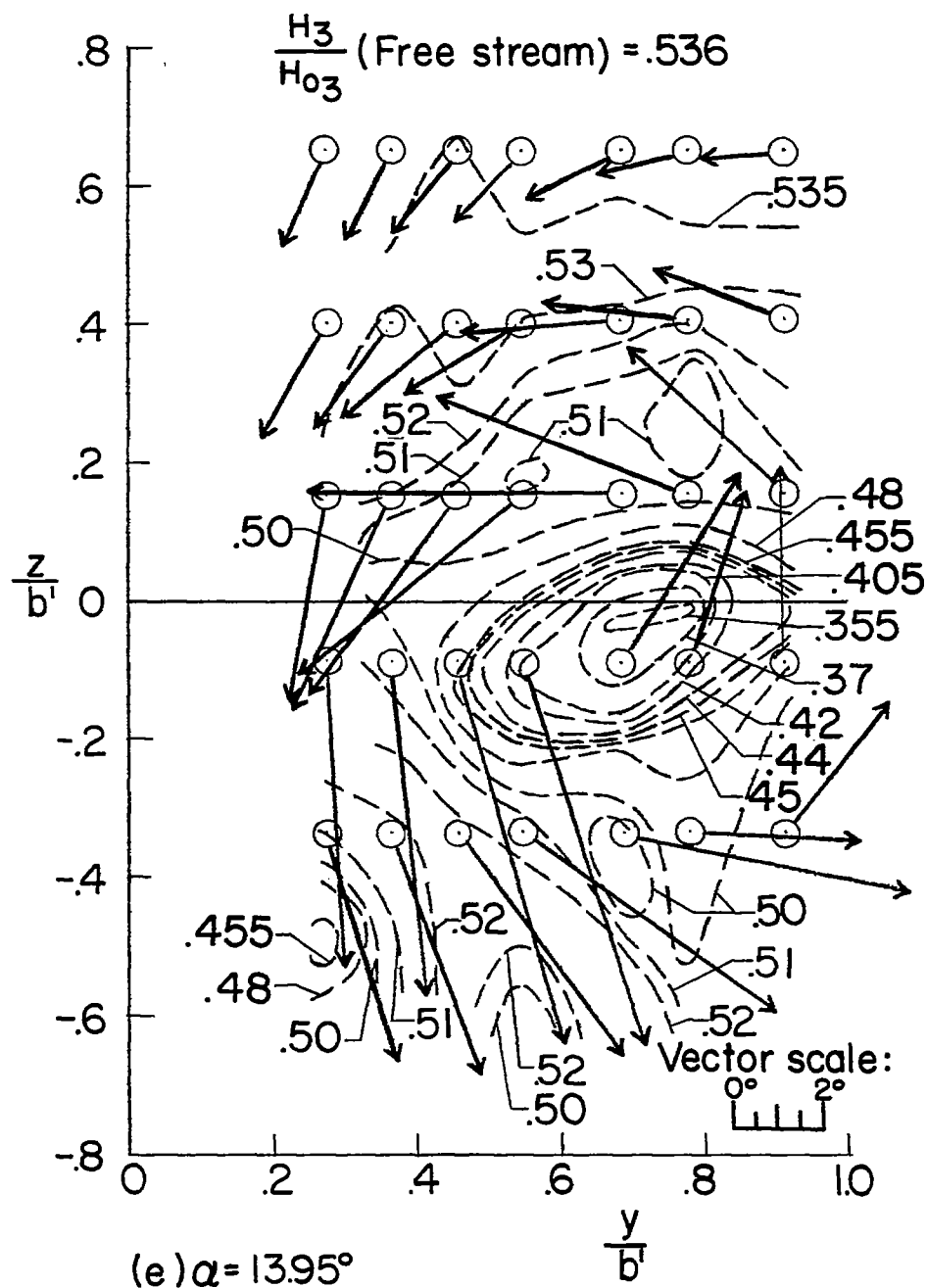
Figure 11.- Concluded.

Dashed lines correspond to constant values of $\frac{H_3}{H_{O_3}}$, as quoted.
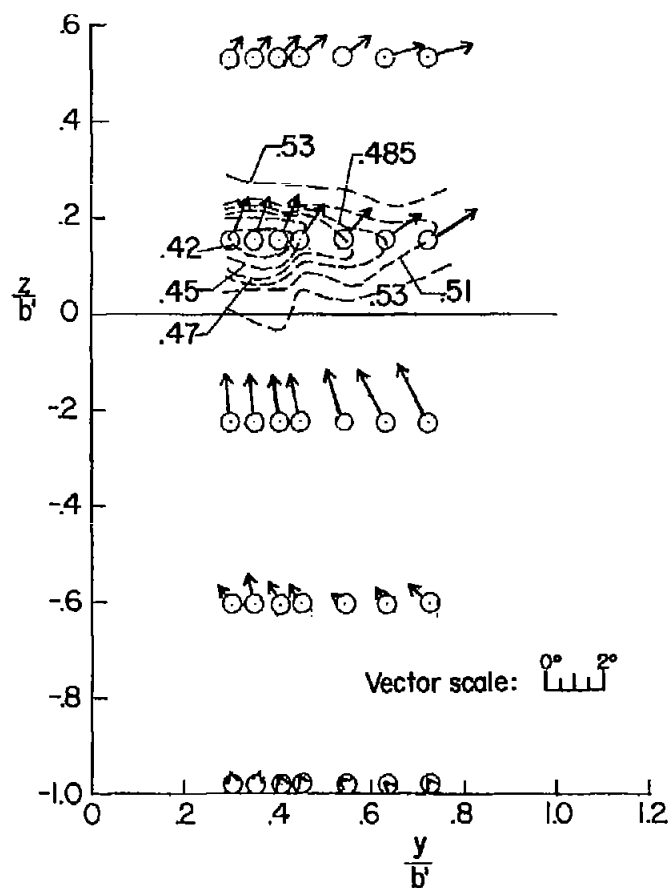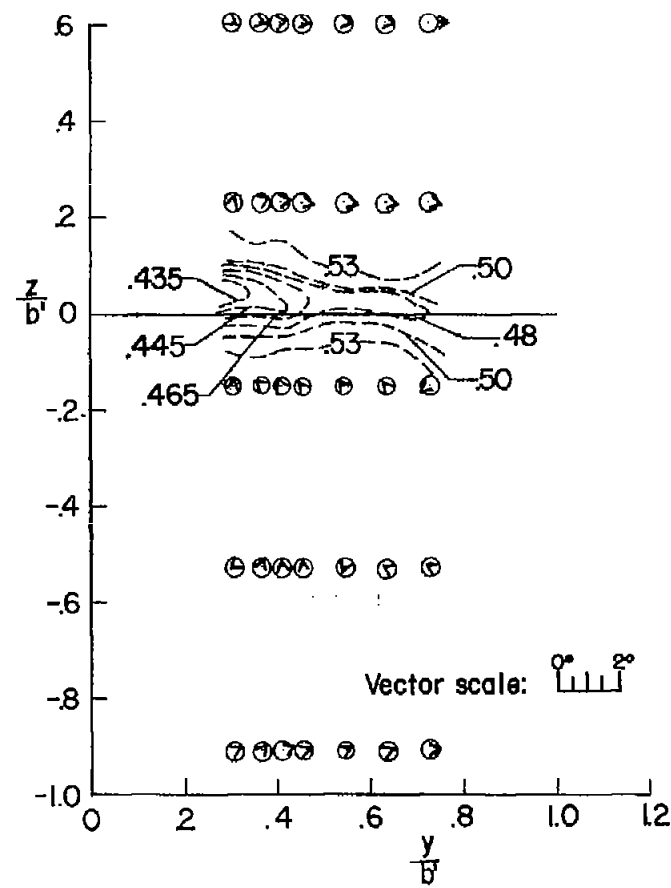
$\frac{H_3}{H_{O_3}}$ (Free stream) = .536

Figure 12.- Pressure contours and vector representation of the flow behind a triangular wing. $\Lambda = 72°$; $M = 2.41$; $x = 1.5c_r$; $R = 1.42 \times 10^6$.

(a) $\alpha = -3.10°$

(b) $\alpha = -0.10°$

Dashed lines correspond to constant values of $\frac{H_3}{H_{o_3}}$, as quoted.

$\frac{H_3}{H_{o_3}}$ (Free stream) = .536
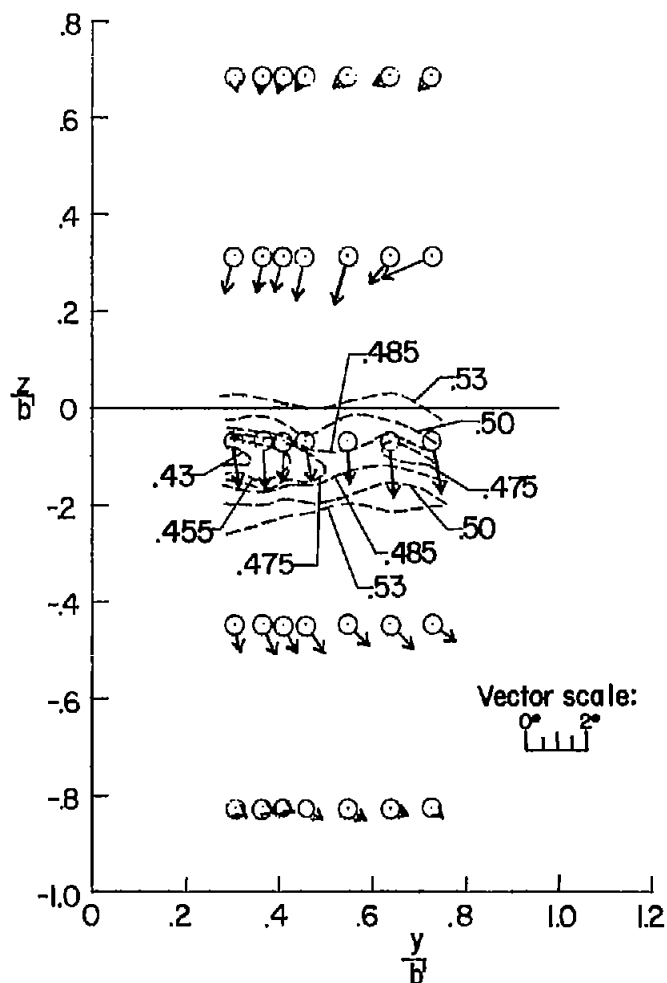
(c) $\alpha = 3.00°$
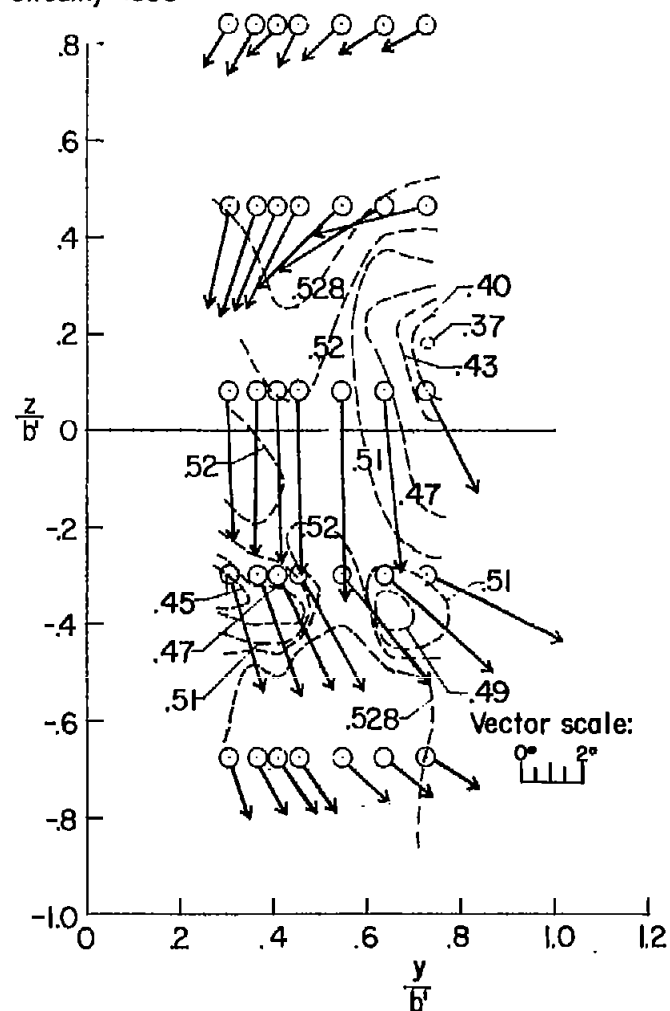
(d) $\alpha = 8.95°$

Figure 12.- Continued.

Dashed lines correspond to constant values of $\frac{H_3}{H_{o_3}}$, as quoted.

$\frac{H_3}{H_{o_3}}$ (Free stream) = .536

(e) $\alpha = 14.00°$

(f) $\alpha = 16.90°$

Vector scale:
0° 2°

.53

.52

.505

.50

.46

.425

.37

.32

.185

.25

.49

.46

.50

.505

.49

.49

.505

.52

.46

.54

.52

.49

.47

.45

.43

.40

.155

.17

.23

.36

.43

.47

.49

.52

.36

.38

.40

.43

$\frac{z}{b'}$

$\frac{y}{b}$
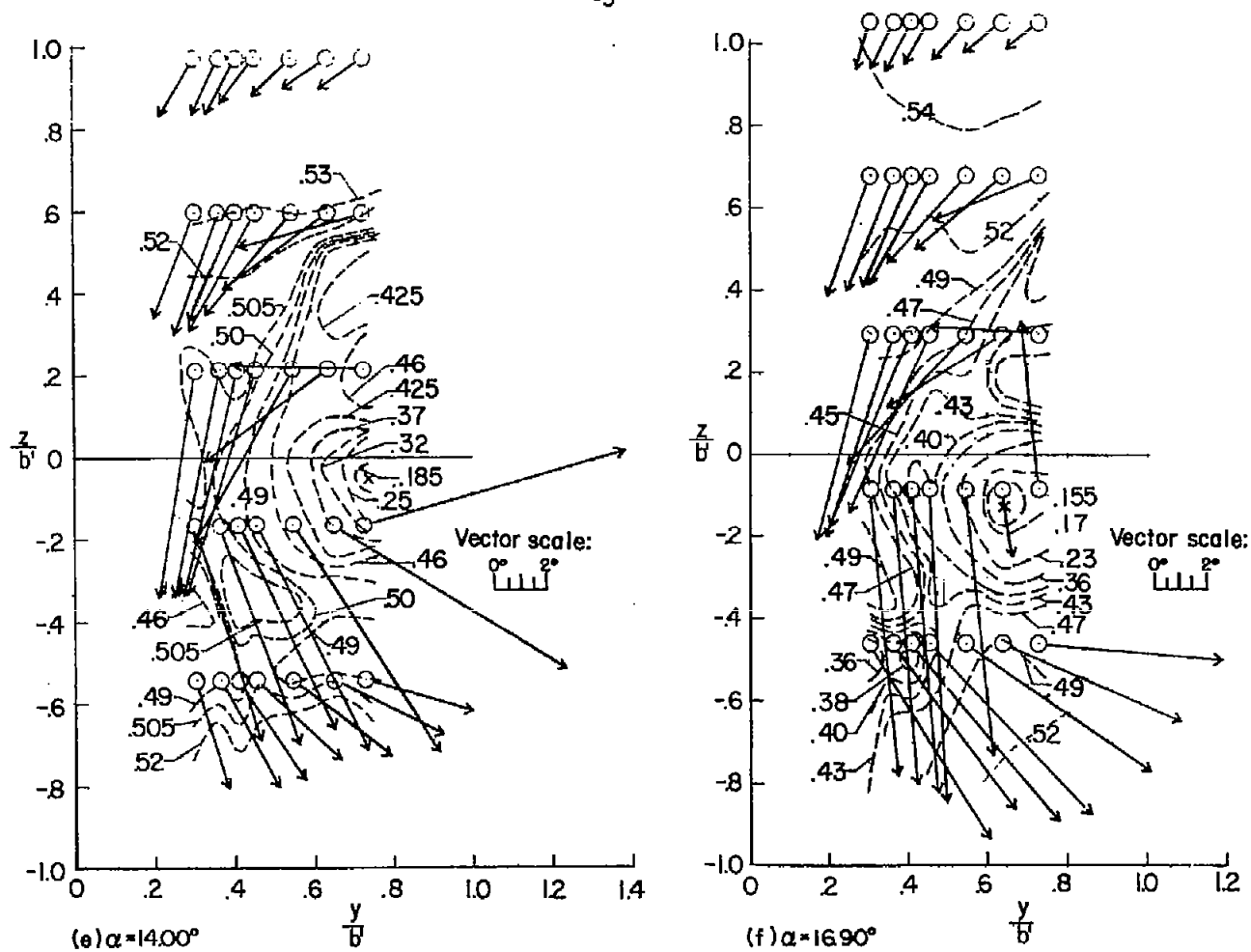
Figure 12.- Concluded.

Dashed lines correspond to constant values of $\frac{H_3}{H_{o_3}}$, as quoted.

$\frac{H_3}{H_{o_3}}$ (Free stream) = .536

(a) α = 14.00°

(b) α = 16.90°
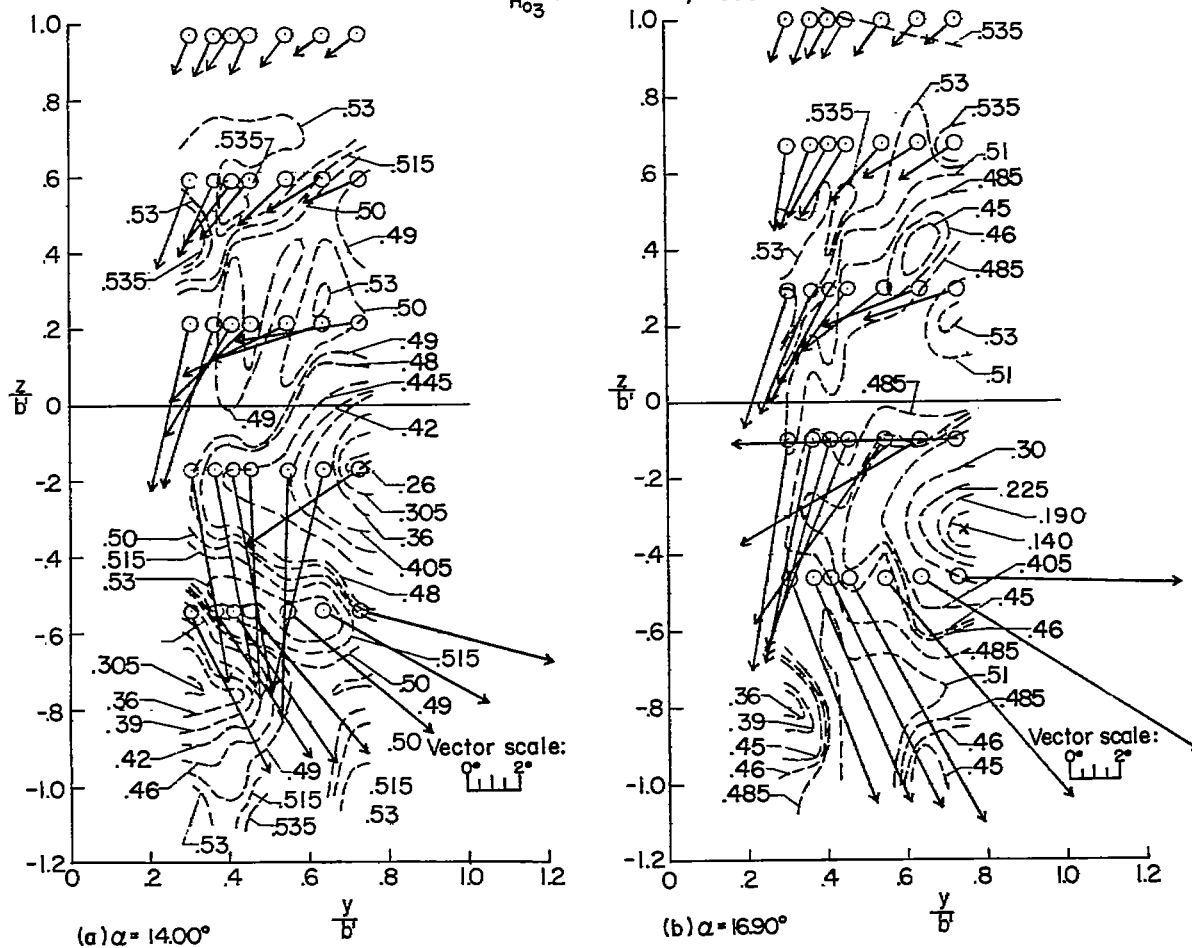
Figure 13.— Pressure contours and vector representation of the flow behind a triangular wing. Λ = 72°; M = 2.41; x = $3c_r$; R = 1.42 × 10^6.

Dashed lines correspond to constant values of $\frac{H_3}{H_{o_3}}$, as quoted.
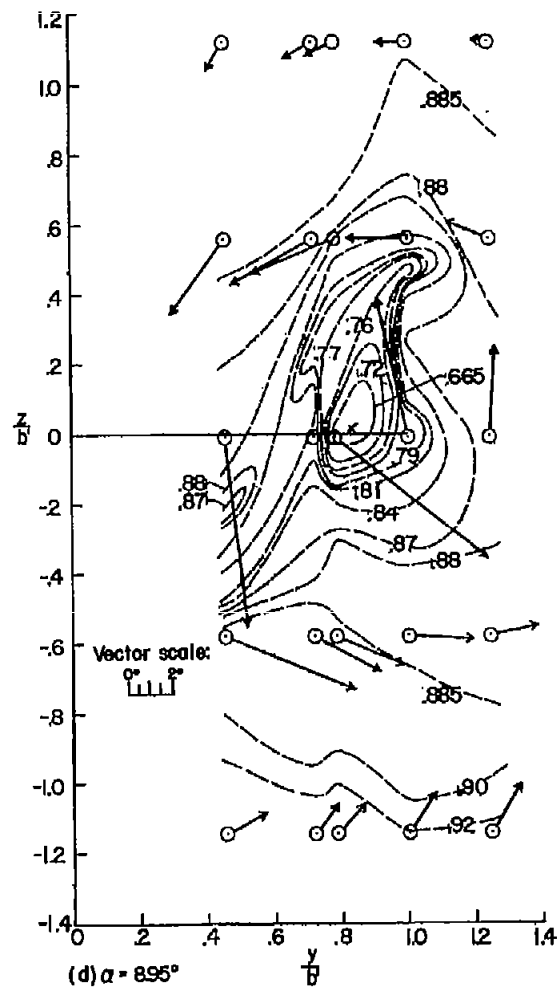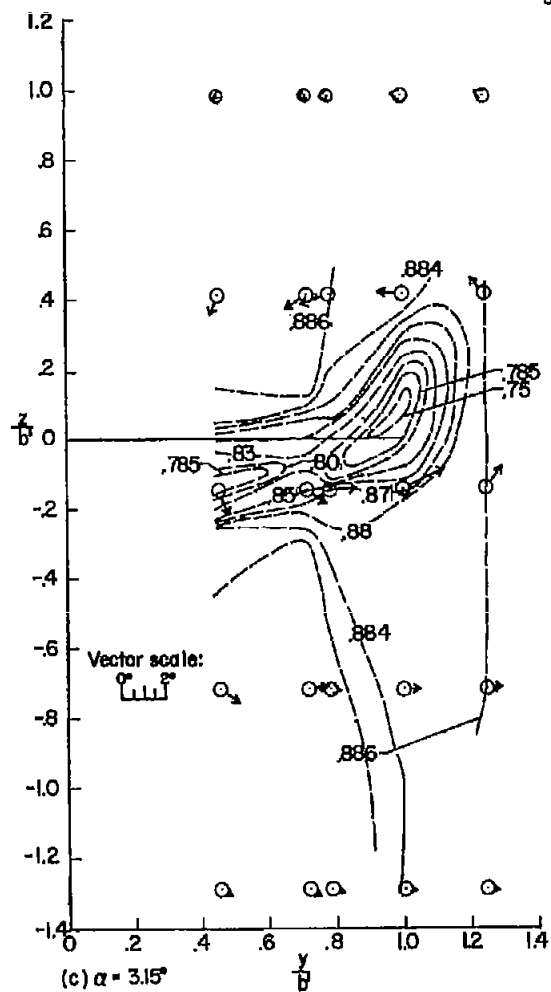
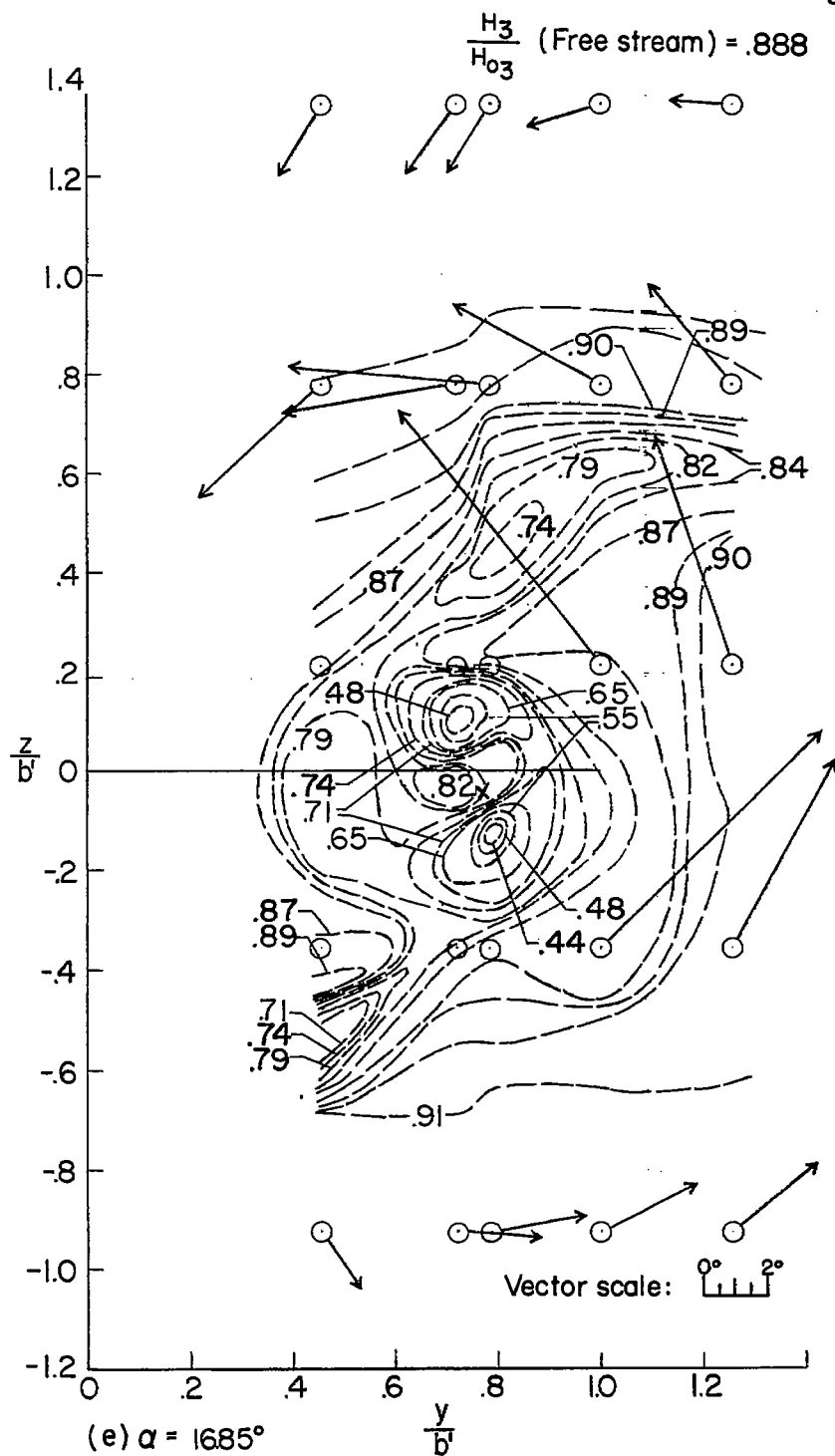$\frac{H_3}{H_{o_3}}$ (Free stream) = .536

(a) $\alpha = -3.10°$ (b) $\alpha = -0.10°$
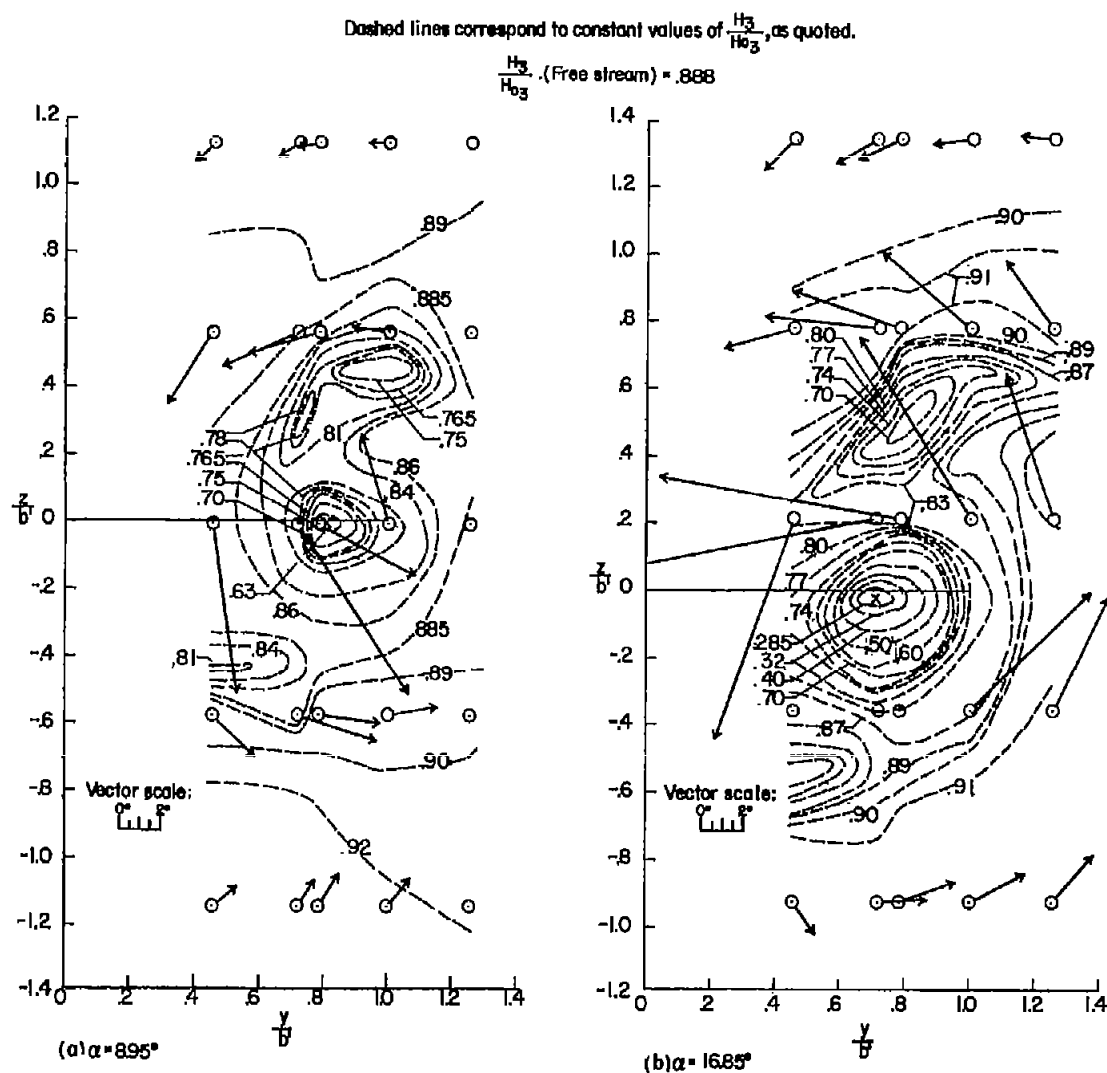
Figure 14.— Pressure contours and vector representation of the flow behind a triangular wing. $\Lambda = 72°$; $M = 2.41$; $x = 4c_r$; $R = 1.42 \times 10^6$.

Dashed lines correspond to constant values of $\frac{H_3}{H_{o_3}}$, as quoted.

$\frac{H_3}{H_{o_3}}$ (Free stream) = .536

(c) α = 3.00°

(d) α = 14.00°
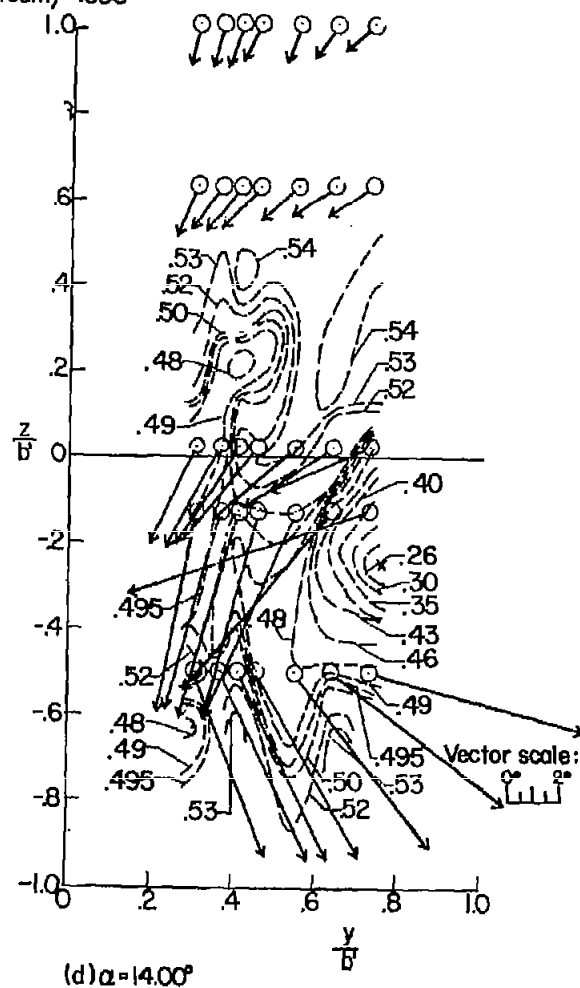
Figure 14.- Continued.

Dashed lines correspond to constant values of $\frac{H_3}{H_{o_3}}$, as quoted.

$\frac{H_3}{H_{o_3}}$ (Free stream) = .536

(e) α = 16.90°

Vector scale: 0° 2°

Figure 14.- Concluded.

Dashed lines correspond to constant values of $\frac{H_3}{H_{o_3}}$, as quoted.

$\frac{H_3}{H_{o_3}}$ (Free stream) = .888

(a) $\alpha = -3.40°$

(b) $\alpha = -0.45°$
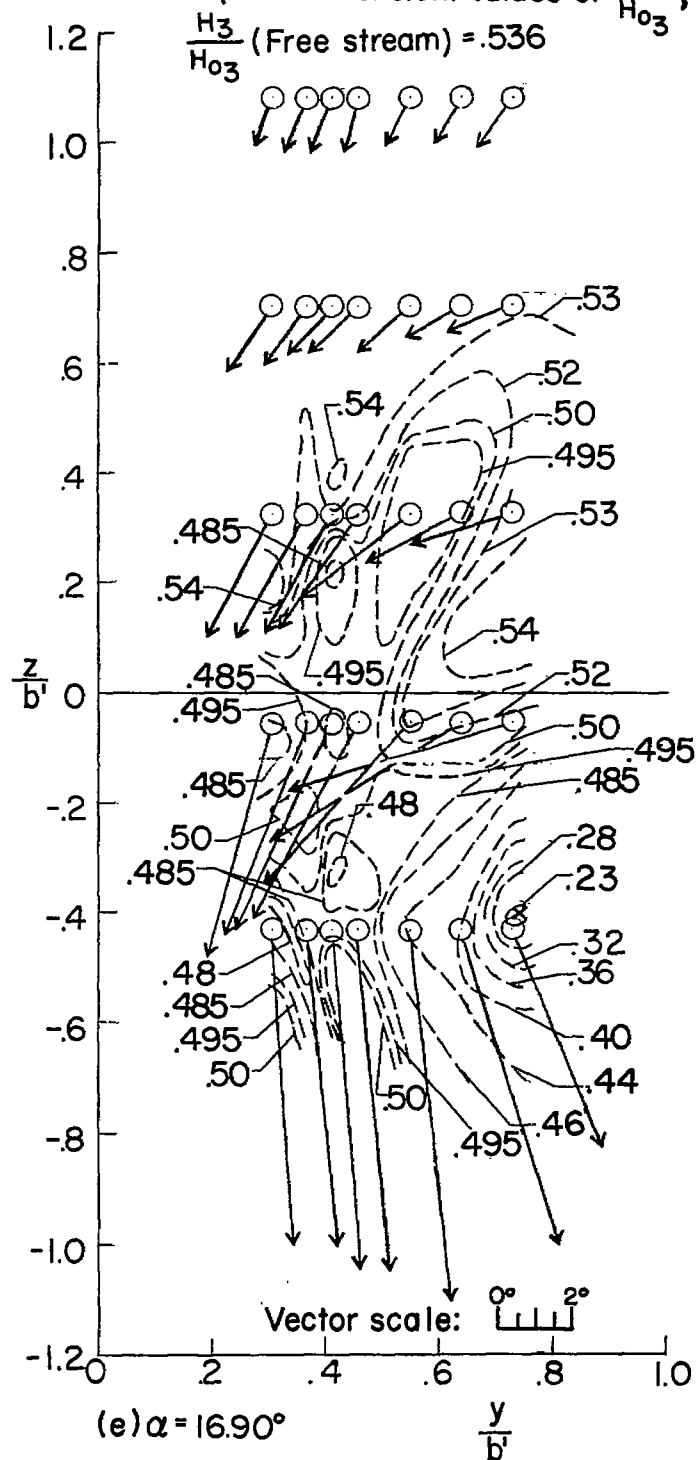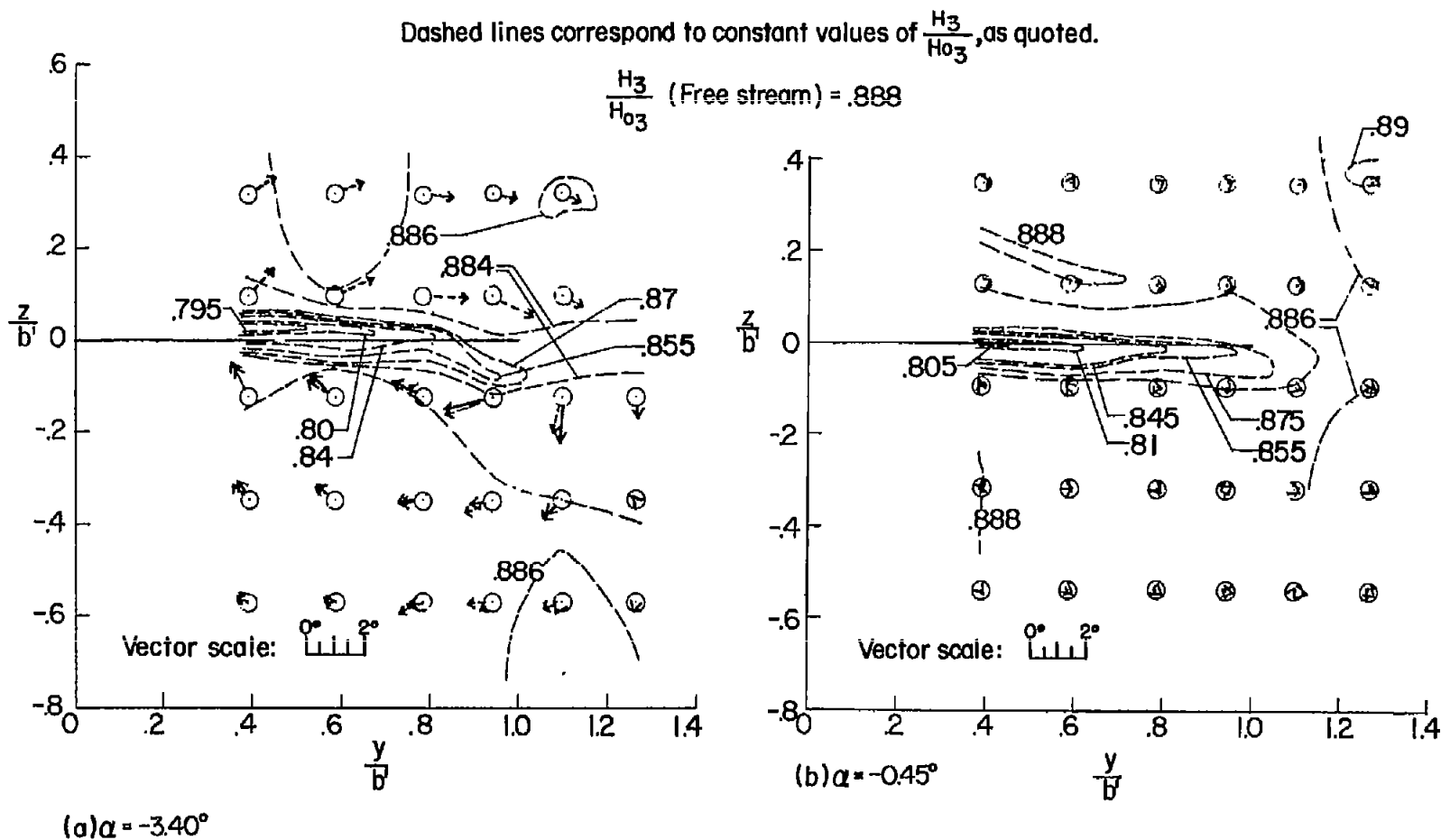
Figure 15.- Pressure contours and vector representation of the flow behind a triangular wing. $\Lambda = 50°$; $M = 1.62$; $x = 1.5c_r$; $R = 0.71 \times 10^6$ and 1.42×10^6.
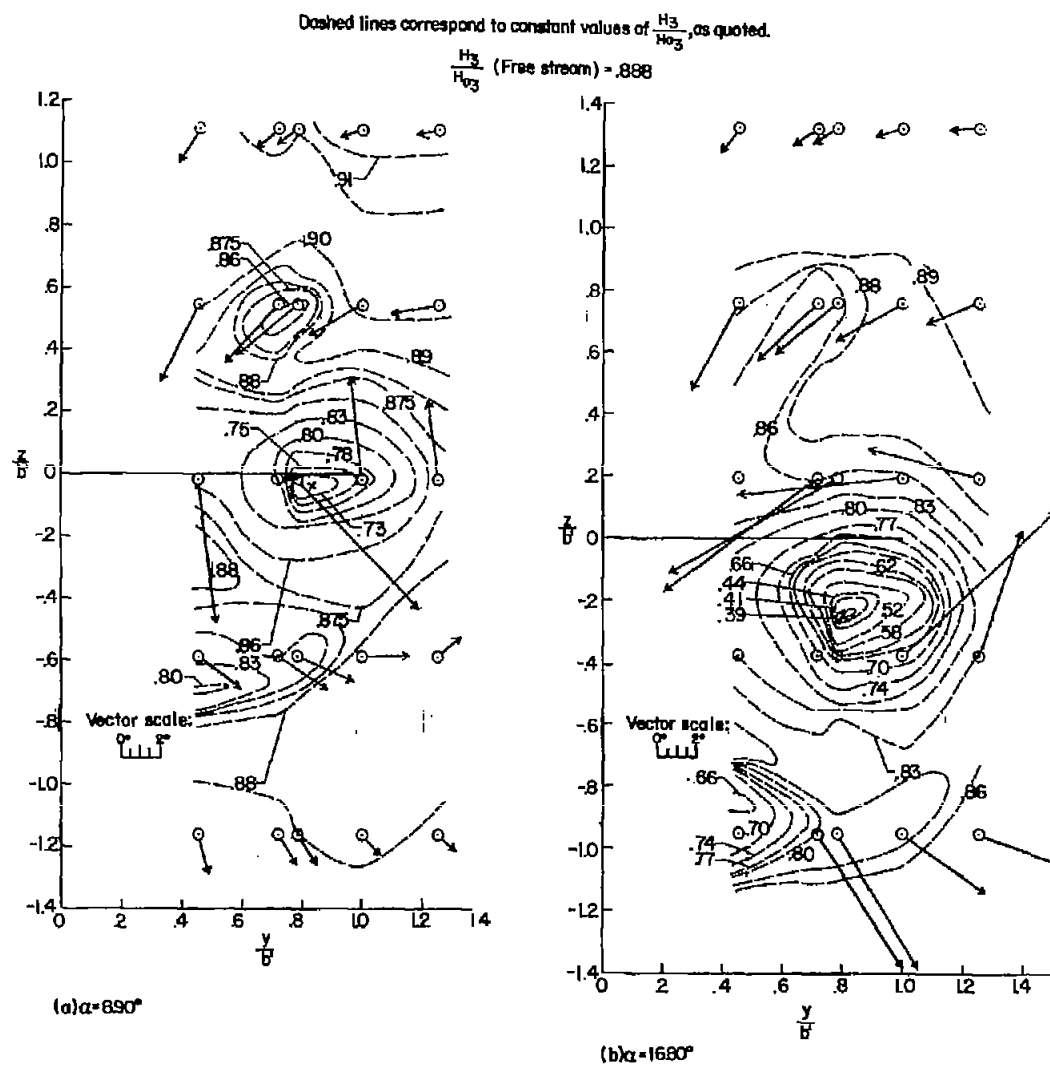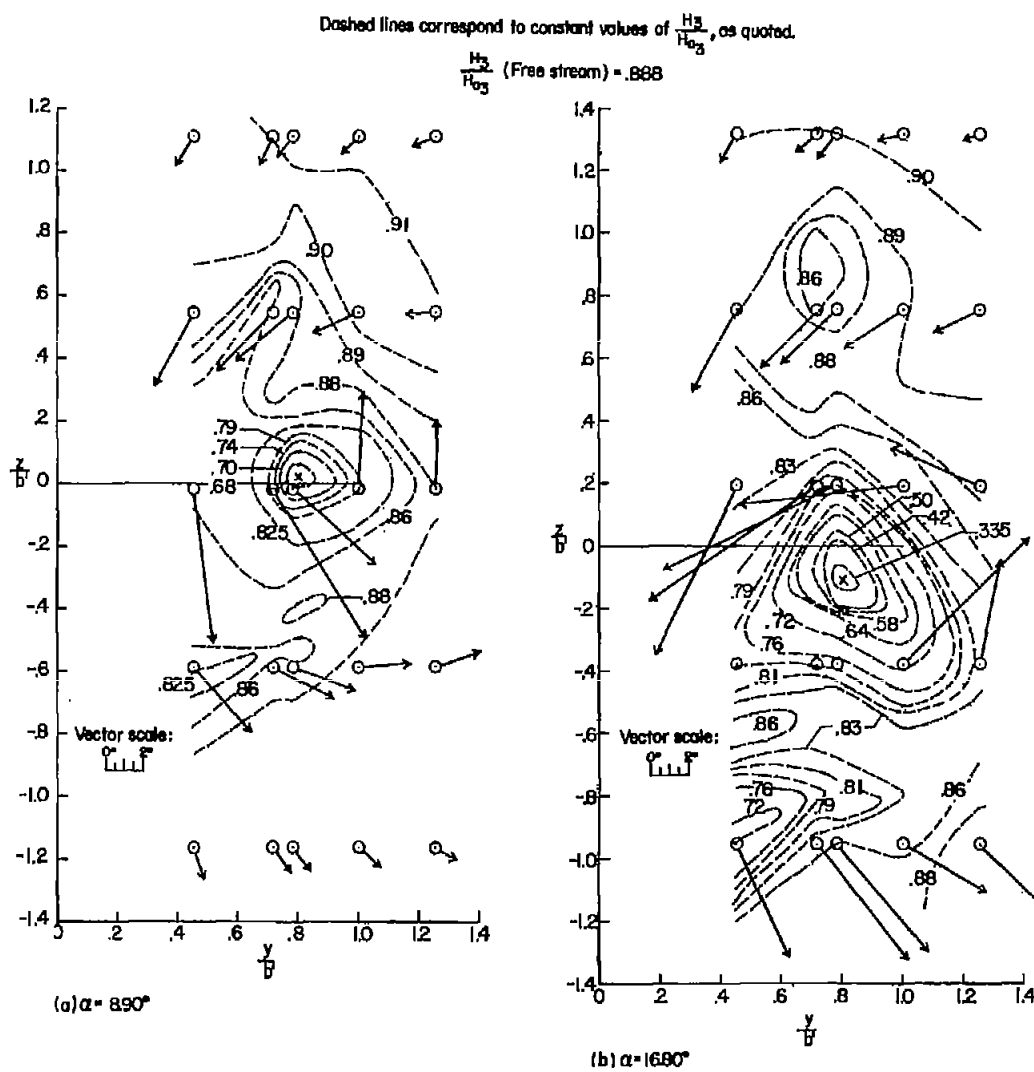
Dashed lines correspond to constant values of $\frac{H_3}{H_{o_3}}$, as quoted.
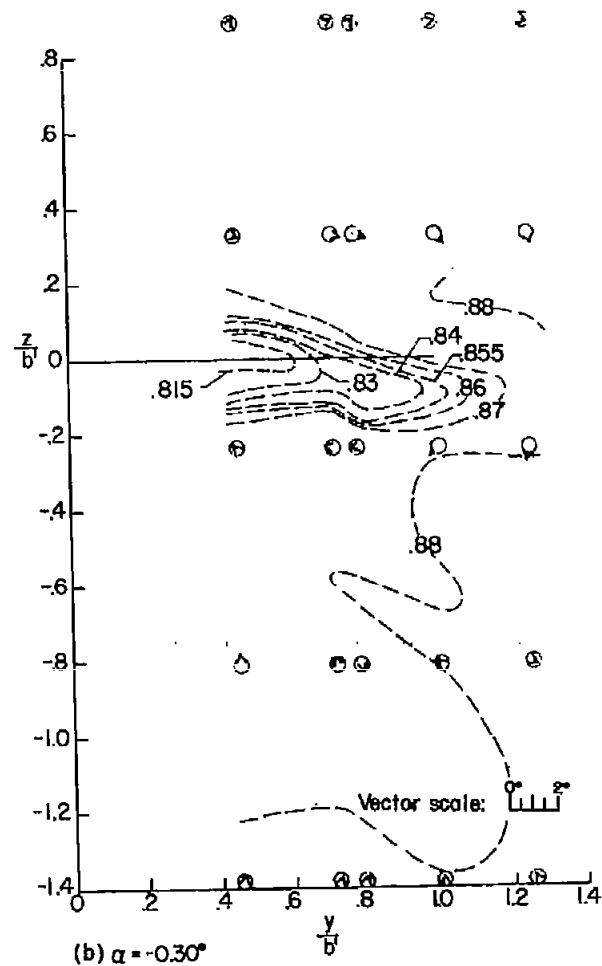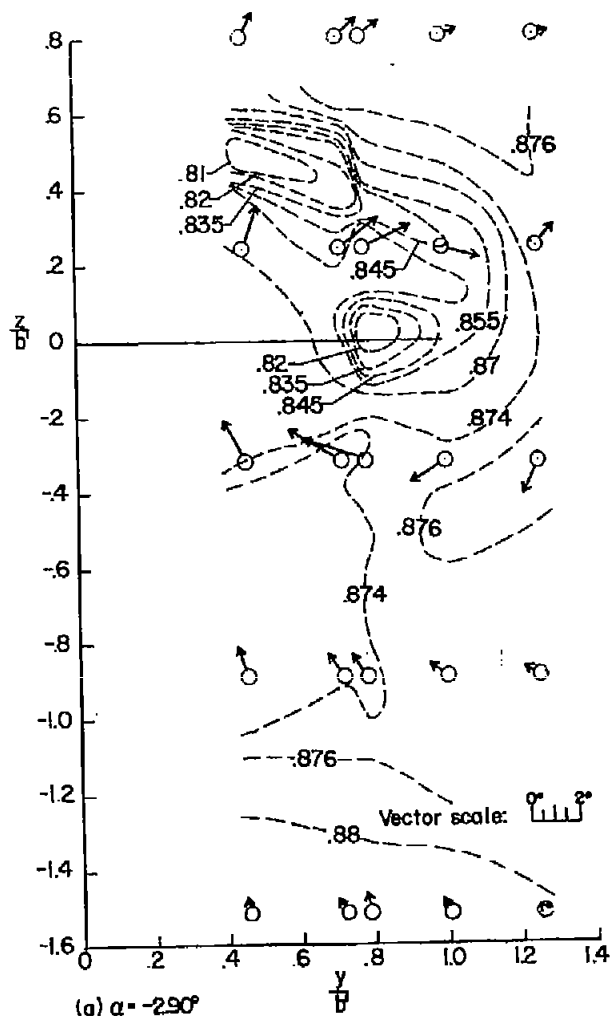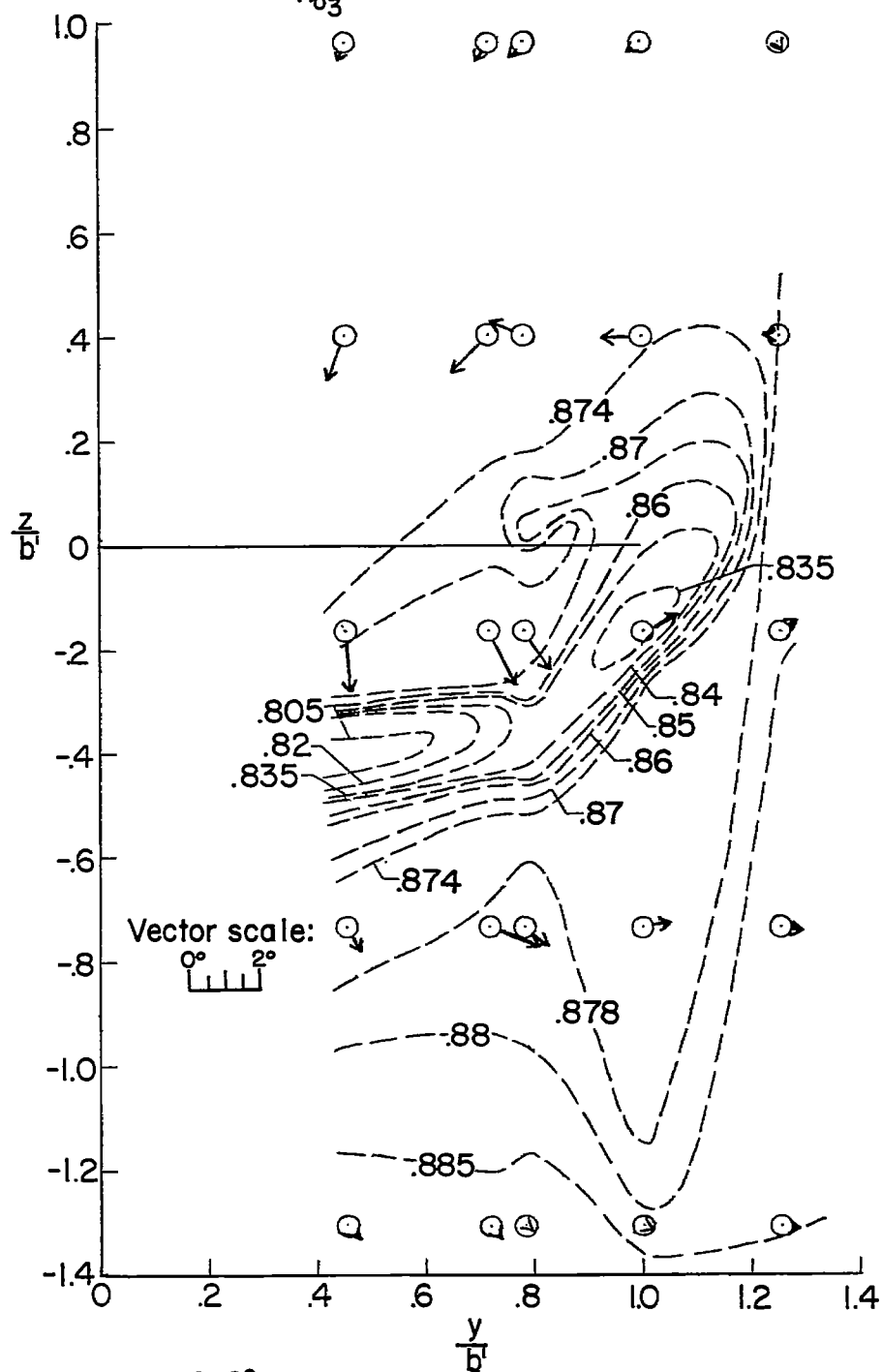
$\frac{H_3}{H_{o_3}}$ (Free stream) = .888

(c) $\alpha = 2.70°$

(d) $\alpha = 8.60°$
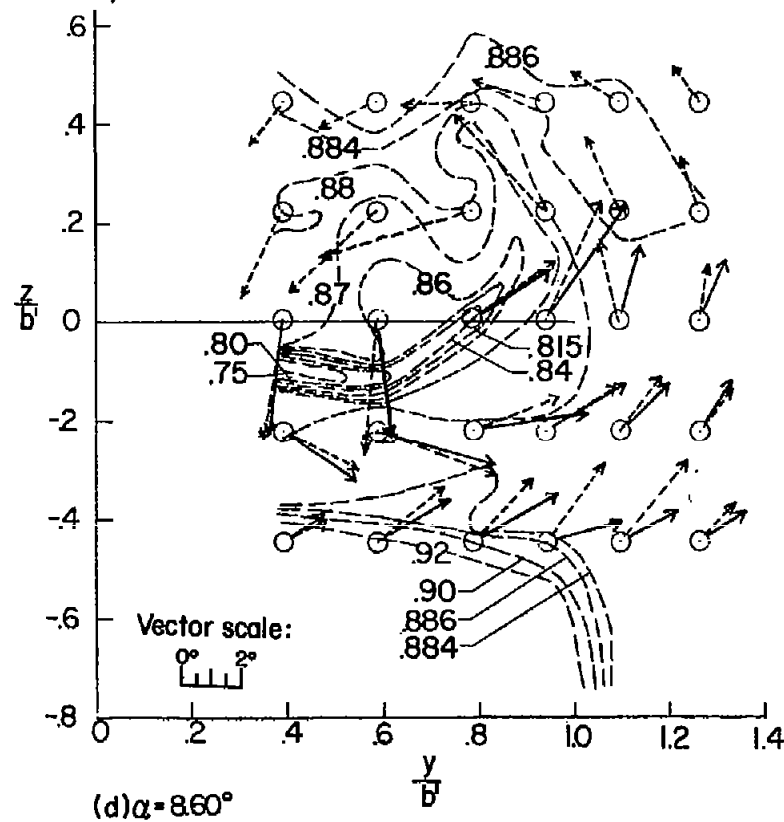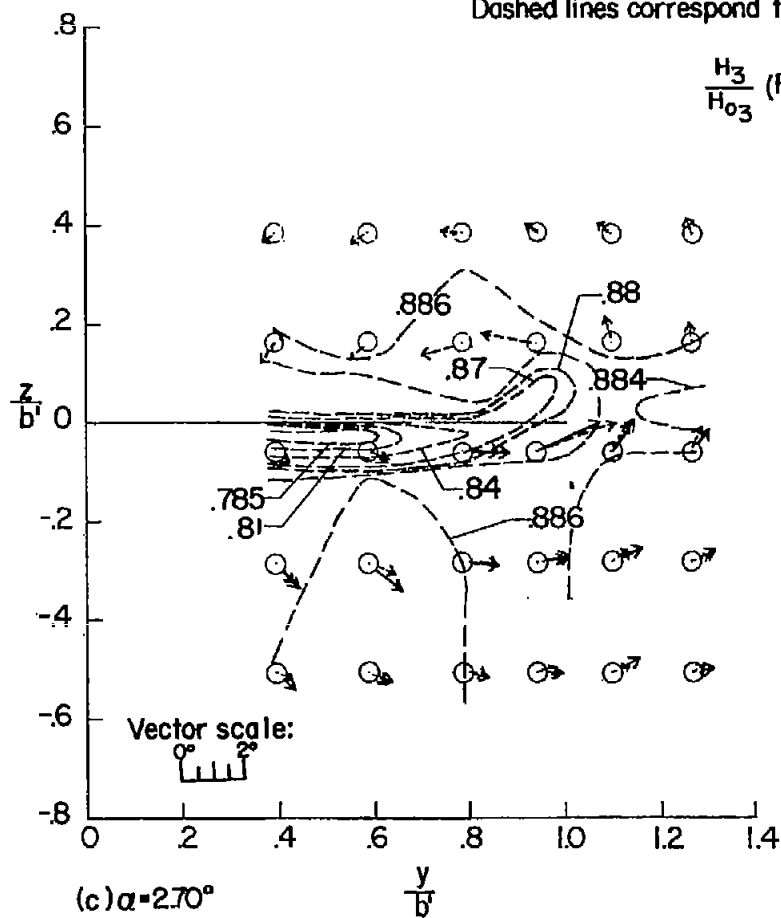
Figure 15.— Concluded.

Dashed lines correspond to constant values of $\frac{H_3}{H_{o_3}}$, as quoted.

$\frac{H_3}{H_{o_3}}$ (Free stream) = .888

(a) $\alpha = -3.40°$

(b) $\alpha = -0.50°$

Figure 16.— Pressure contours and vector representation of the flow behind a triangular wing. $\Lambda = 50°$; $M = 1.62$; $x = 3c_r$; $R = 1.42 \times 10^6$.

Dashed lines correspond to constant values of $\frac{H_3}{H_{o_3}}$, as quoted.

(c) $\alpha = 2.65°$

Figure 16.- Concluded.

Dashed lines correspond to constant values of $\frac{H_3}{H_{o_3}}$, as quoted.

$\frac{H_3}{H_{o_3}}$ (Free stream) = .888

(a) $\alpha = -3.40°$

(b) $\alpha = -0.50°$
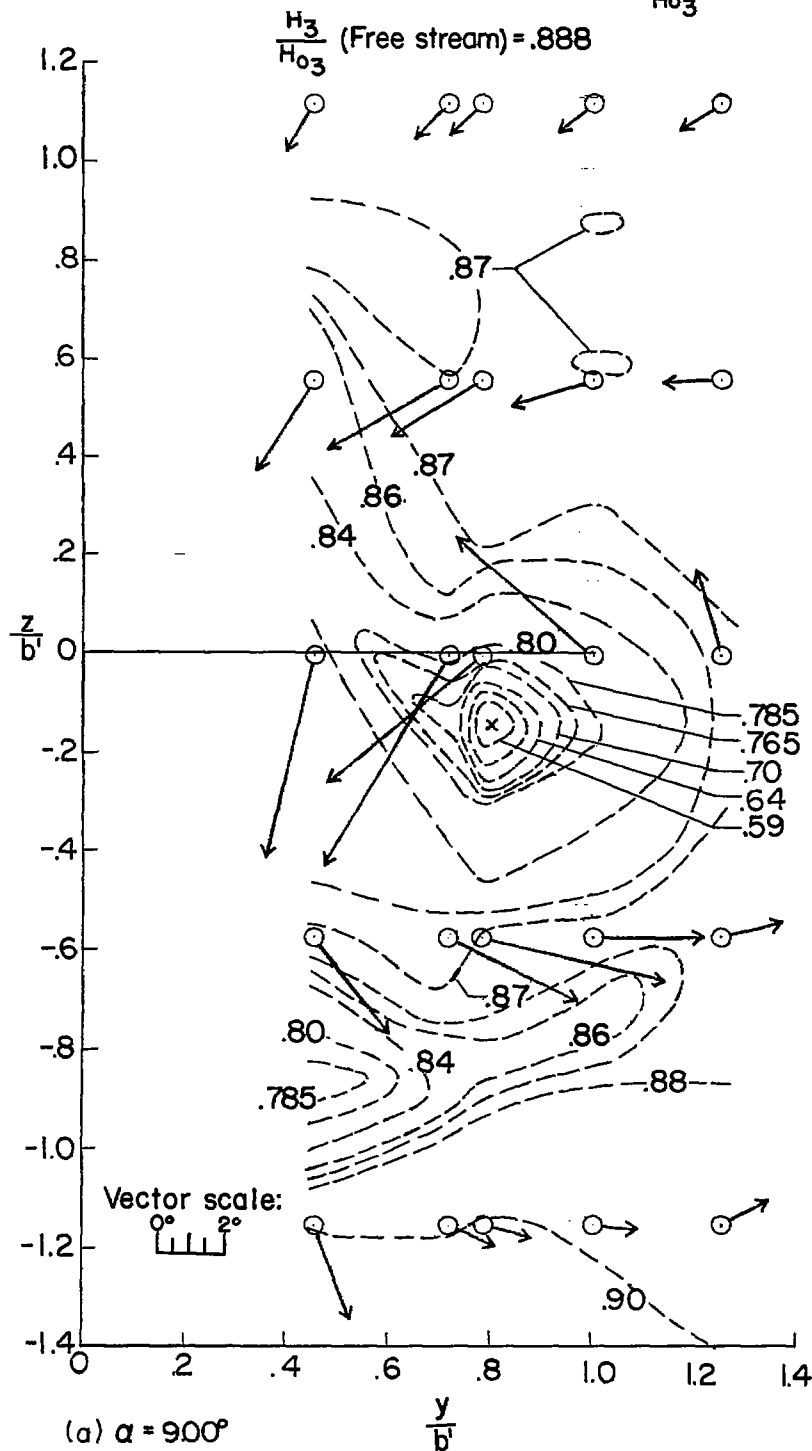
Figure 17.- Pressure contours and vector representation of the flow behind a triangular wing. $\Lambda = 50°$; $M = 1.62$; $x = 4c_r$; $R = 0.71 \times 10^6$ and 1.42×10^6.

Dashed lines correspond to constant values of $\frac{H_3}{H_{o_3}}$, as quoted.

$\frac{H_3}{H_{o_3}}$ (Free stream) = .888

(c) $\alpha = 2.60°$

(d) $\alpha = 8.50°$

Figure 17.- Concluded.

Dashed lines correspond to constant values of $\frac{H_3}{H_{o_3}}$, as quoted.

$\frac{H_3}{H_{o_3}}$ (Free stream) = .888

(a) $\alpha = -3.05°$

(b) $\alpha = -0.15°$

Figure 18.- Pressure contours and vector representation of the flow behind a triangular wing. $\Lambda = 63°$; $M = 1.62$; $x = 1.5c_r$; $R = 1.42 \times 10^6$.

Dashed lines correspond to constant values of $\frac{H_3}{H_{o_3}}$, as quoted.

$\frac{H_3}{H_{o_3}}$ (Free stream) = .888

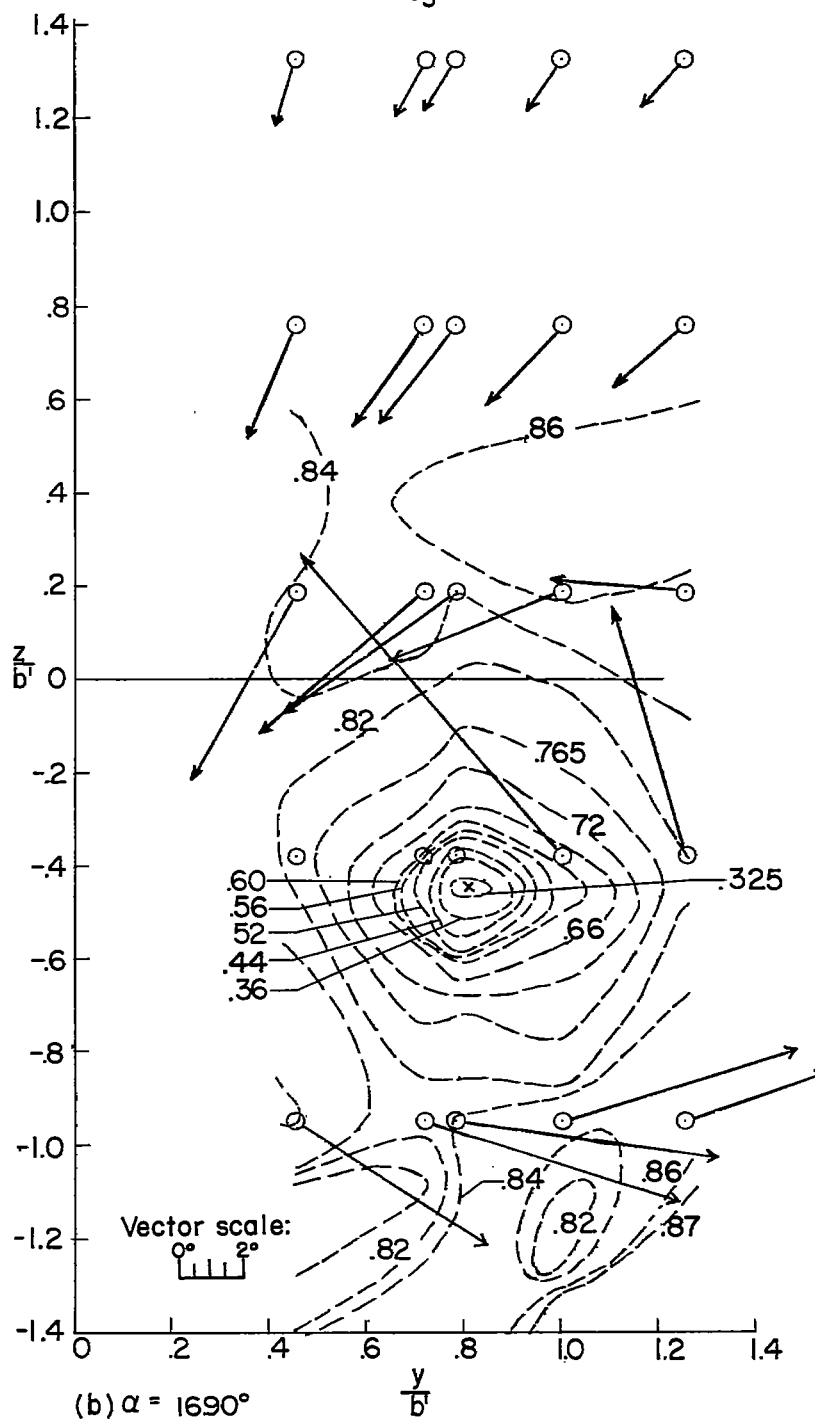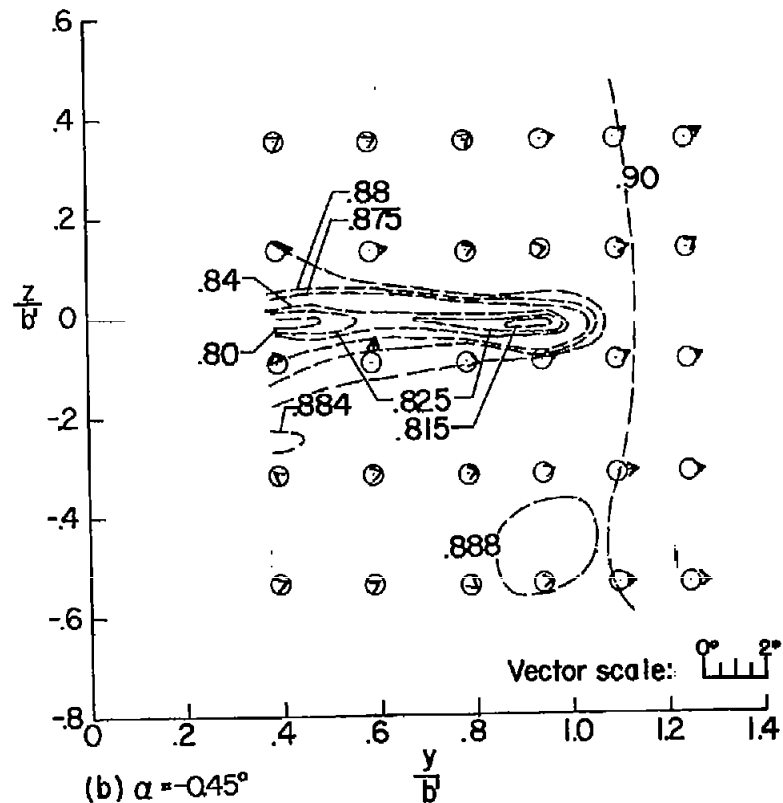(c) $\alpha = 3.00°$

(d) $\alpha = 8.95°$

Figure 18.- Continued.

Dashed lines correspond to constant values of $\frac{H_3}{H_{O_3}}$, as quoted.

$\frac{H_3}{H_{O_3}}$ (Free stream) = .888

(e) $\alpha = 11.90°$

Figure 18.- Concluded.

Dashed lines correspond to constant values of $\frac{H_3}{H_{o_3}}$, as quoted.
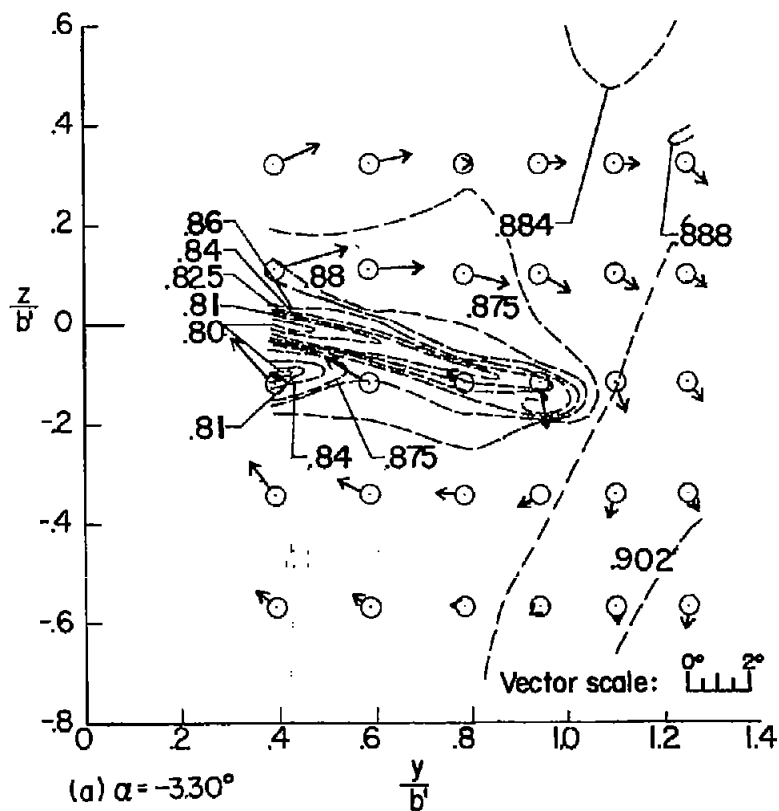
$\frac{H_3}{H_{o_3}}$ (Free stream) = .888

(a) $\alpha = 8.55°$
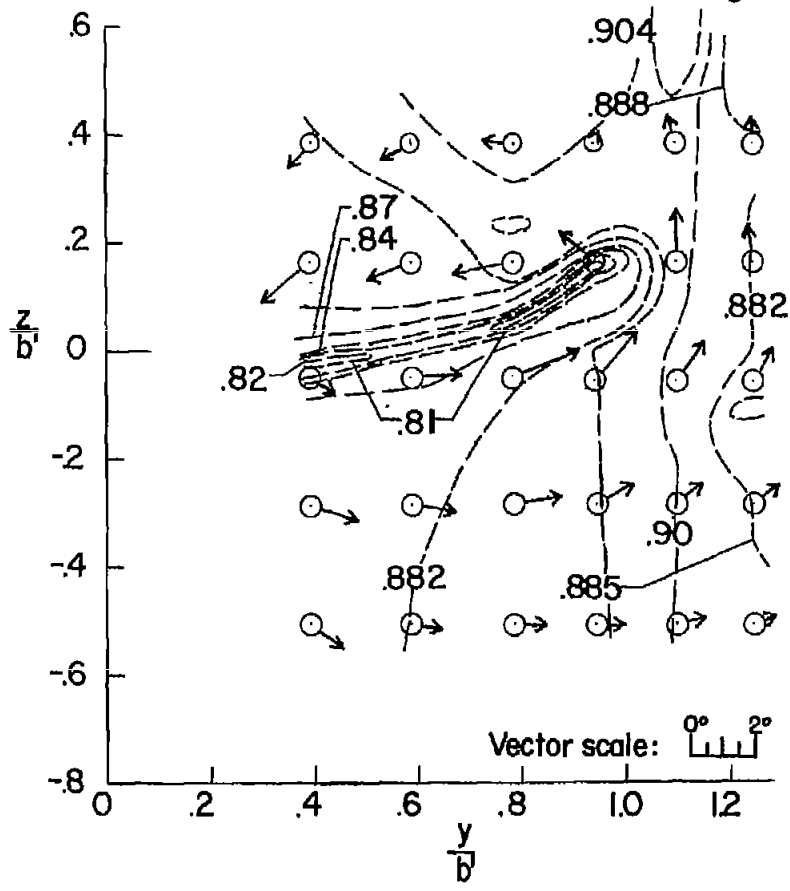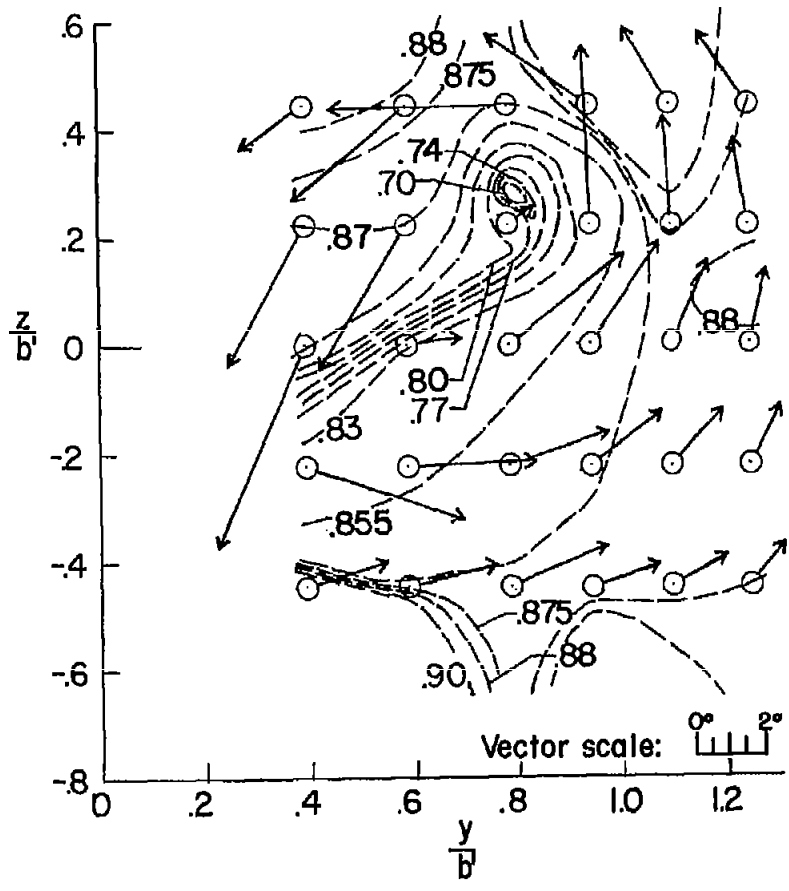
(b) $\alpha = 11.65°$

Figure 19.— Pressure contours and vector representation of the flow behind a triangular wing. $\Lambda = 63°$; $M = 1.62$; $x = 3c_r$; $R = 1.42 \times 10^6$.

Dashed lines correspond to constant values of $\frac{H_3}{H_{O_3}}$, as quoted.

$\frac{H_3}{H_{O_3}}$ (Free stream) = .888

(a) $\alpha = -3.30°$

(b) $\alpha = -0.35°$
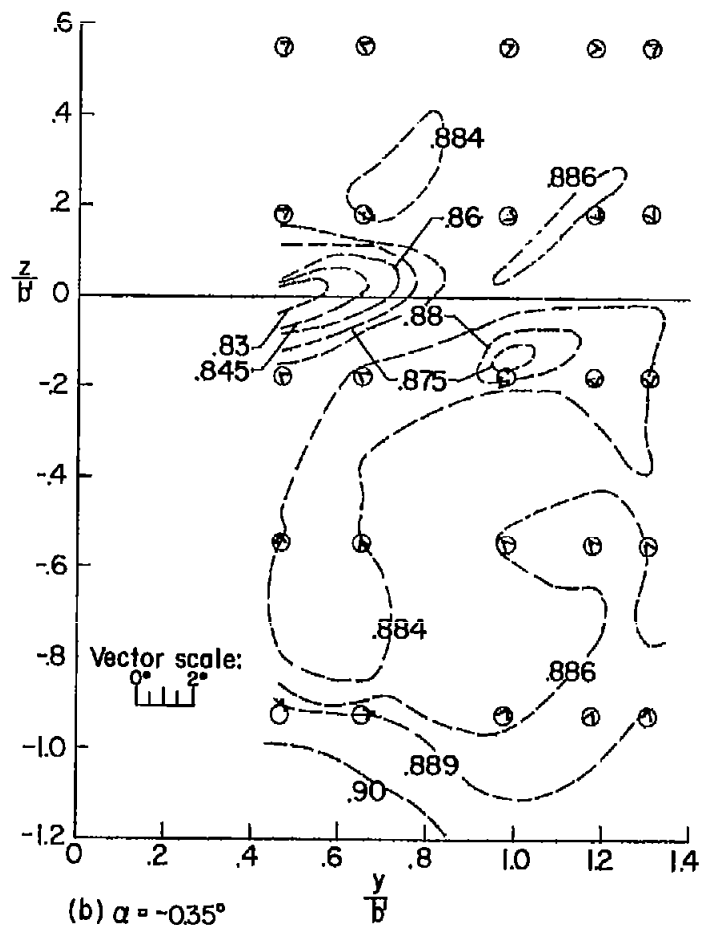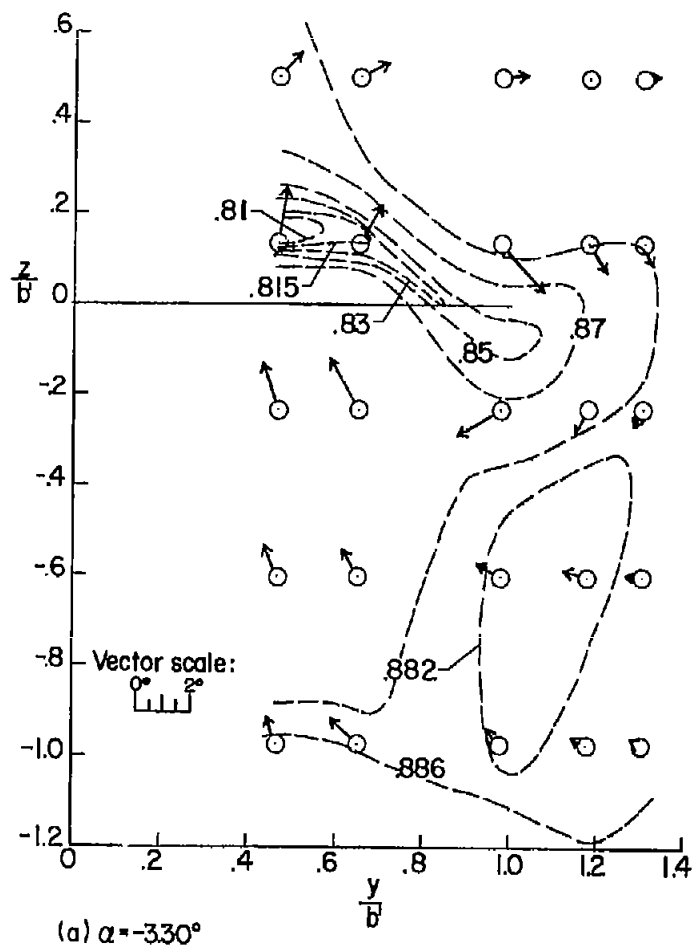
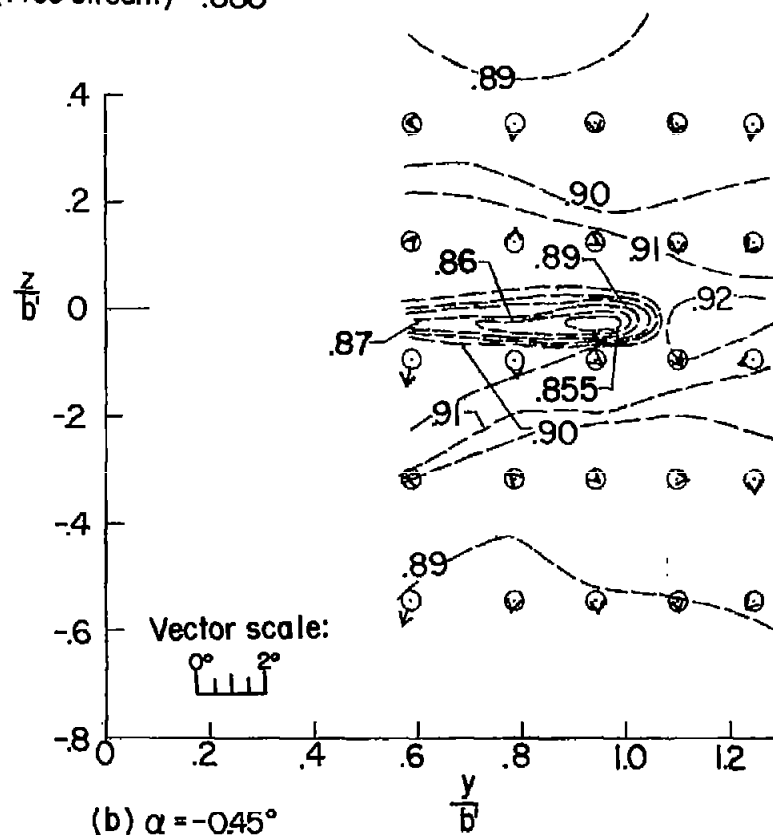Figure 20.- Pressure contours and vector representation of the flow behind a triangular wing. $\Lambda = 63°$; $M = 1.62$; $x = 4c_r$; $R = 1.42 \times 10^6$.

Dashed lines correspond to constant values of $\frac{H_3}{H_{o_3}}$, as quoted.

$\frac{H_3}{H_{o_3}}$ (Free stream) = .888

(c) $\alpha = 2.85°$

Figure 20.- Continued.

Dashed lines correspond to constant values of $\frac{H_3}{H_{0_3}}$, as quoted.

$\frac{H_3}{H_{0_3}}$ (Free stream) = .888

(d) $\alpha = 8.90°$

(e) $\alpha = 11.65°$
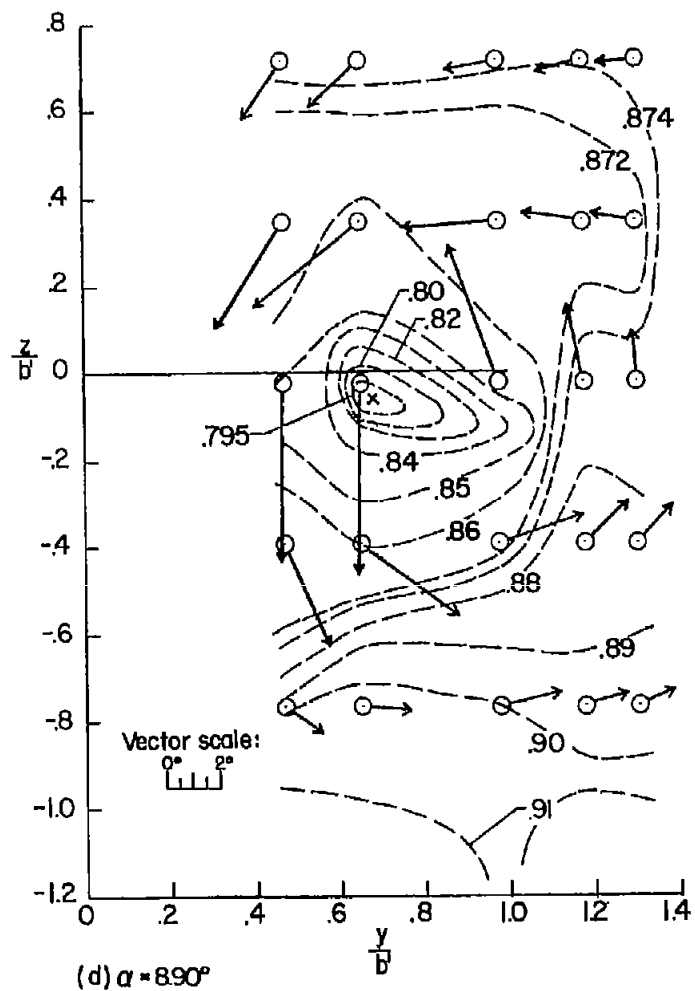
Figure 20.- Concluded.

Dashed lines correspond to constant values of $\frac{H_3}{H_{o_3}}$, as quoted.
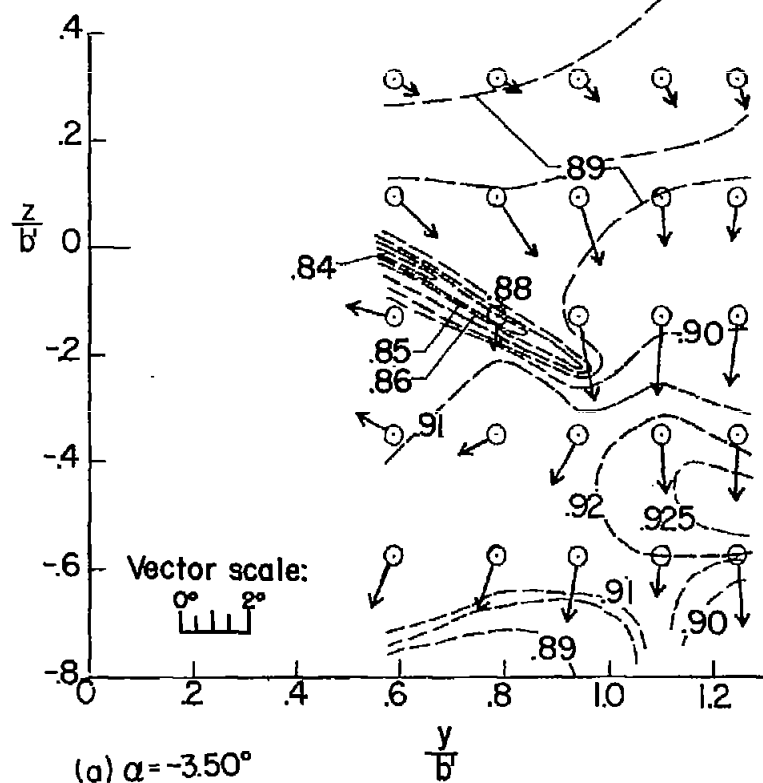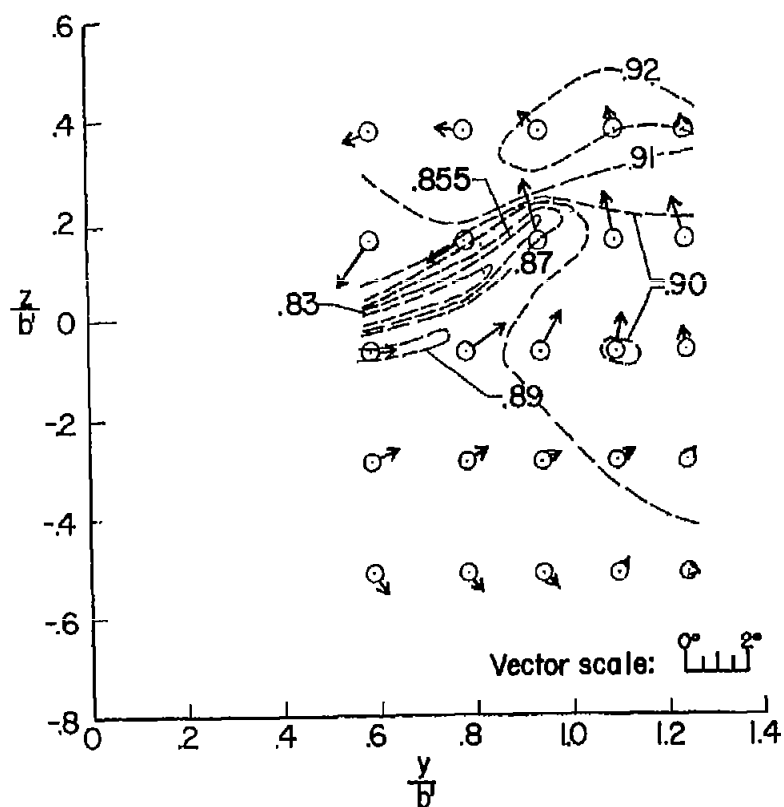
$\frac{H_3}{H_{o_3}}$ (Free stream) = .888

(a) $\alpha = -3.00°$

(b) $\alpha = 0.05°$

Vector scale:
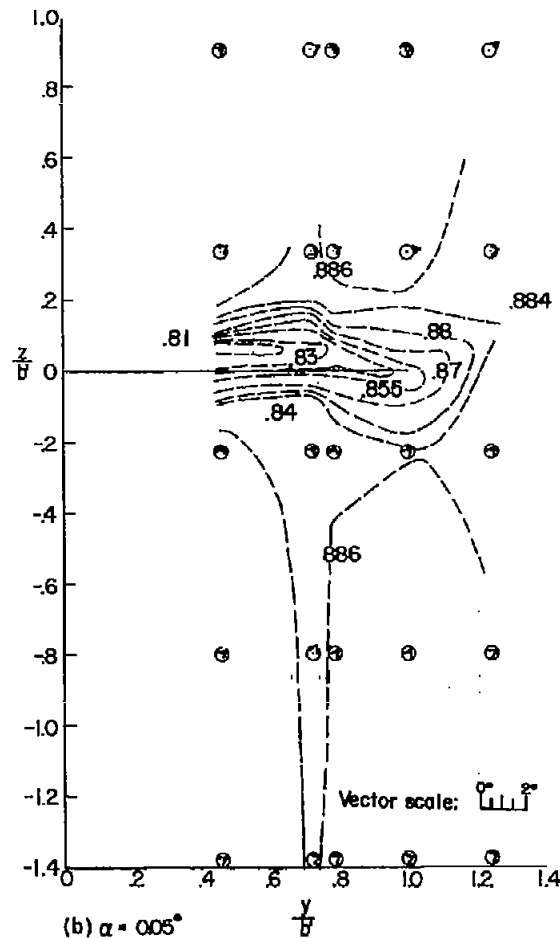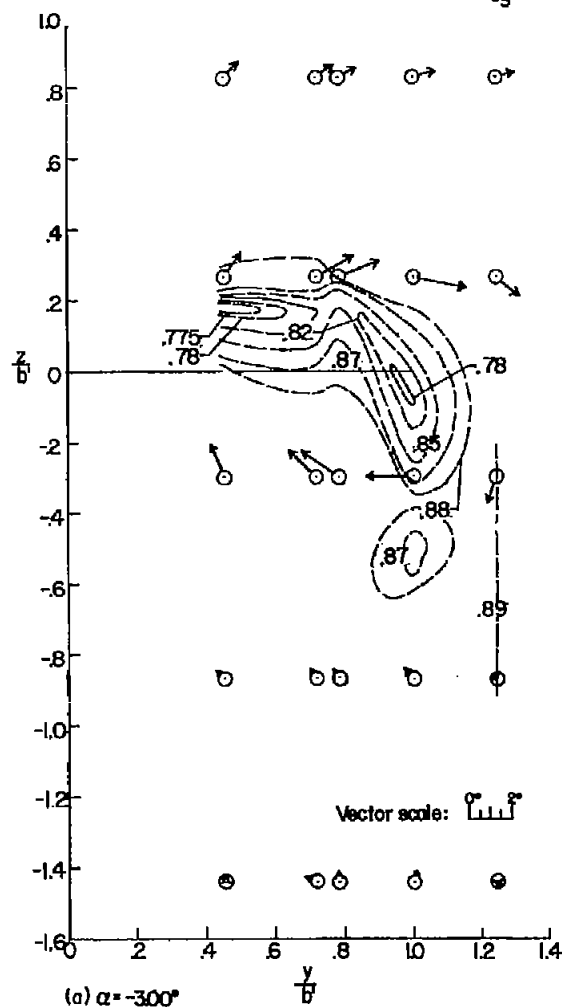
Figure 21.- Pressure contours and vector representation of the flow behind a triangular wing. $\Lambda = 72°$; $M = 1.62$; $x = 1.5c_r$; $R = 1.42 \times 10^6$.

Dashed lines correspond to constant values of $\frac{H_3}{H_{o_3}}$, as quoted.
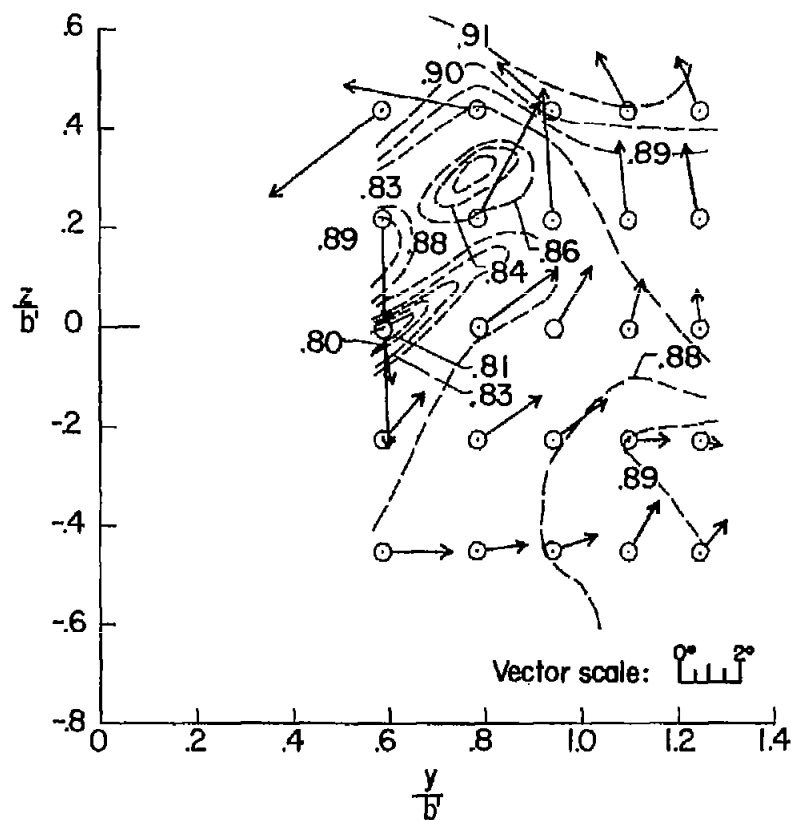
$\frac{H_3}{H_{o_3}}$ (Free stream) = .888

(c) $\alpha = 3.15°$

(d) $\alpha = 8.95°$

Figure 21.- Continued.

Dashed lines correspond to constant values of $\dfrac{H_3}{H_{o_3}}$, as quoted.

$\dfrac{H_3}{H_{o_3}}$ (Free stream) = .888

.89

.90

.79   .82   .84

.74

.87

.87

.90

.89

.48

.65

.79

.55

.74

.82

.71

.65

.48

.87

.44

.89

.71

.74

.79

.91

$\dfrac{z}{b'}$

Vector scale: 0°   2°

1.4
1.2
1.0
.8
.6
.4
.2
0
-.2
-.4
-.6
-.8
-1.0
-1.2

0   .2   .4   .6   .8   1.0   1.2

$\dfrac{y}{b'}$

(e) $\alpha = 16.85°$

Figure 21.- Concluded.

Dashed lines correspond to constant values of $\frac{H_3}{H_{o_3}}$, as quoted.
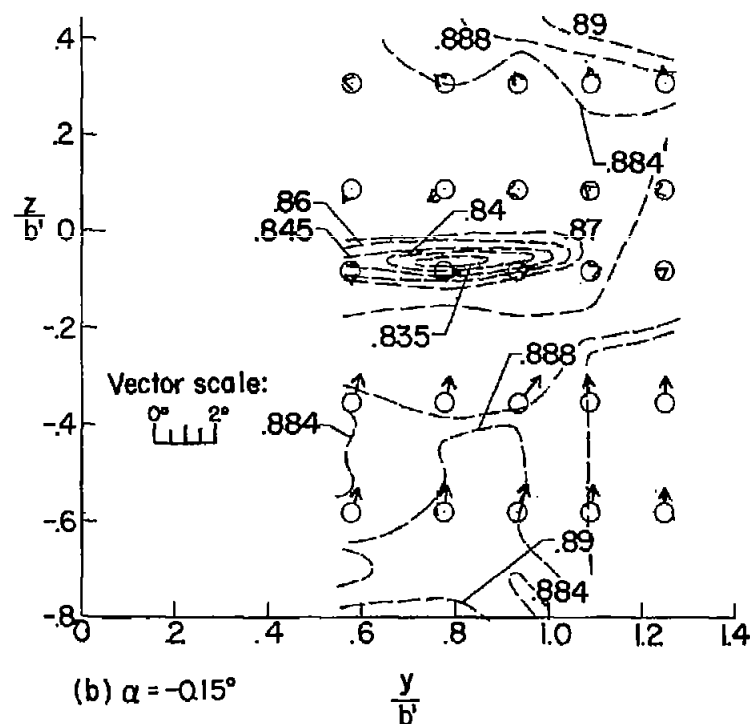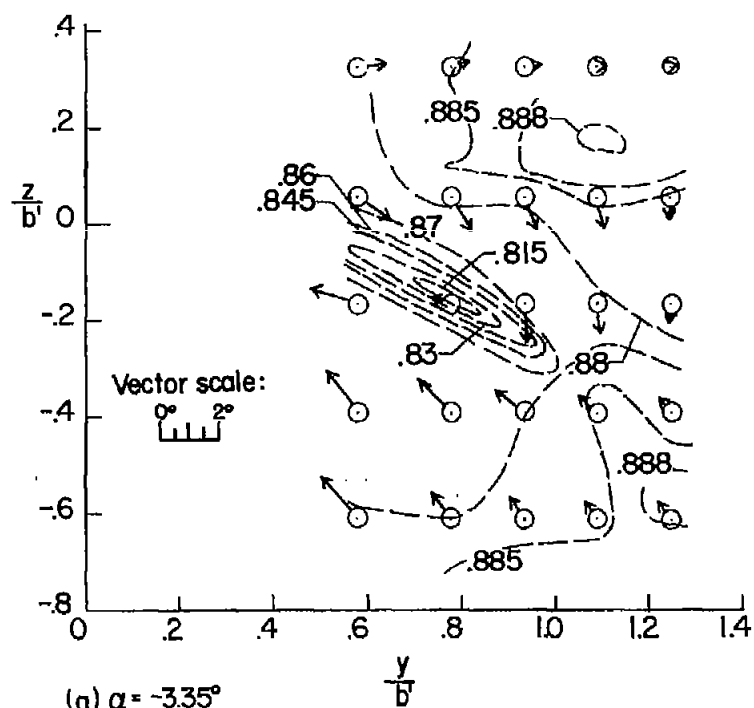
$\frac{H_3}{H_{o_3}}$ (Free stream) = .888

(a) $\alpha = 8.95°$

(b) $\alpha = 16.85°$

Figure 22.- Pressure contours and vector representation of the flow behind a triangular wing. $\Lambda = 72°$; $M = 1.62$; $x = 1.5c_r$; $R = 0.71 \times 10^6$.

Dashed lines correspond to constant values of $\frac{H_3}{H_{o_3}}$, as quoted.

$\frac{H_3}{H_{o_3}}$ (Free stream) = .888

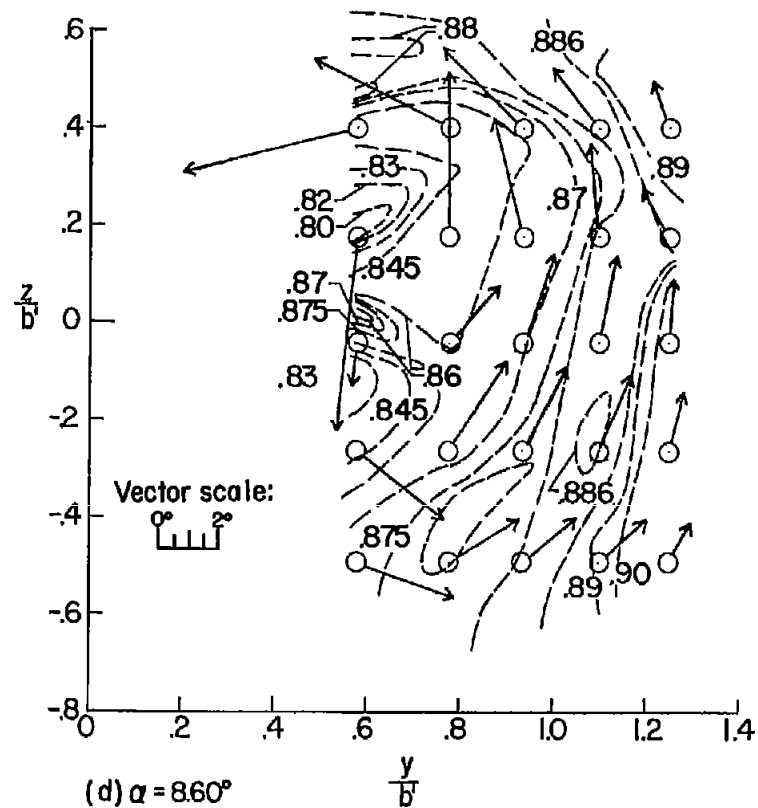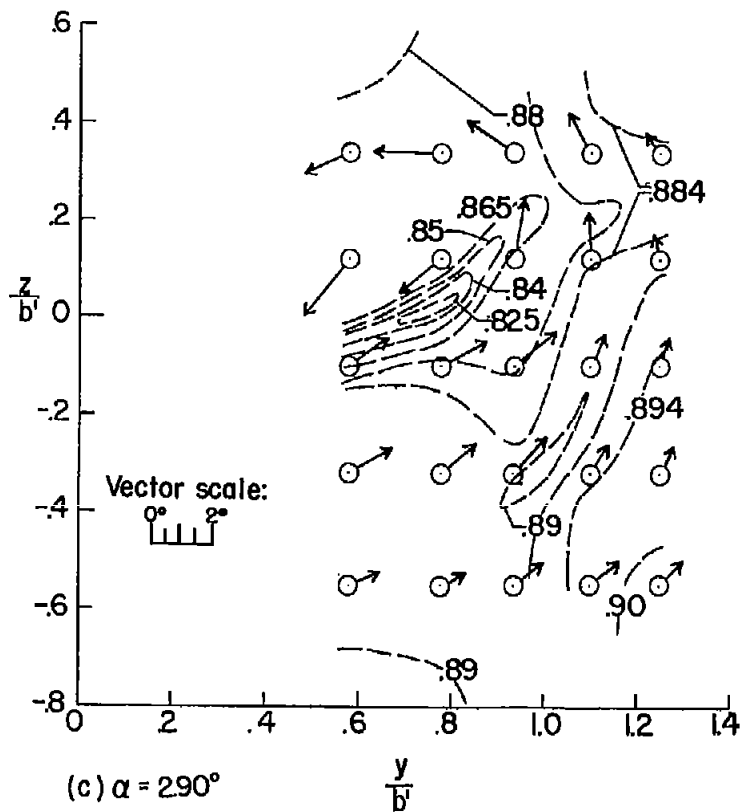(a) $\alpha = 8.90°$

(b) $\alpha = 16.80°$

Figure 23.- Pressure contours and vector representation of the flow behind a triangular wing. $\Lambda = 72°$; $M = 1.62$; $x = 3c_r$; $R = 1.42 \times 10^6$.

Figure 24.- Pressure contours and vector representation of the flow behind a triangular wing. $\Lambda = 72°$; $M = 1.62$; $x = 3c_r$; $R = 0.71 \times 10^6$.

Dashed lines correspond to constant values of $\frac{H_3}{H_{o_3}}$, as quoted.

$\frac{H_3}{H_{o_3}}$ (Free stream) = .888

(a) $\alpha = -2.90°$

(b) $\alpha = -0.30°$

Figure 25.- Pressure contours and vector representation of the flow behind a triangular wing. $\Lambda = 72°$; $M = 1.62$; $x = 4c_r$; $R = 1.42 \times 10^6$.

Dashed lines correspond to constant values of $\frac{H_3}{H_{o_3}}$, as quoted.
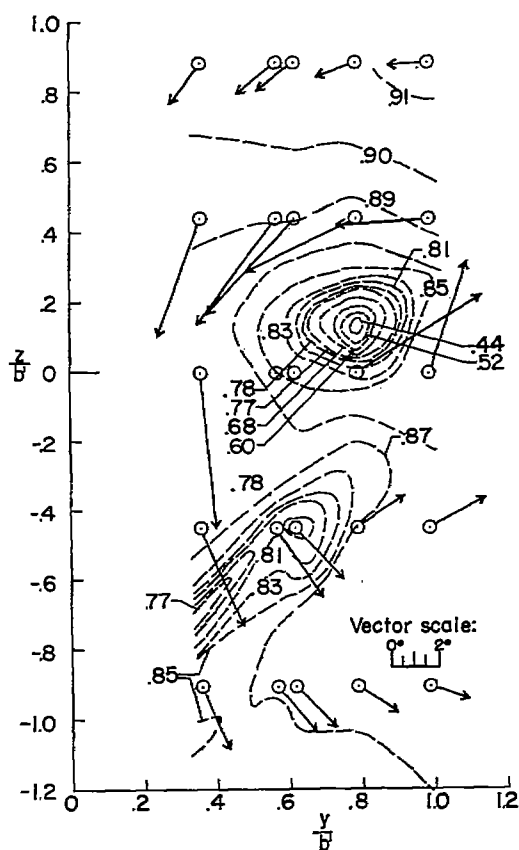
$\frac{H_3}{H_{o_3}}$ (Free stream) = .888

(c) $\alpha = 3.10°$

Figure 25.- Concluded.
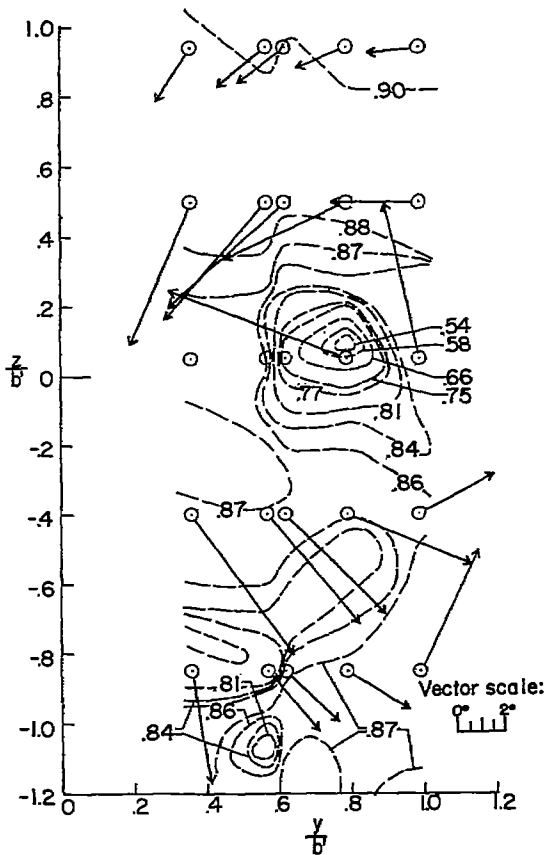
Dashed lines correspond to constant values of $\frac{H_3}{H_{o_3}}$, as quoted.

$\frac{H_3}{H_{o_3}}$ (Free stream) = .888

(a) $\alpha = 9.00°$

Figure 26.- Pressure contours and vector representation of the flow behind a triangular wing. $\Lambda = 72°$; $M = 1.62$; $x = 4c_r$; $R = 0.71 \times 10^6$.

Dashed lines correspond to constant values of $\frac{H_3}{H_{o_3}}$, as quoted.

$\frac{H_3}{H_{o_3}}$ (Free stream) = .888

(b) $\alpha = 1690°$

Figure 26.- Concluded.

Dashed lines correspond to constant values of $\frac{H_3}{H_{o_3}}$, as quoted.

$\frac{H_3}{H_{o_3}}$ (Free stream) = .888

(a) $\alpha = -3.30°$

(b) $\alpha = -0.45°$

Figure 27.- Pressure contours and vector representation of the flow behind a reversed triangular wing. $\Lambda_{TE} = -50°$; $M = 1.62$; $x = 1.5c_r$; $R = 1.42 \times 10^6$.

Dashed lines correspond to constant values of $\frac{H_3}{H_{o_3}}$, as quoted.

$\frac{H_3}{H_{o_3}}$ (Free stream) = .888

(c) $\alpha = 2.70°$

(d) $\alpha = 8.60°$

Figure 27.— Concluded.

Dashed lines correspond to constant values of $\frac{H_3}{H_{o_3}}$, as quoted.

$\frac{H_3}{H_{o_3}}$ (Free stream) = .888

(a) $\alpha = -3.50°$

(b) $\alpha = -0.45°$

Figure 28.– Pressure contours and vector representation of the flow behind a reversed triangular wing. $\Lambda_{TE} = -50°$; $M = 1.62$; $x = 3c_r$; $R = 1.42 \times 10^6$.

Dashed lines correspond to constant values of $\frac{H_3}{H_{o_3}}$, as quoted.
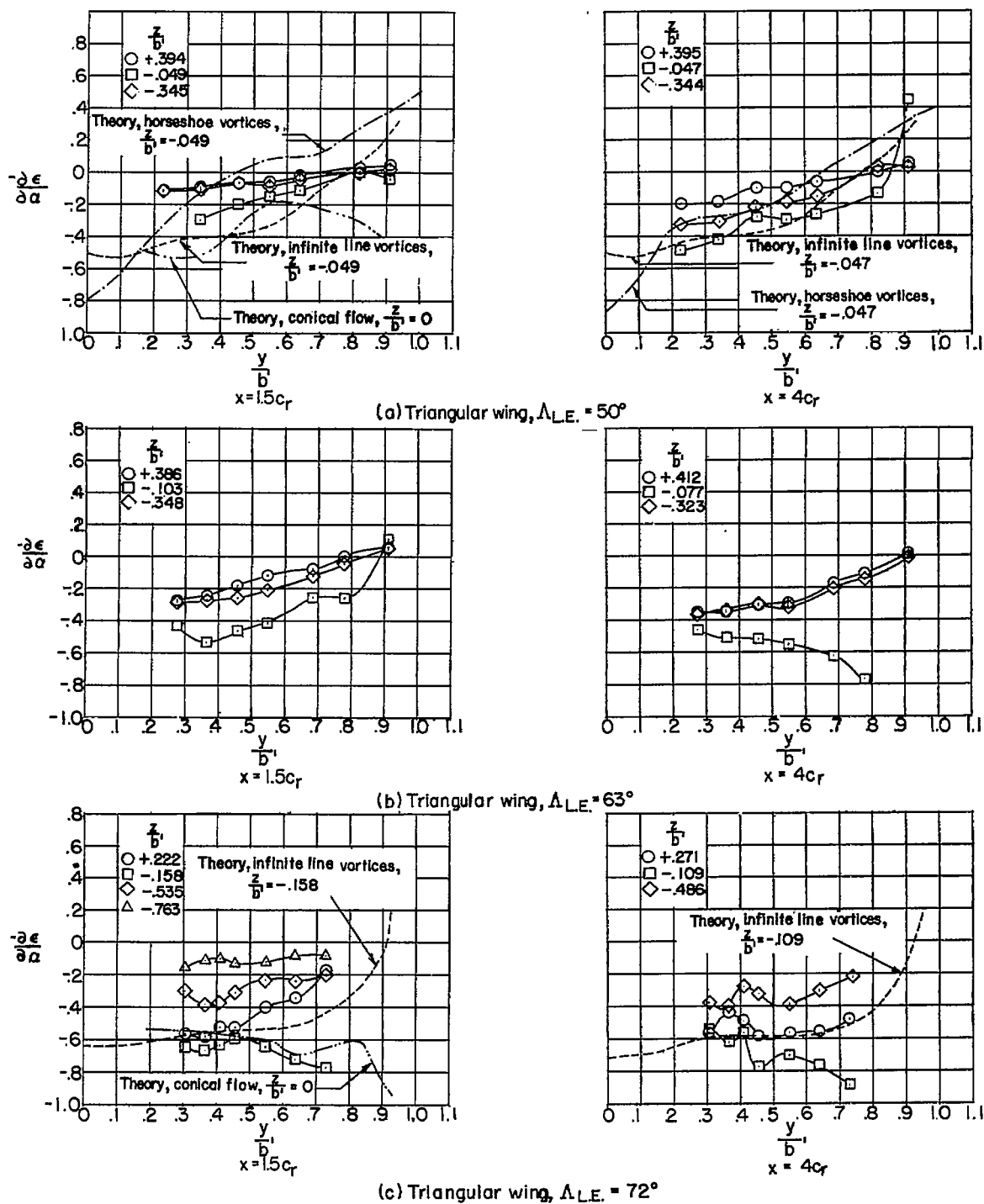
$\frac{H_3}{H_{o_3}}$ (Free stream) = .888

(c) $\alpha = 2.70°$

(d) $\alpha = 8.55°$

Figure 28.- Concluded.

Dashed lines correspond to constant values of $\frac{H_3}{H_{03}}$, as quoted.

$\frac{H_3}{H_{03}}$ (Free stream) = .888

(a) $\alpha = -3.35°$

(b) $\alpha = -0.15°$

Figure 29.— Pressure contours and vector representation of the flow behind a reversed triangular wing. $\Lambda_{TE} = -50°$; $M = 1.62$; $x = 4c_r$; $R = 1.42 \times 10^6$.

Dashed lines correspond to constant values of $\frac{H_3}{H_{o_3}}$, as quoted.

$$\frac{H_3}{H_{o_3}} \text{ (Free stream)} = .888$$

(c) $\alpha = 2.90°$

(d) $\alpha = 8.60°$

Figure 29.- Concluded.
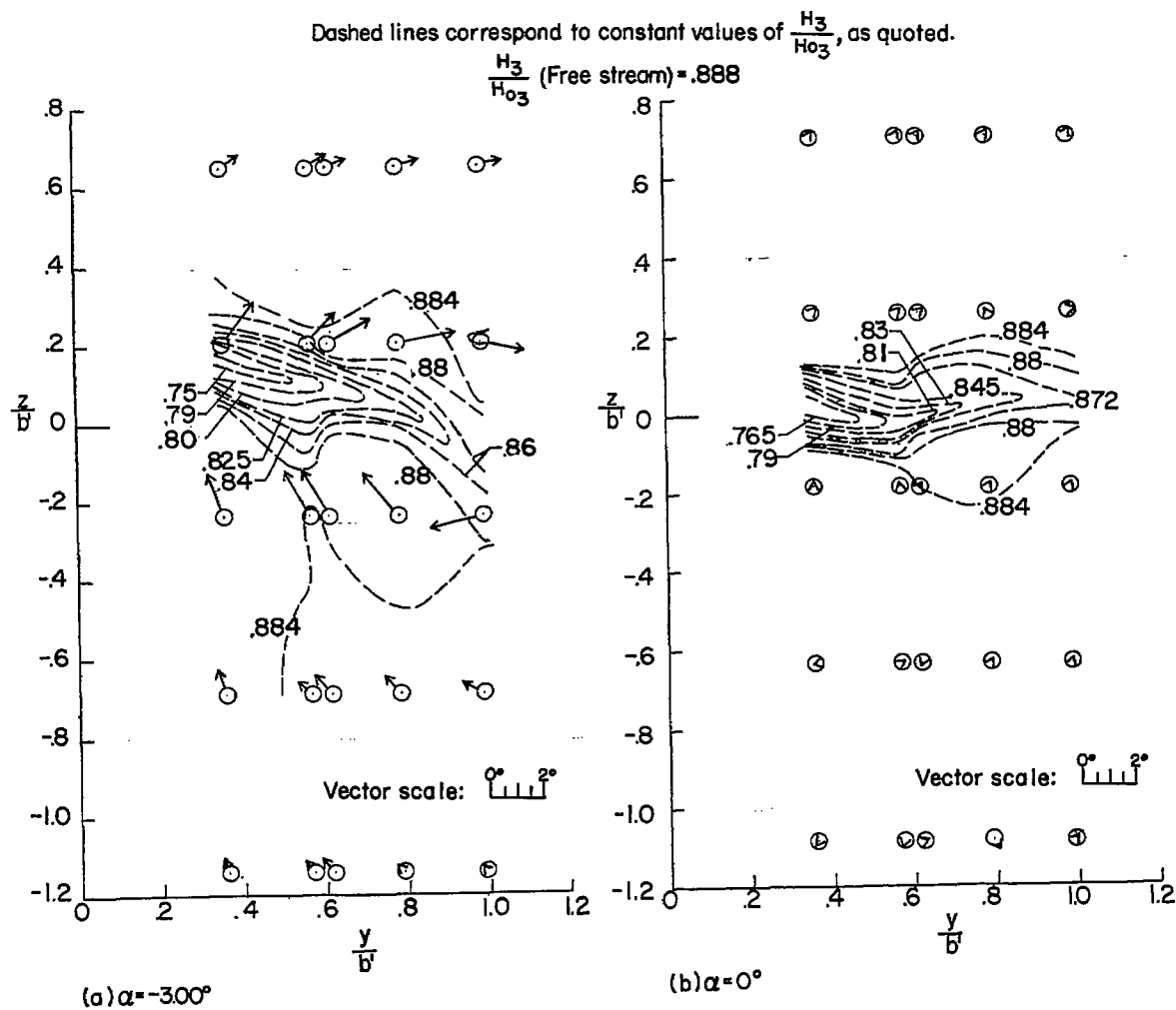
Figure 30.- Pressure contours and vector representation of the flow behind a straight 0-taper-ratio wing. $\Lambda = -\Lambda_{TE} = 50°$; $M = 1.62$; $x = 1.5c_r$; $R = 1.42 \times 10^6$.

Dashed lines correspond to constant values of $\frac{H_3}{H_{O_3}}$, as quoted.

$\frac{H_3}{H_{O_3}}$ (Free stream) = .888

.8

.6

.4

.884

.87 .855
.84
.82
.77 .87

-.2

.78
.79
.884

-.6

Vector scale: 0° 2°

(c) $\alpha = 3.00°$

.8

.6

.88
.87
.86 .80
.77
.72
.68
.62
.84
.83
.86
.80 .87
.77
.88
.89
.90
.92

Vector scale: 0° 2°

(d) $\alpha = 8.90°$
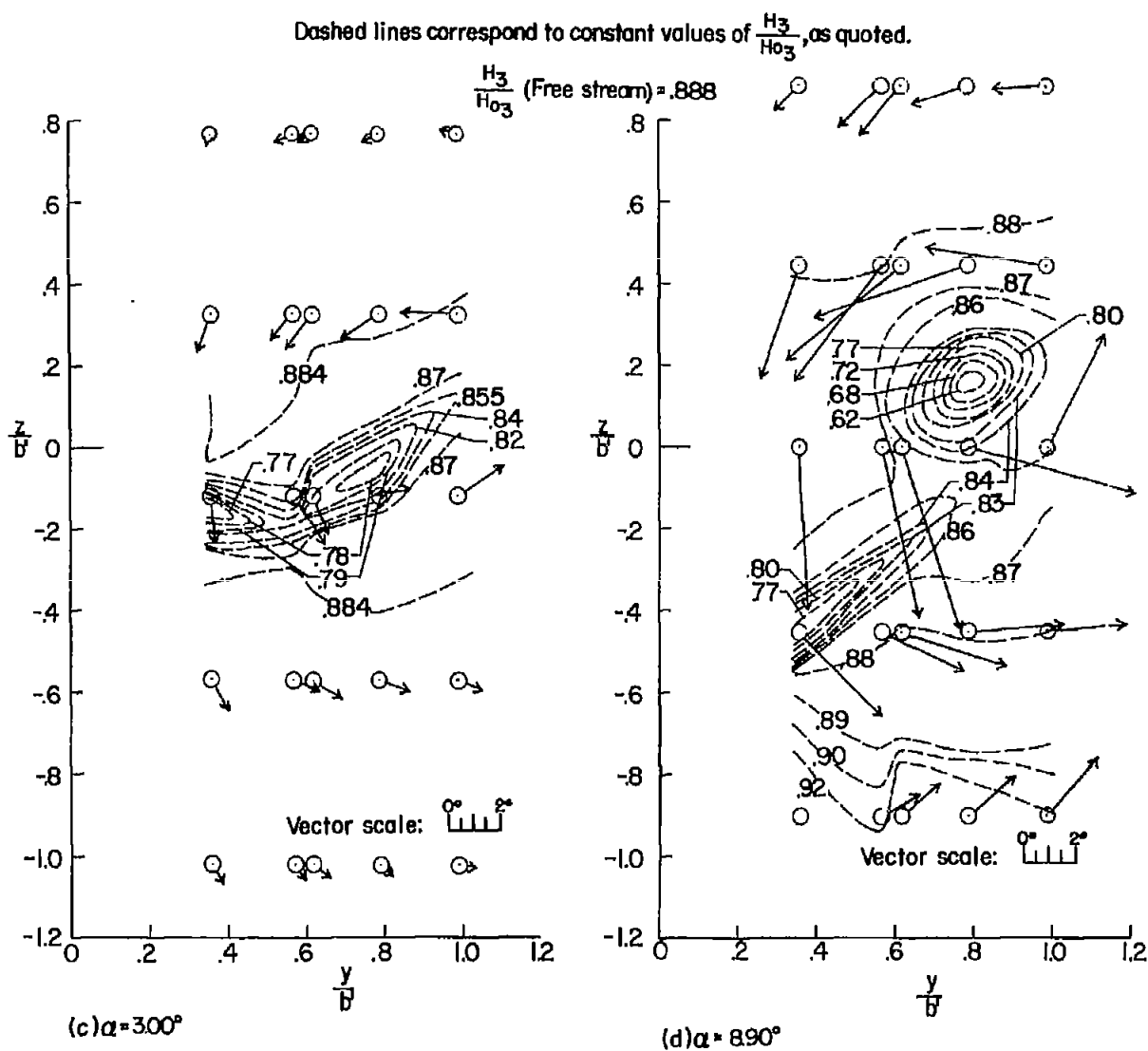
Figure 30.— Continued.

Dashed lines correspond to constant values of $\frac{H_3}{H_{03}}$, as quoted.

$\frac{H_3}{H_{03}}$ (Free stream) = .888
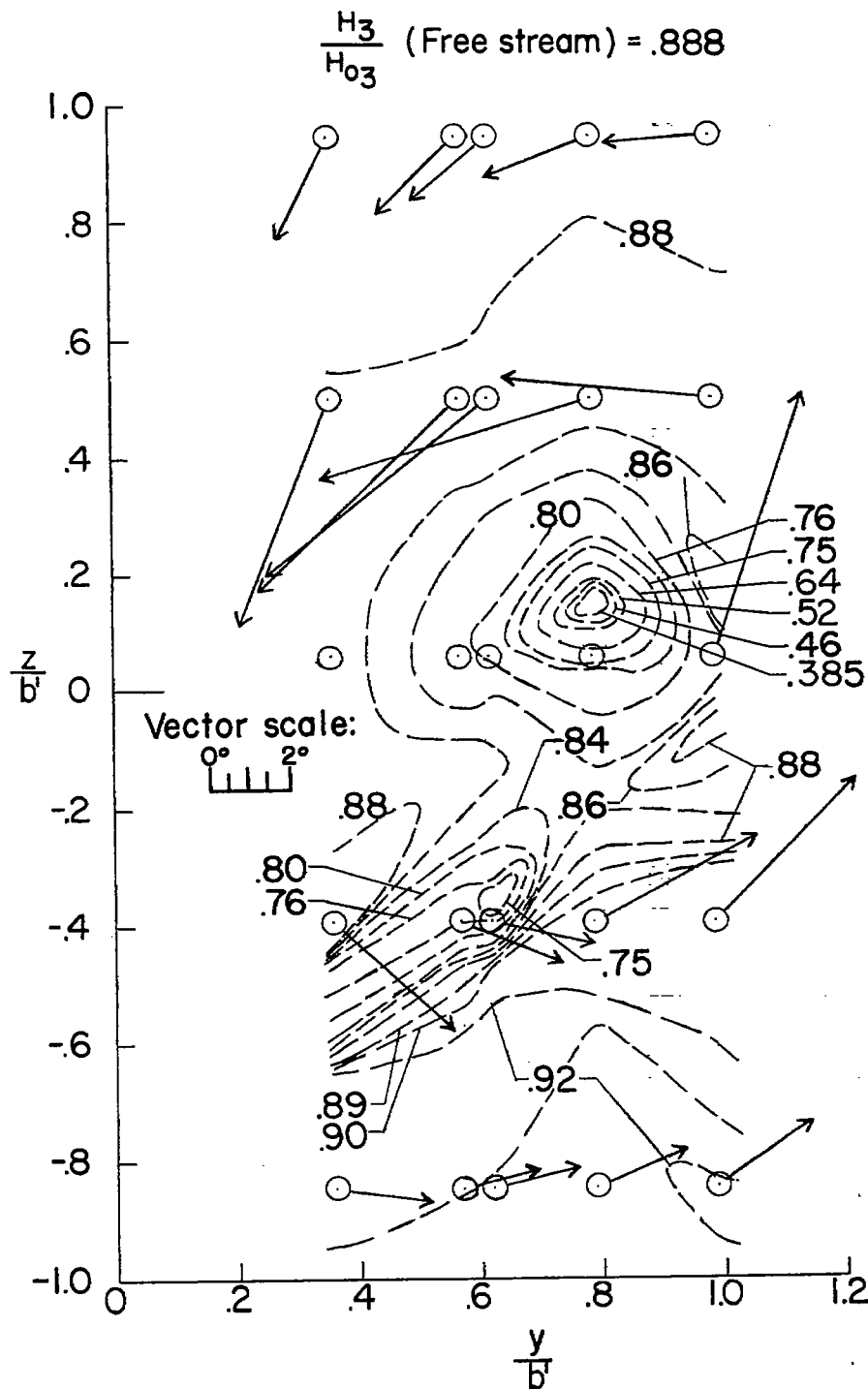
(e) α = 11.90°

Figure 30.- Concluded

Dashed lines correspond to constant values of $\frac{H_3}{H_{o_3}}$, as quoted.

$\frac{H_3}{H_{o_3}}$ (Free stream) = .888

(a) $\alpha = 8.60°$ (b) $\alpha = 11.90°$

Figure 31.- Pressure contours and vector representation of the flow behind a straight 0-taper-ratio wing. $\Lambda = -\Lambda_{TE} = 50°$; $M = 1.62$; $x = 3c_r$; $R = 1.42 \times 10^6$.

Dashed lines correspond to constant values of $\frac{H_3}{H_{o_3}}$, as quoted.

$\frac{H_3}{H_{o_3}}$ (Free stream) = .888

(a) $\alpha = -3.15°$

(b) $\alpha = -0.10°$
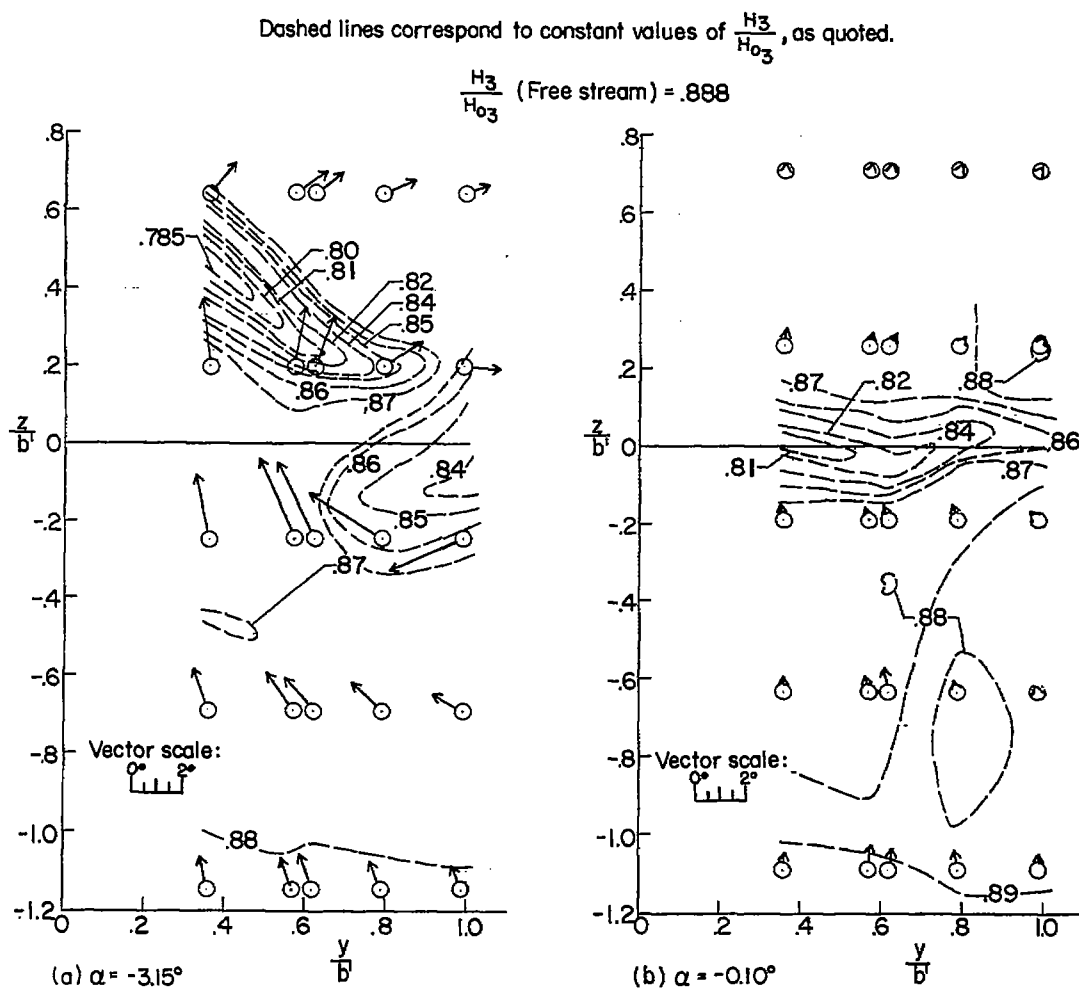
Figure 32.- Pressure contours and vector representation of the flow behind a straight O-taper-ratio wing. $\Lambda = -\Lambda_{TE} = 50°$; M = 1.62; $x = 4c_r$; R = 1.42×10^6.

Dashed lines correspond to constant values of $\frac{H_3}{H_{o_3}}$, as quoted.

$\frac{H_3}{H_{o_3}}$ (Free stream) = .888

(c) $\alpha = 2.90°$

(d) $\alpha = 8.75°$
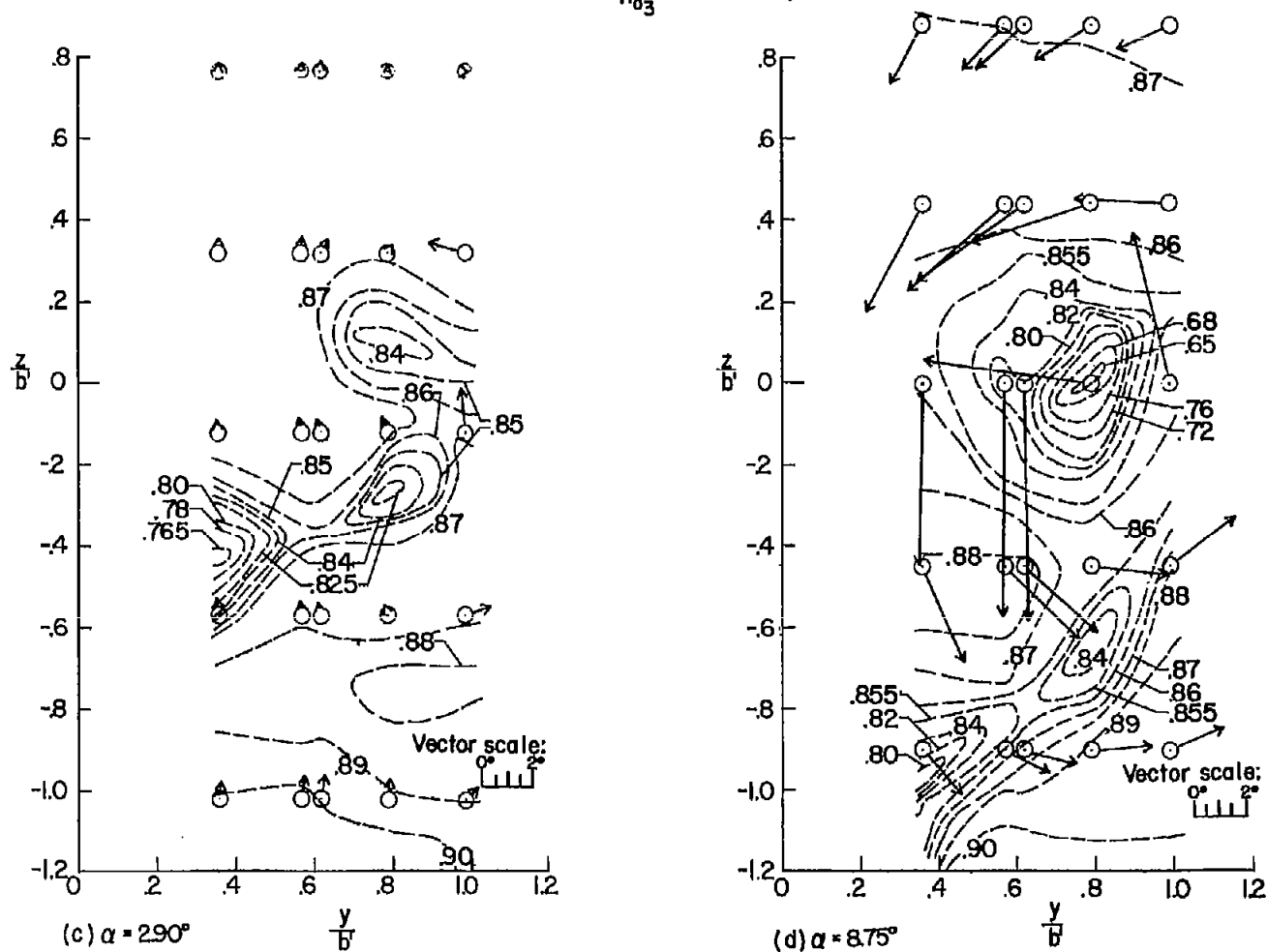
Figure 32.- Concluded.

(a) Triangular wing, $\Lambda_{L.E.} = 50°$

(b) Triangular wing, $\Lambda_{L.E.} = 63°$

(c) Triangular wing, $\Lambda_{L.E.} = 72°$

Figure 33.- Spanwise variation in $\dfrac{-\partial\epsilon}{\partial\alpha}$ near $\alpha = 0°$ ($\pm 3°$) for three triangular wings. $M = 2.41$; $R = 1.42 \times 10^6$.
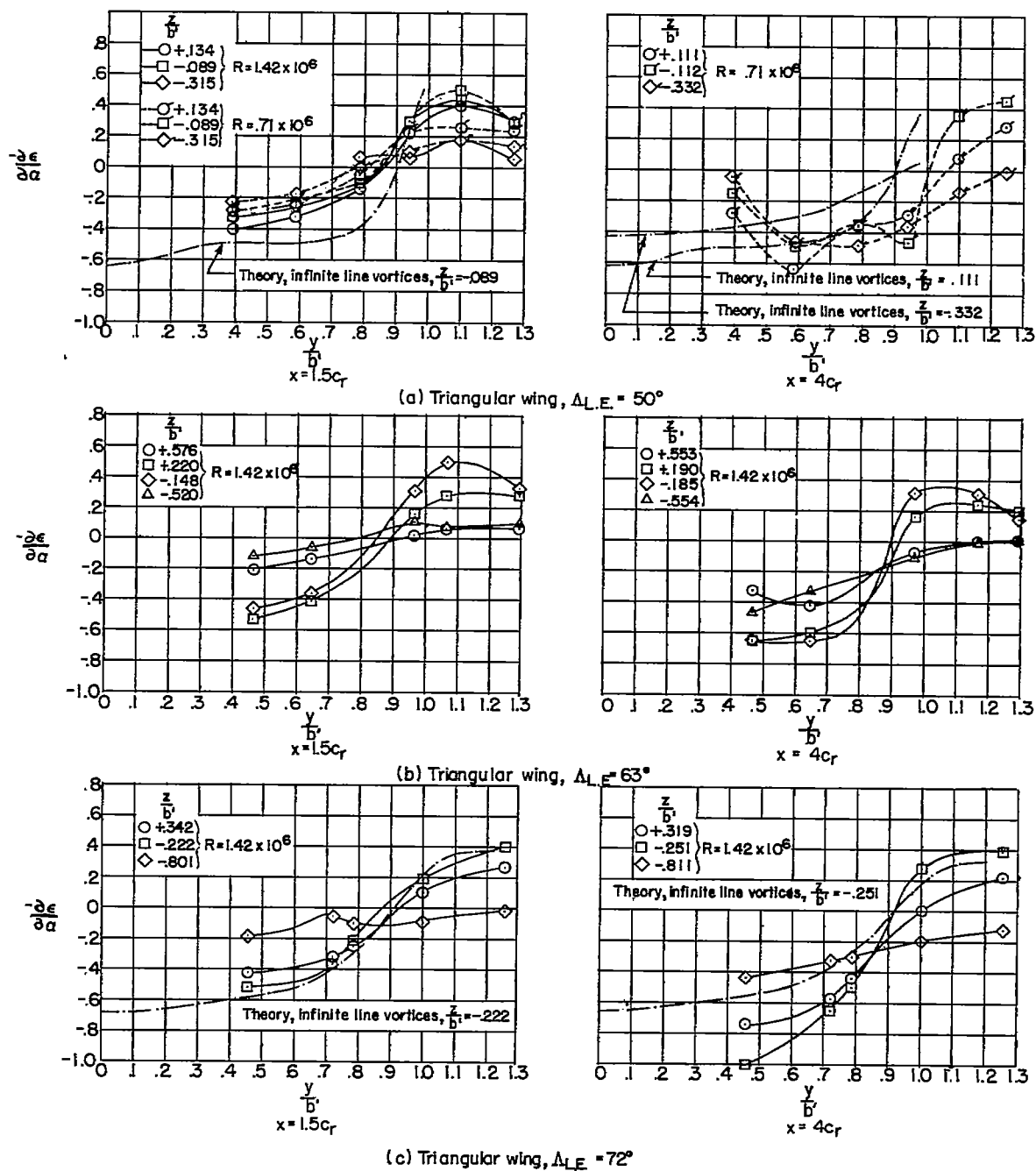
Figure 34.- Spanwise variation in $\dfrac{-\partial\epsilon}{\partial\alpha}$ near $\alpha = 0^{\circ}$ ($\pm 3^{\circ}$) for three triangular wings. $M = 1.62$; $R = 1.42 \times 10^{6}$.
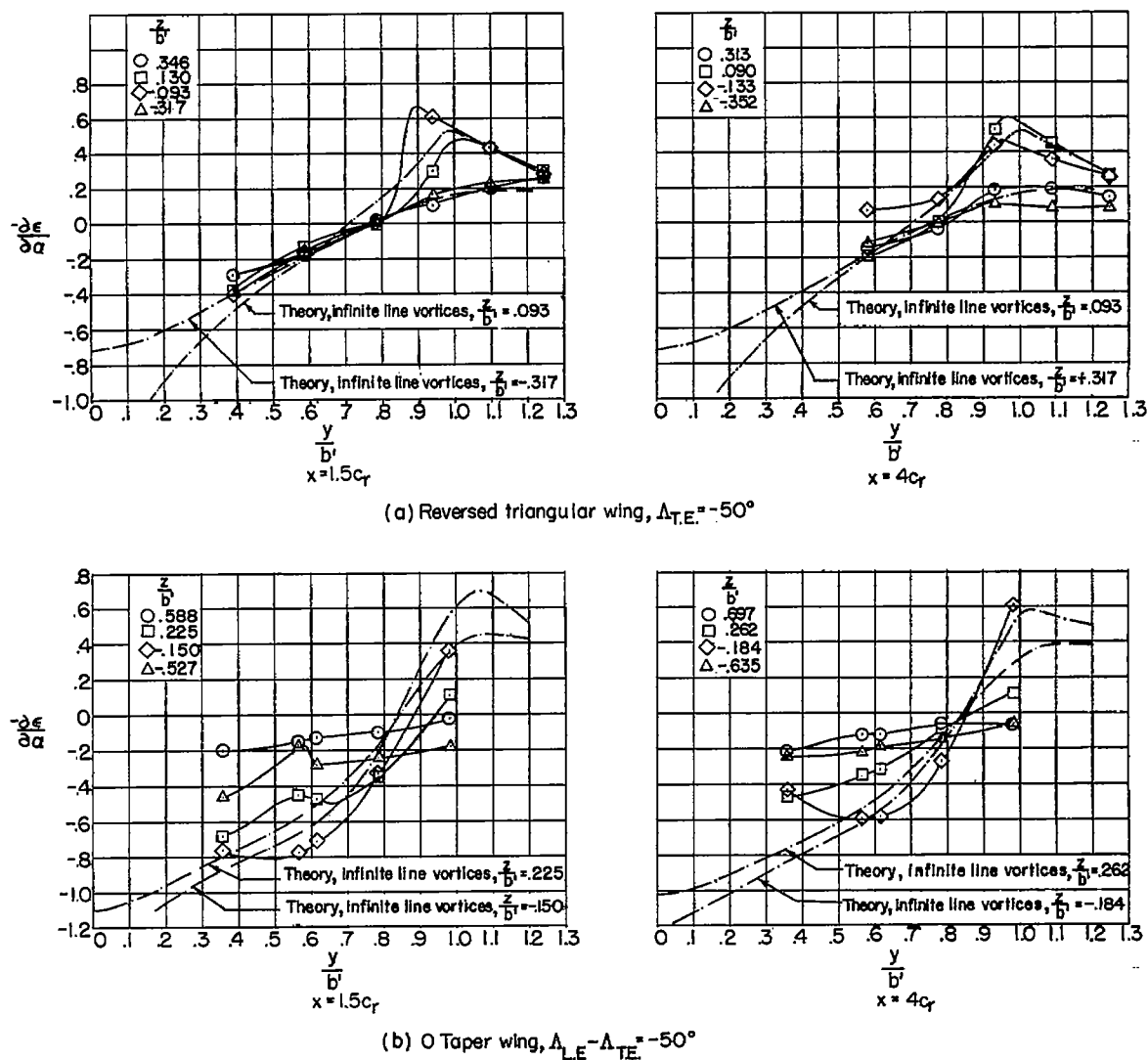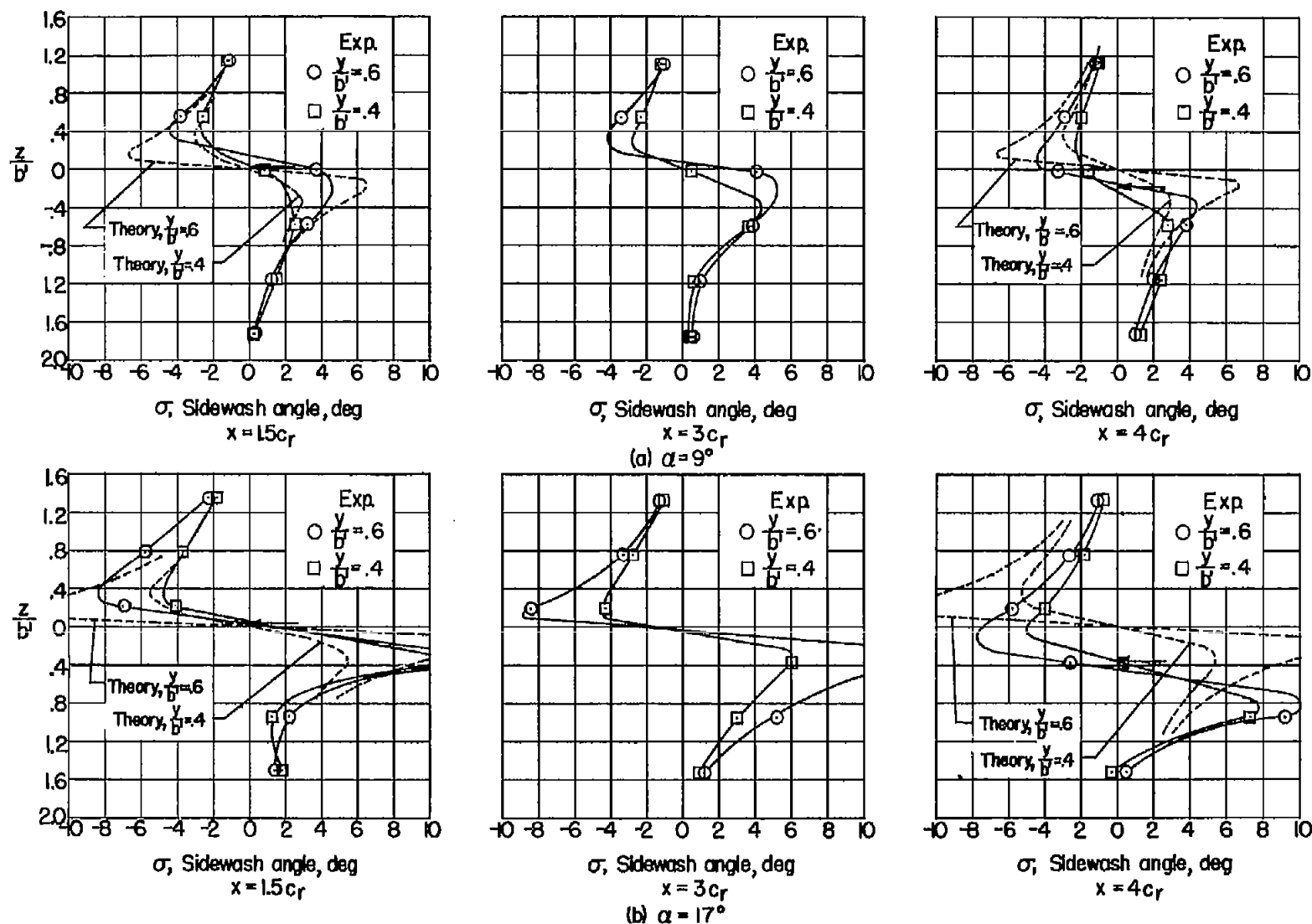
Figure 36.- Vertical variation of the sidewash at stations behind 72° sweptback triangular wing. M = 1.62; R = 0.71 × 10⁶.
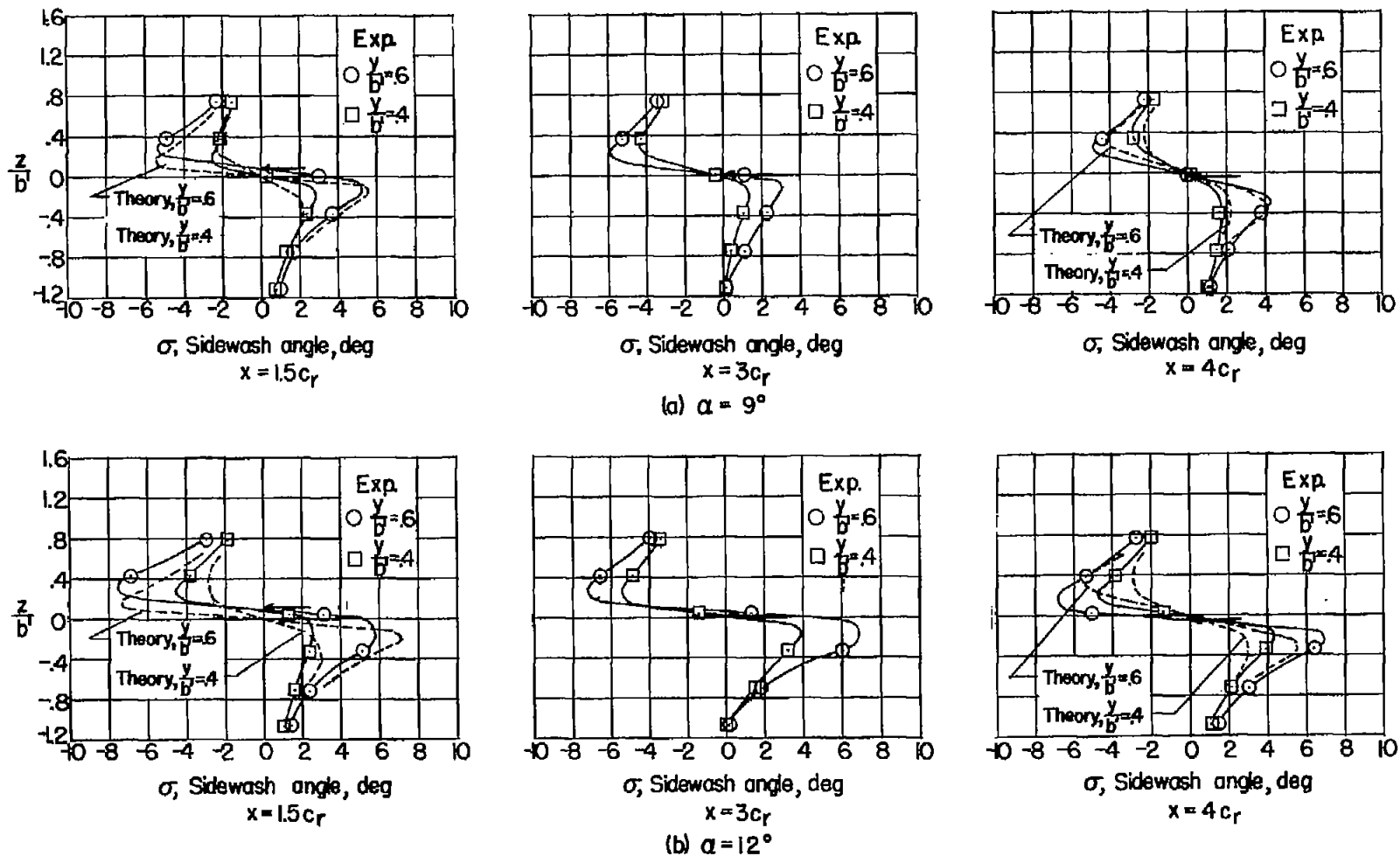
Figure 37.- Vertical variation of the sidewash at stations behind 63° sweptback triangular wing. M = 1.62; R = 1.42 × 10⁶.
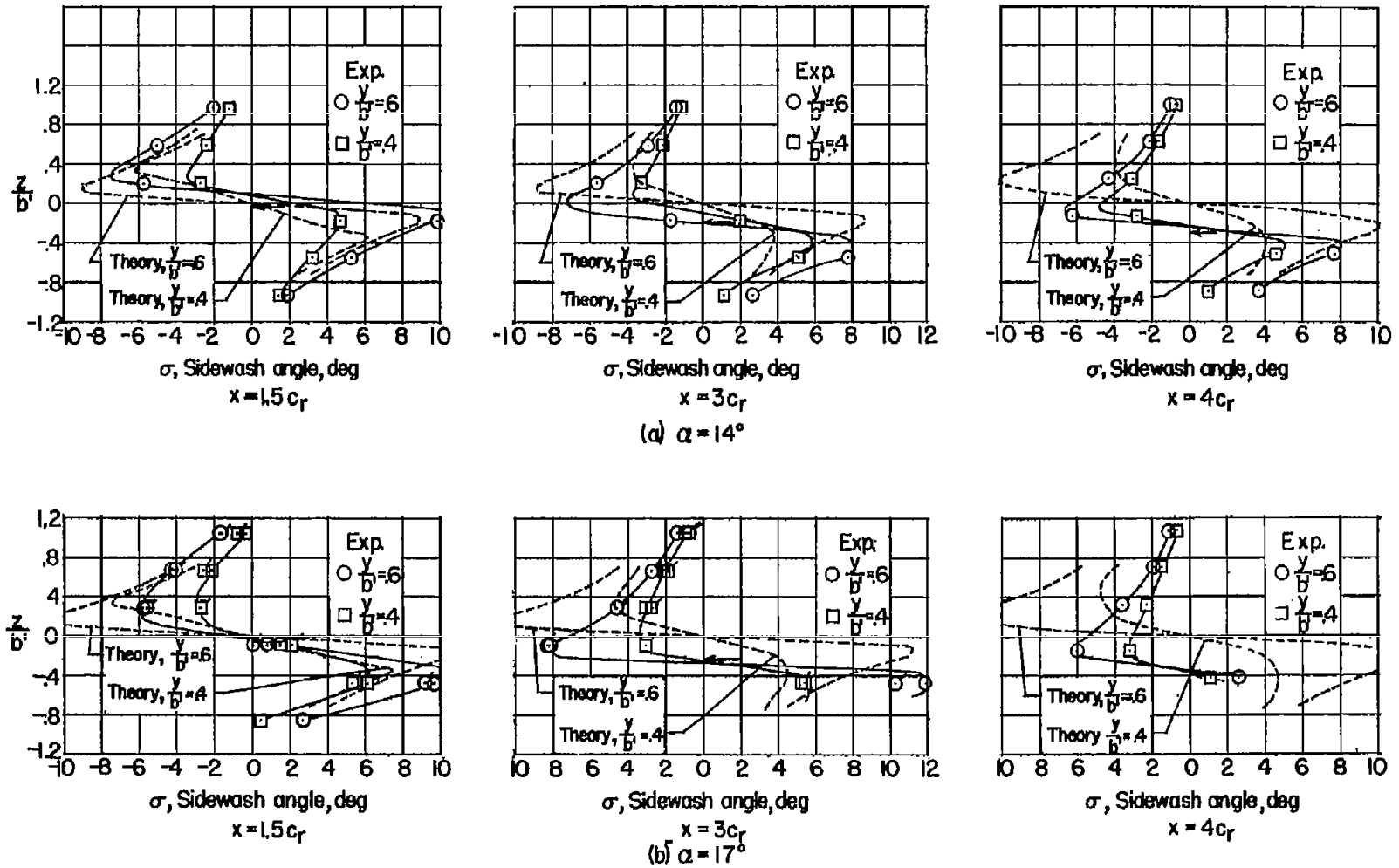
Figure 38.- Vertical variation of the sidewash at stations behind
72° sweptback triangular wing. $M = 2.41$; $R = 1.42 \times 10^6$. (Flagged
symbols denote $R = 0.71 \times 10^6$.)
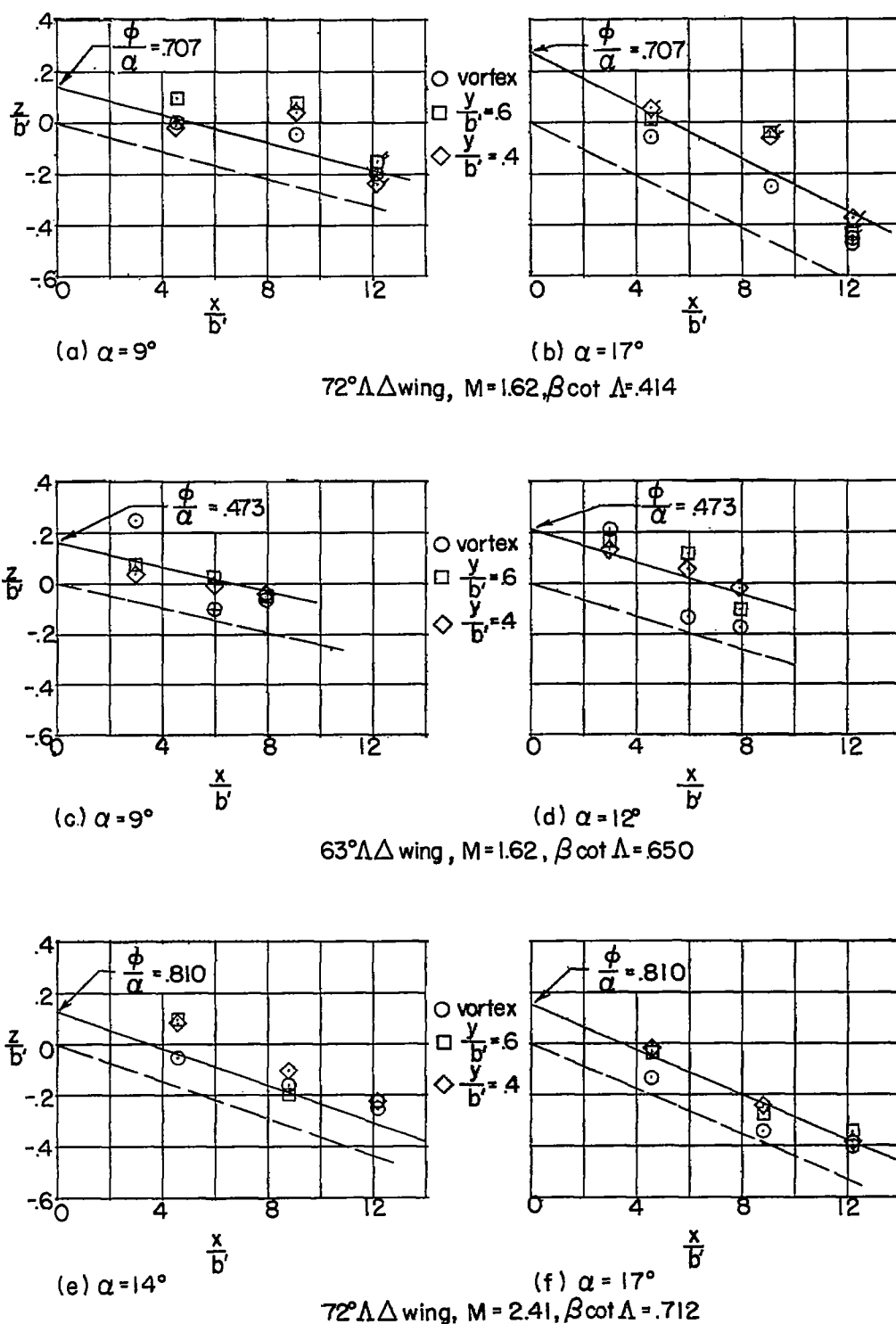
Figure 39.- Side view of the effective vortex-sheet locations for the three subsonic leading-edge, triangular-wing configurations.
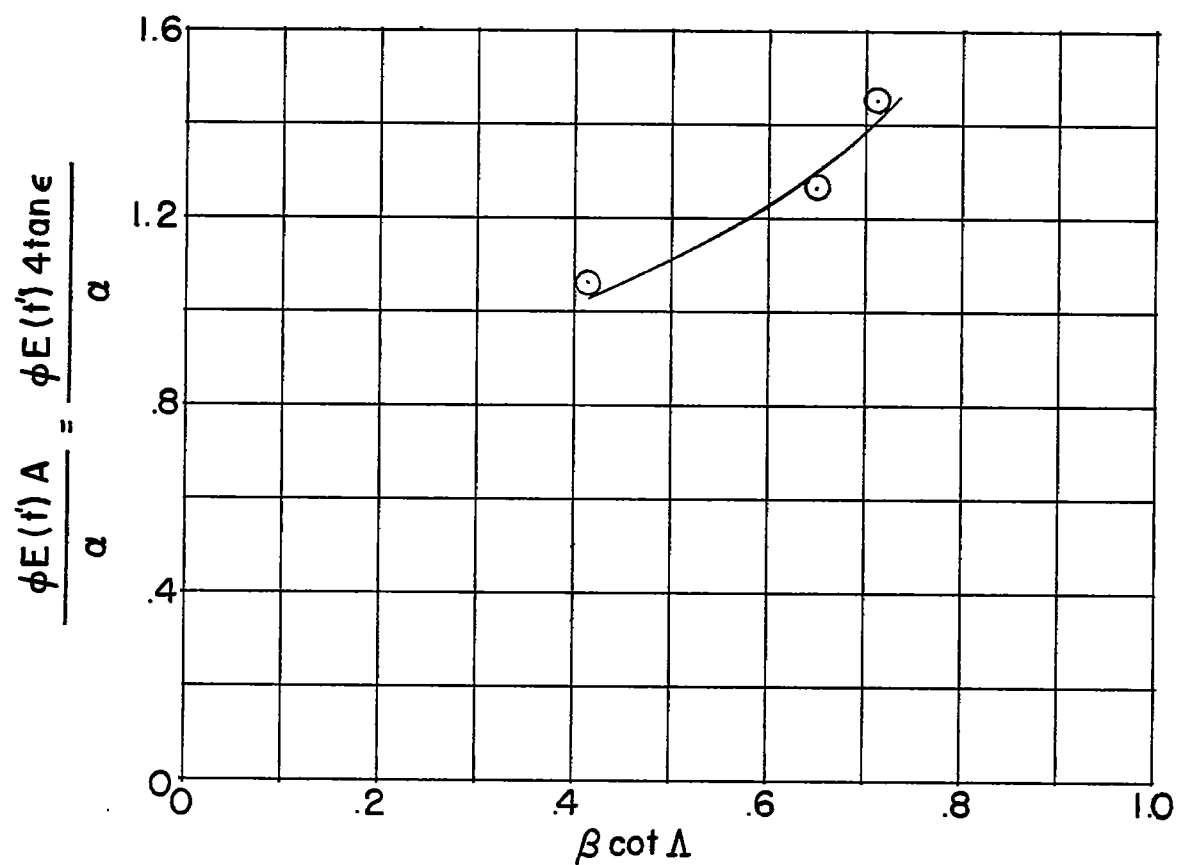
Figure 40.- Chart illustrating height of centroid of vorticity above the trailing edges of triangular wings with subsonic leading edges.
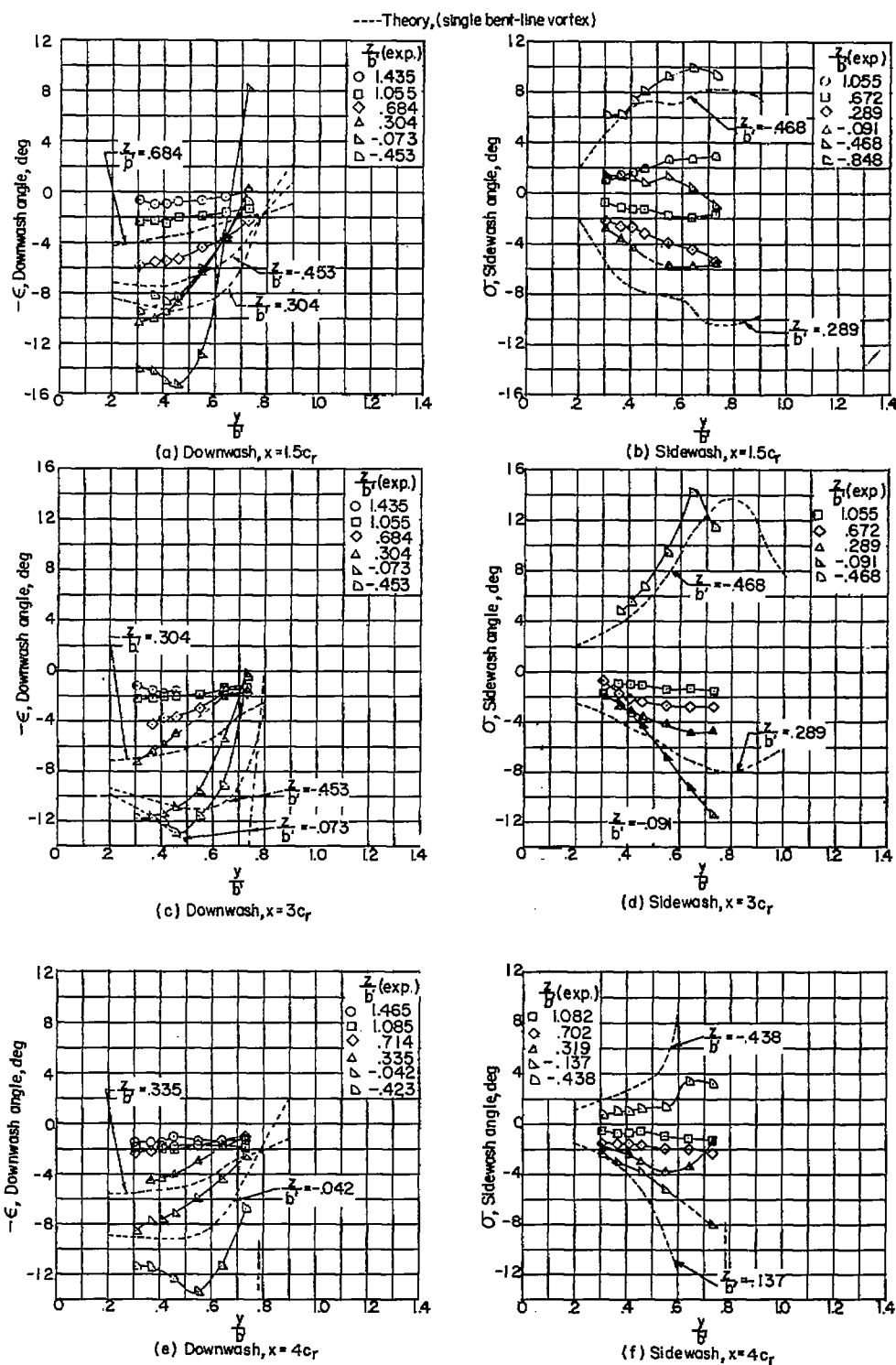
Figure 41.- Spanwise variation of downwash and sidewash for 72° sweptback triangular wing. M = 2.41; R = 1.42 × 10⁶; α = 17°.
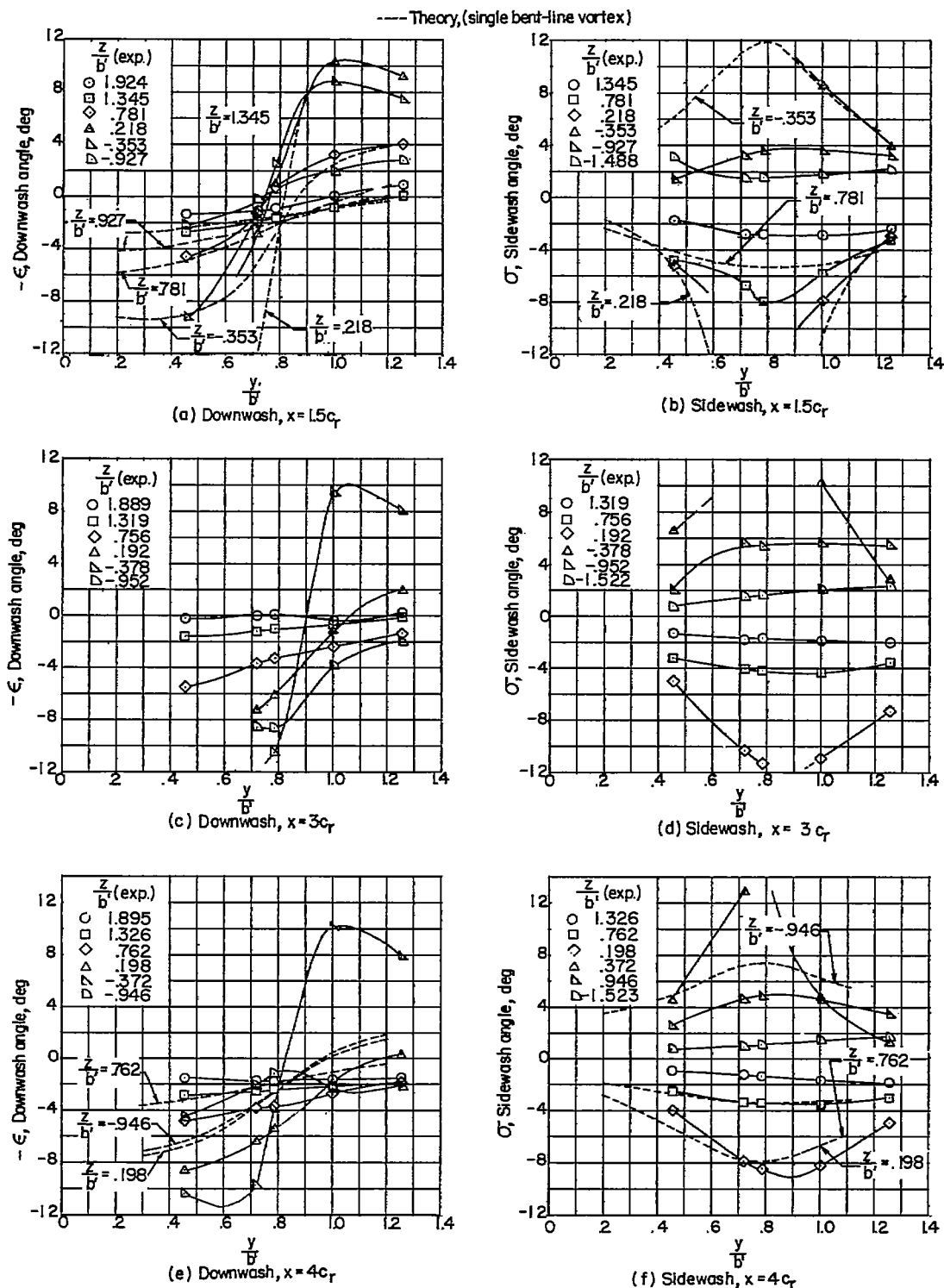
Figure 42.- Spanwise variation of downwash and sidewash for 72° sweptback triangular wing. M = 1.62; R = 1.42 × 10⁶; α = 17°.
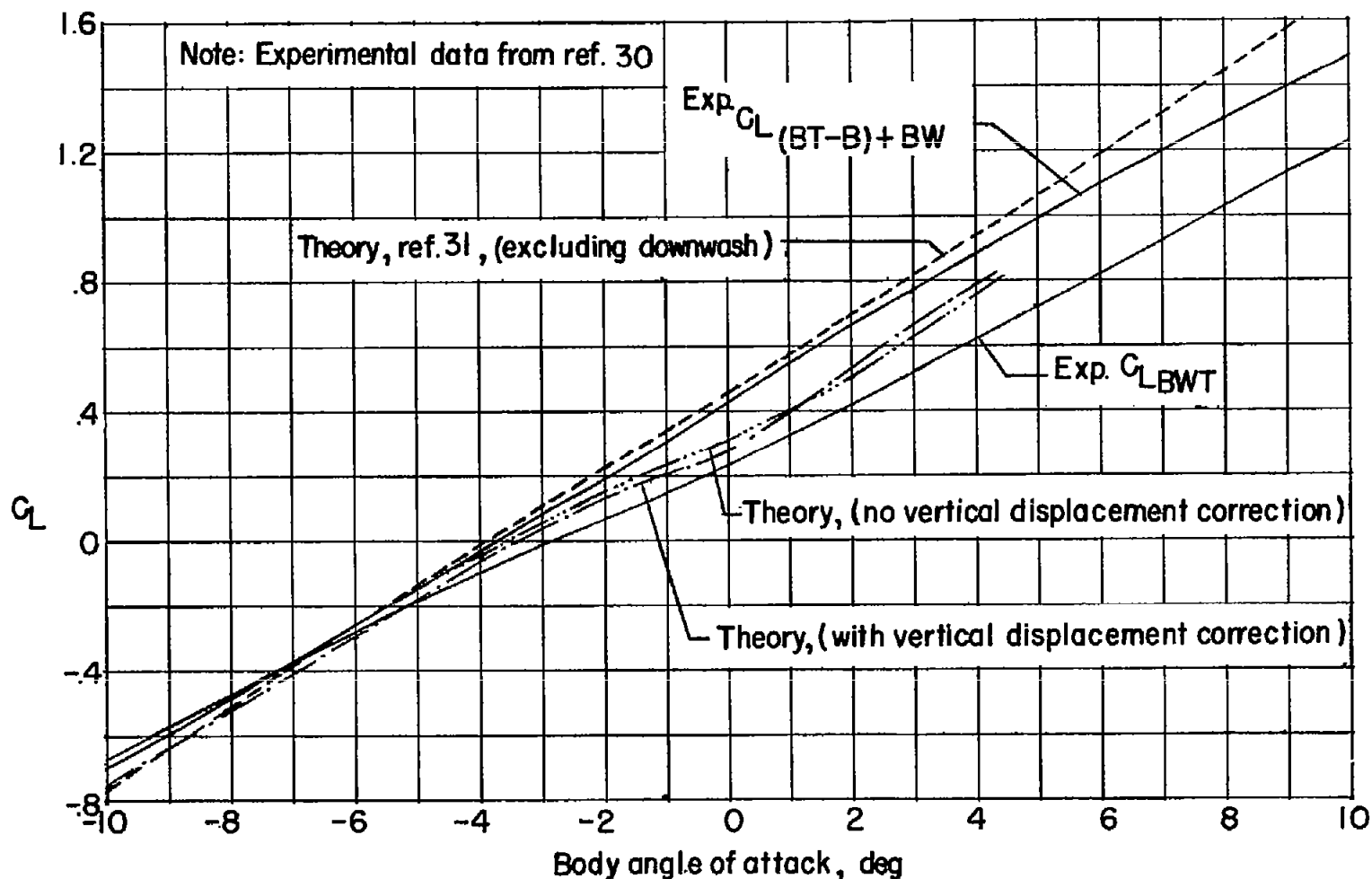
Figure 43.- Comparison of theoretical and experimental lift for a triangular wing and tail missile with the wing at 8° incidence, using theoretical downwash estimates. (Experimental data from ref. 30 at M = 1.50.)

(a) x = 1.5c_r

(b) x = 4c_r
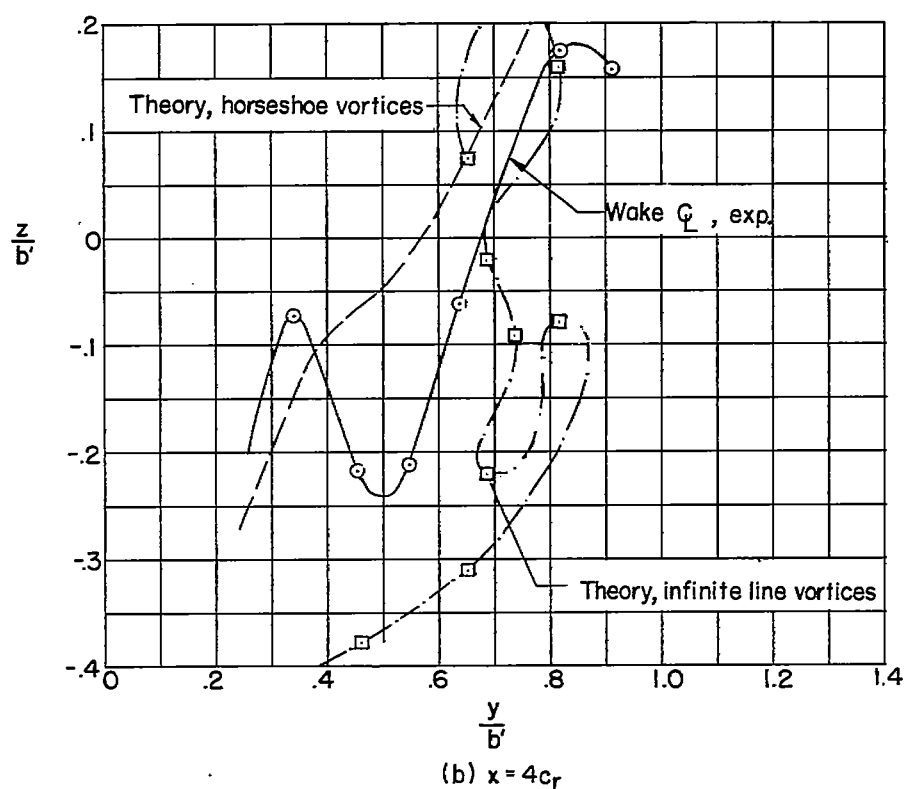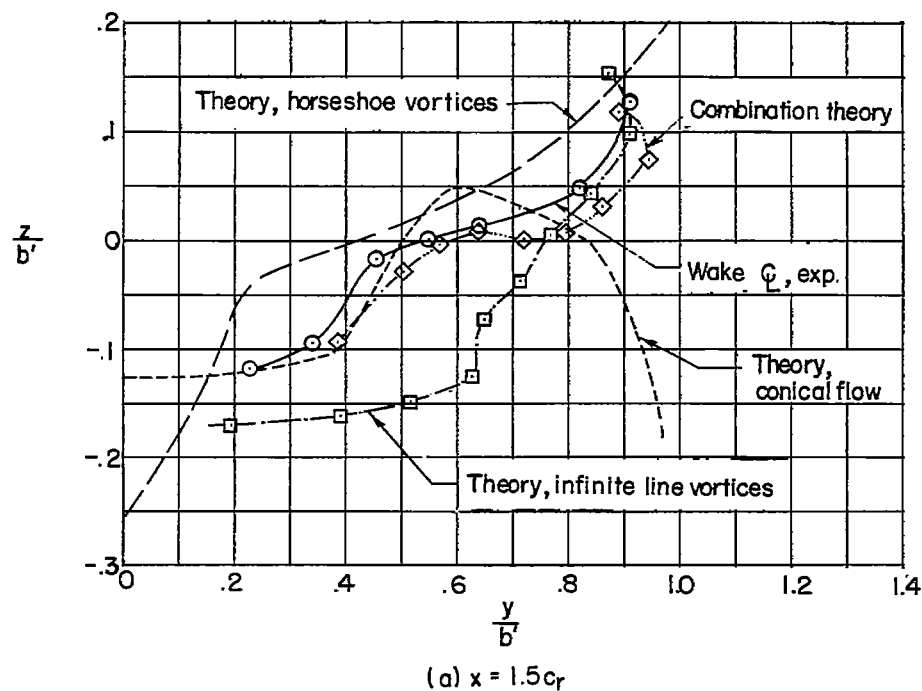
Figure 44.- Wake center-line location and comparison with various theories for the 50° sweptback triangular wing. M = 2.41.
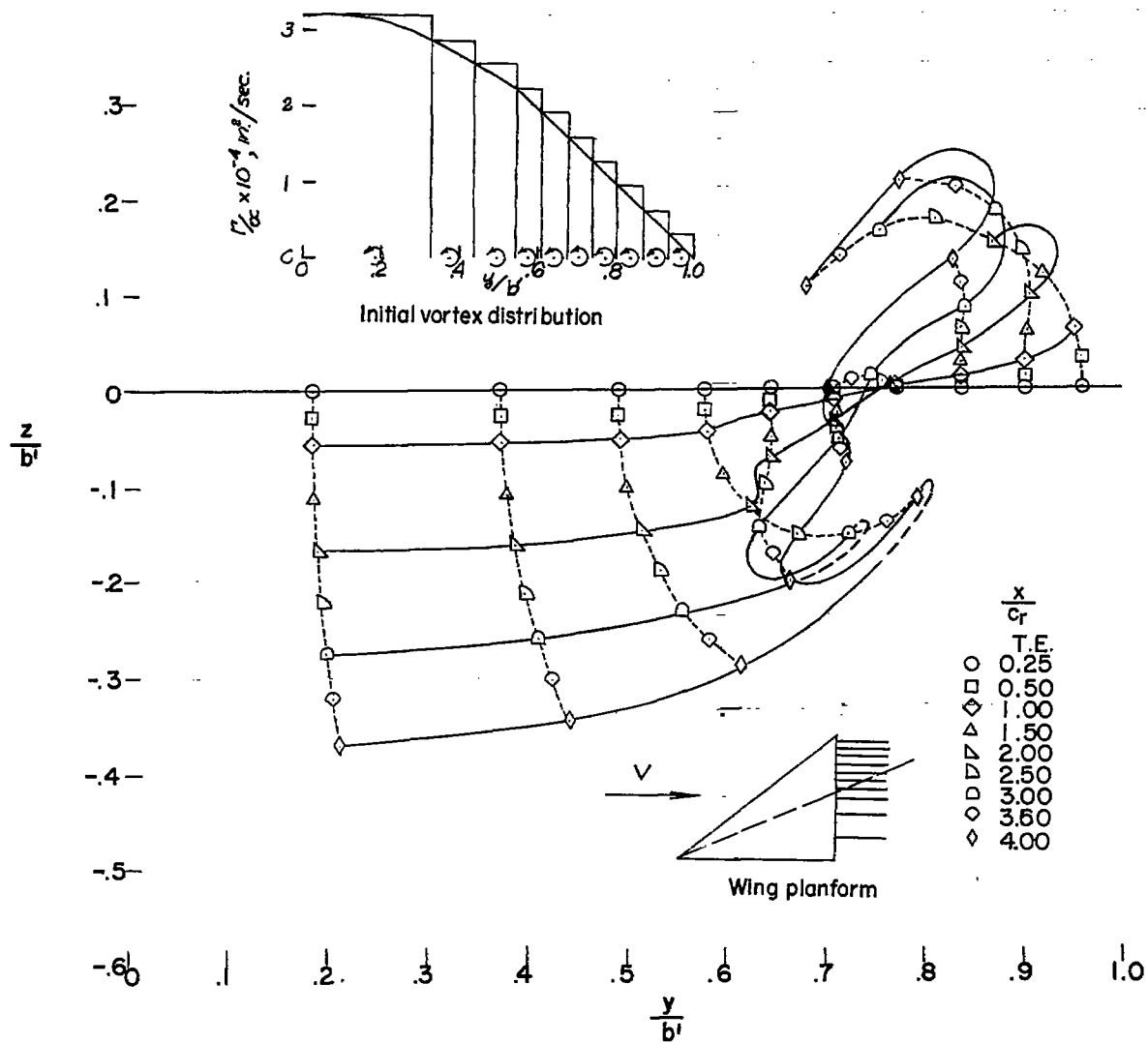
Figure 45.- Theoretical paths of ten infinite line vorticies behind the
50° sweptback triangular wing. M = 2.41; α = 12°.
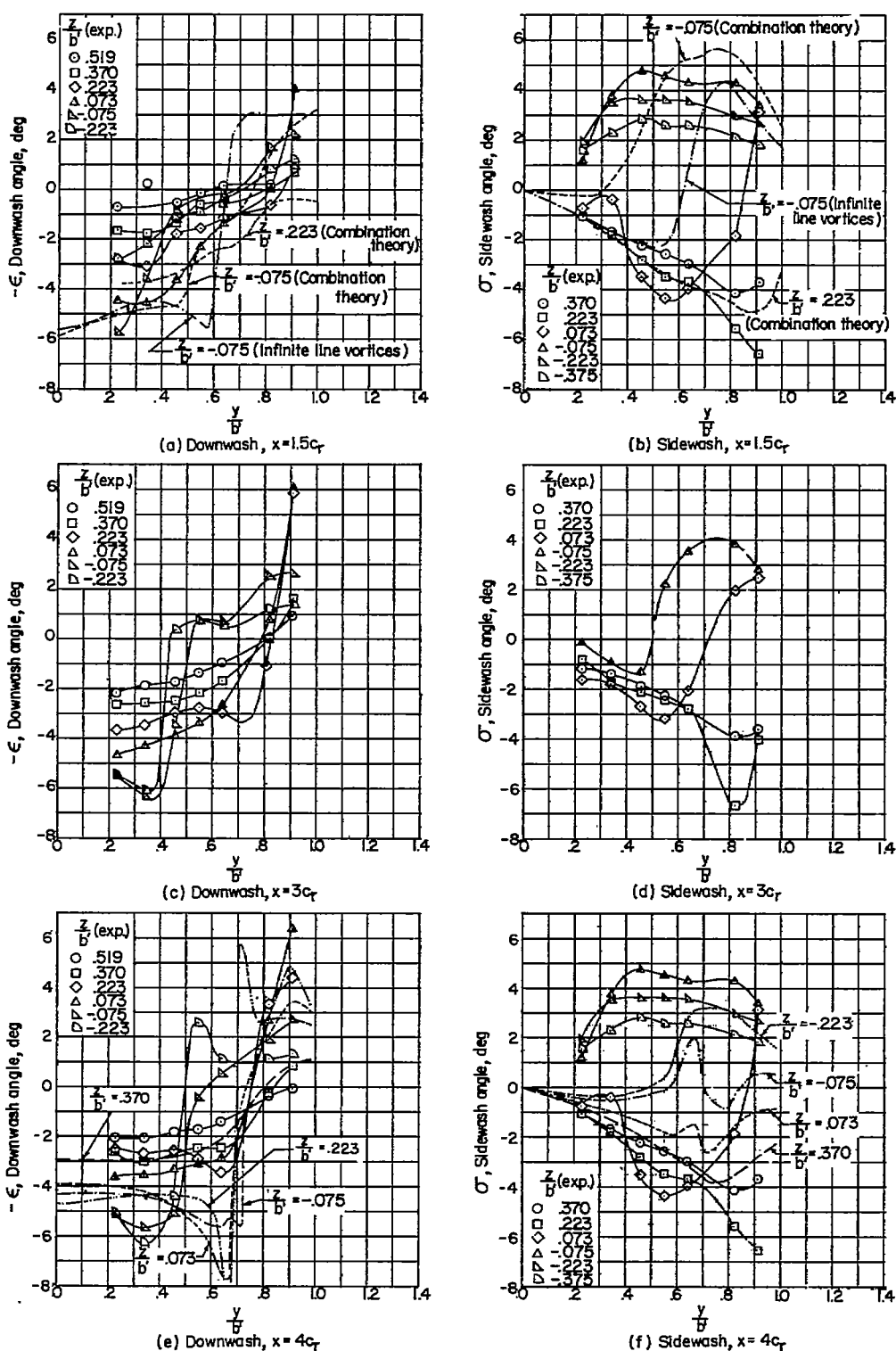
Figure 46.- Spanwise variation of downwash and sidewash for the 50° swept-back triangular wing. M = 2.41; R = 1.42 × 10⁶; α = 11.50°.
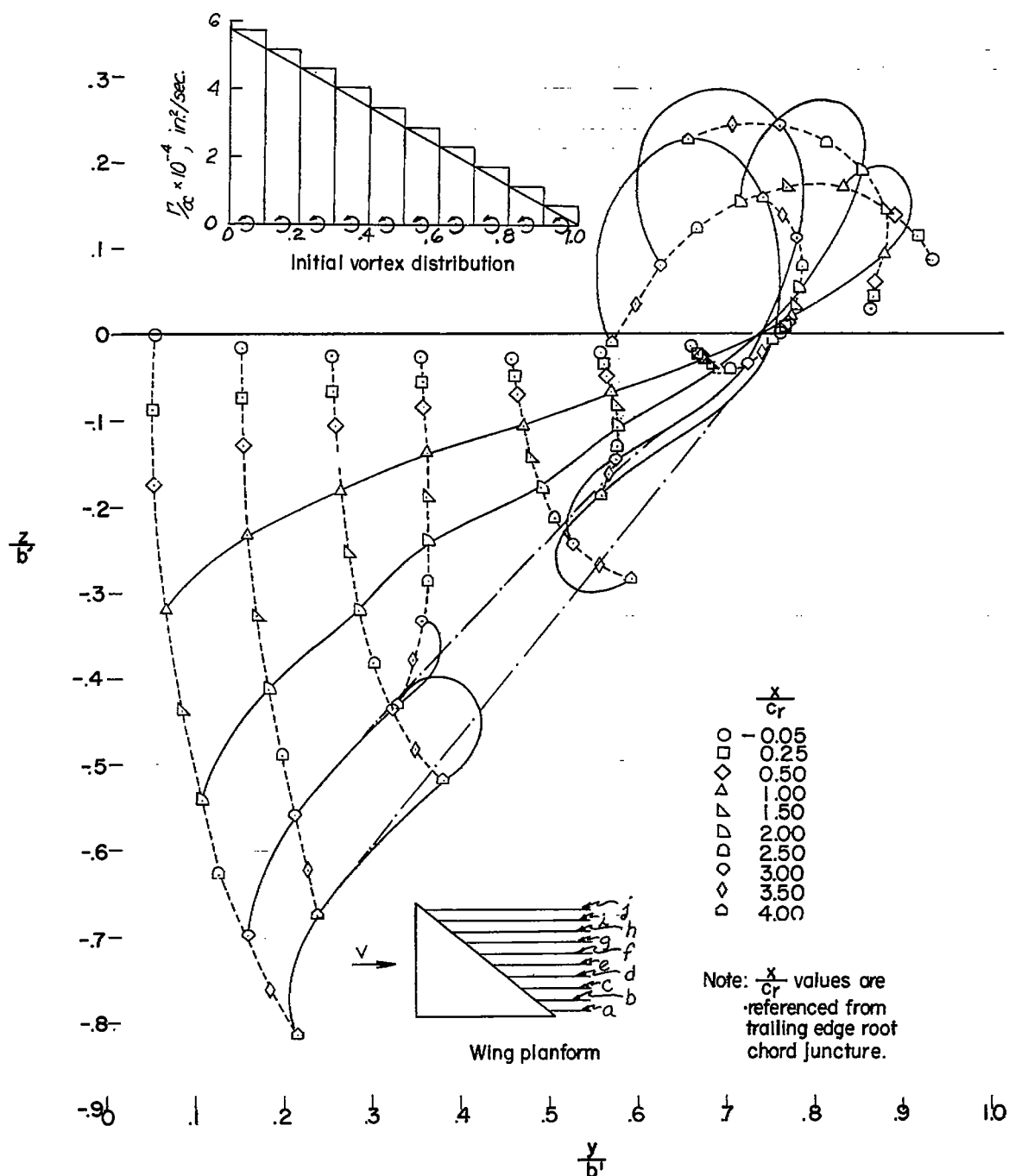
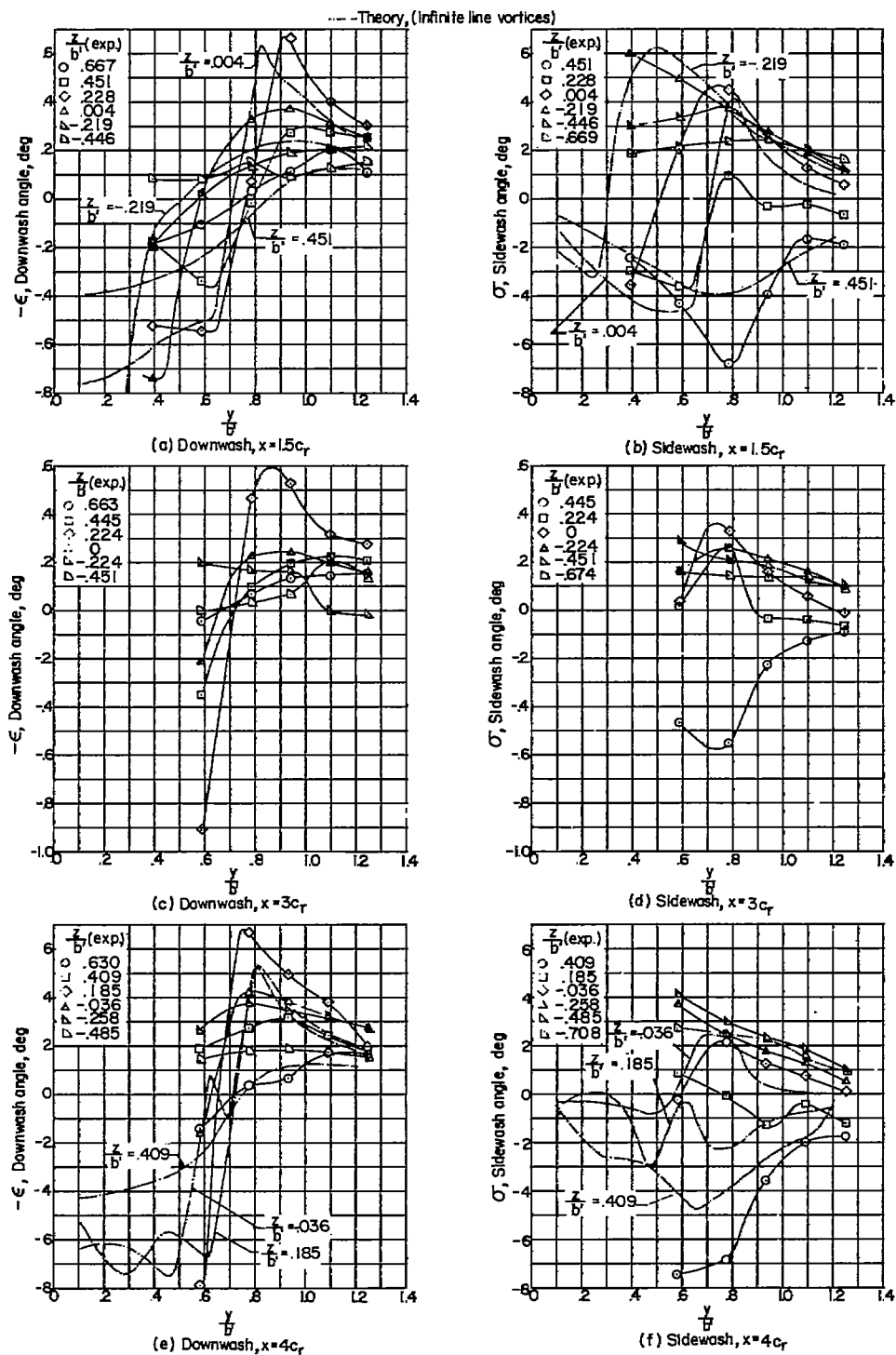Figure 47.- Theoretical paths of ten infinite line vortices behind the reversed triangular wing. M = 1.62; α = 9°.

Figure 48.- Spanwise variation of the downwash and sidewash for the reversed triangular wing $\left(\Lambda_{TE} = -50^\circ\right)$. M = 1.62; R = 1.42 × 10^6; $\alpha = 9^\circ$.
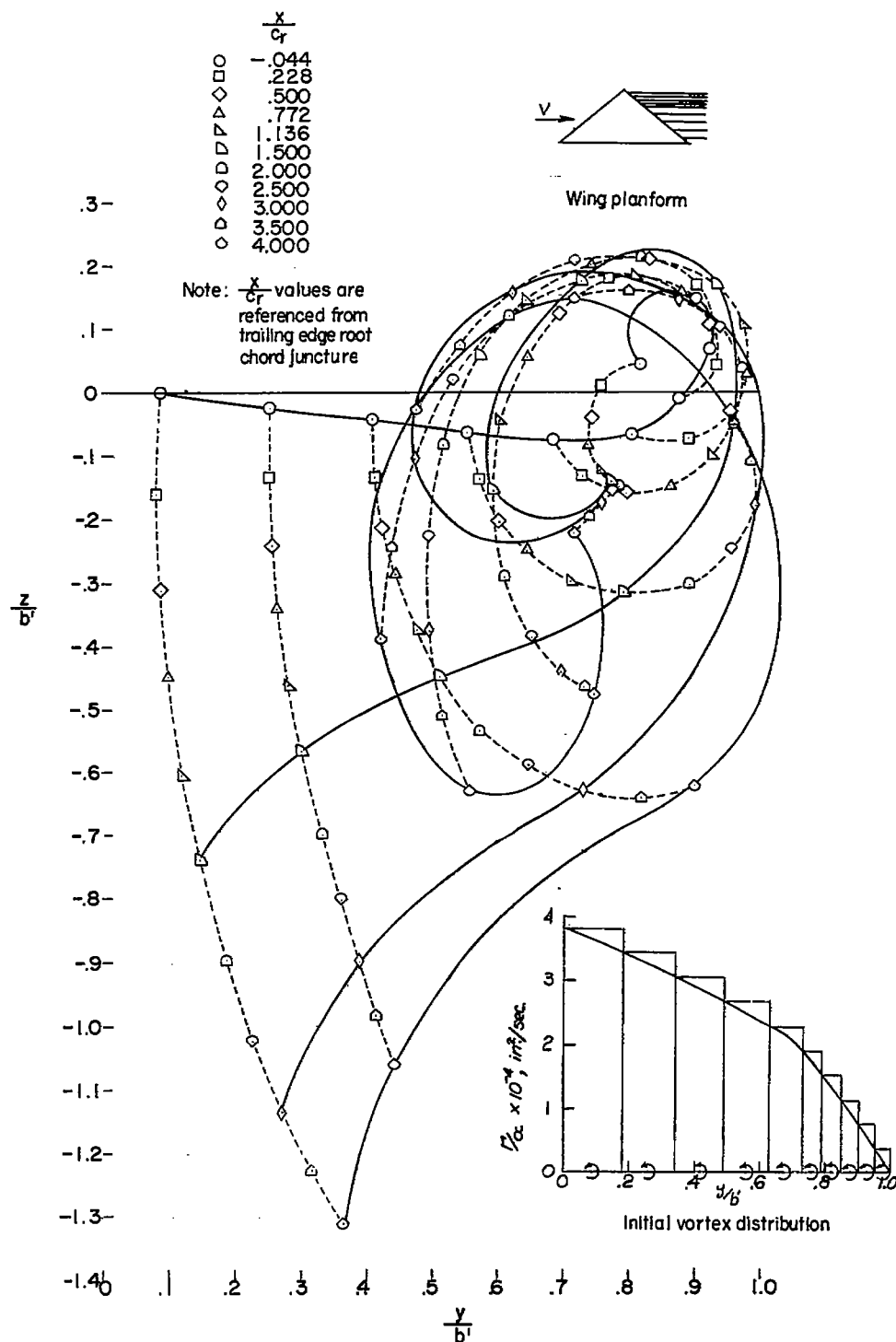
Figure 49.- Theoretical paths of ten infinite line vortices behind the straight 0-taper-ratio wing $\left(\Lambda = -\Lambda_{TE} = 50^\circ\right)$. M = 1.62; R = 1.42 × 10^6; α = 9°.
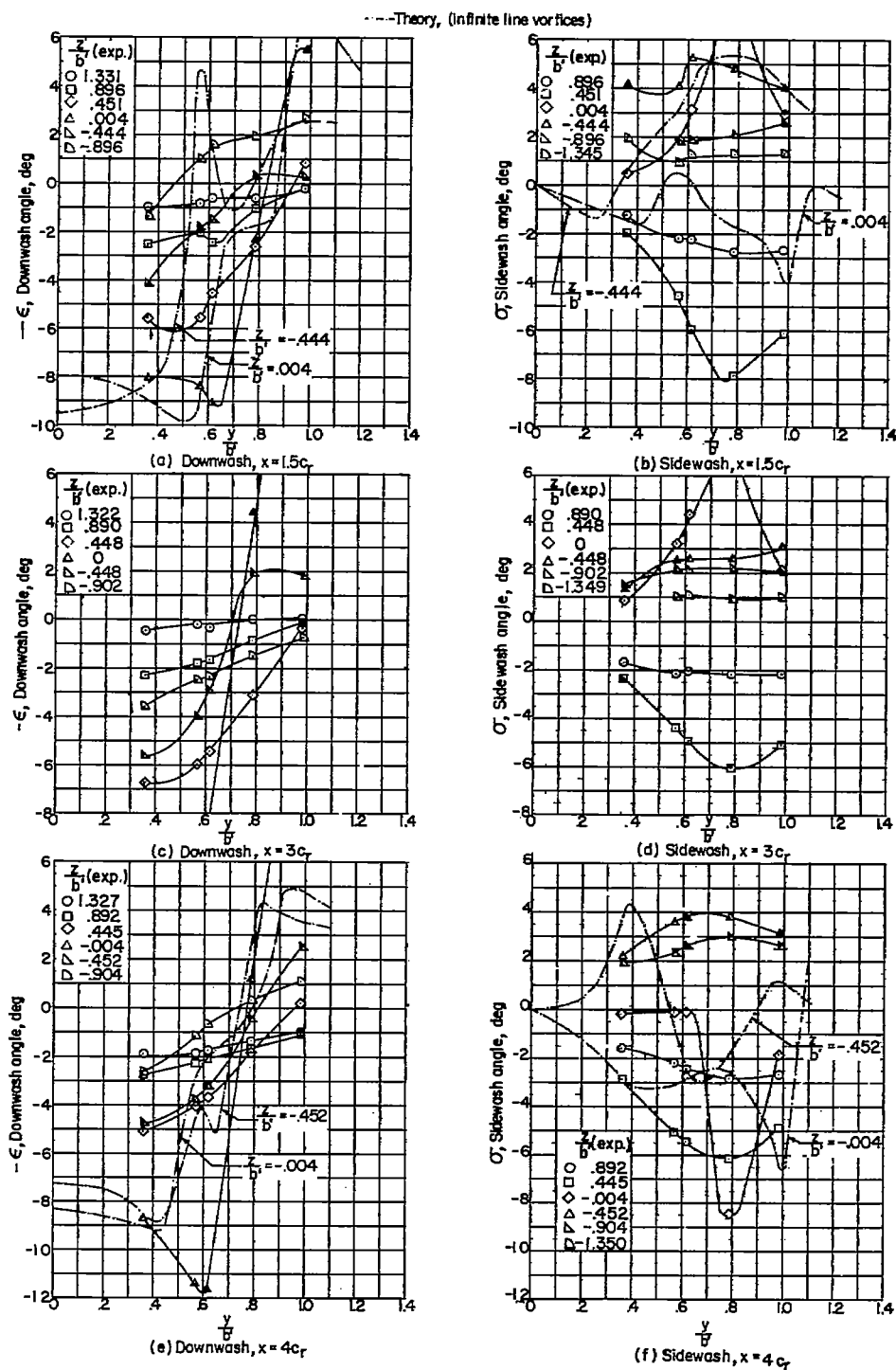
Figure 50.- Spanwise variation of the downwash and sidewash behind the straight 0-taper-ratio wing $(\Lambda = -\Lambda_{TE} = 50^\circ)$. M = 1.62; R = 1.42 × 10^6; α = 9°.